OPEN ACCESS

# ACTA METALLURGICA SLOVACA

2020, VOL. 26, NO. 2, 37-41

**RESEARCH PAPER**

## THE CORROSION AND WEAR RESISTANCE OF LASER AND MAG WELD DEPOSITS

*Anna Guzanová[1*], Miroslav Džupon[2], Dagmar Draganovská[1], Janette Brezinová[1], Ján Viňáš[1], Denis Cmorej[1], Erik Janoško[1], Pavlo Maruschak[3]*

[1]Technical University of Košice, Faculty of Mechanical Engineering, Košice, Slovakia

[2]Slovak Academy of Sciences, Institute of Materials Research, Košice, Slovakia

[3]Ternopil Ivan Puluj National Technical University, Faculty of Applied Information Technologies and Electrical Engineering, Ternopil', Ukraine

*Corresponding author: anna.guzanova@tuke.sk, tel.: +421949186308, Faculty of Mechanical Engineering / Technical University of Košice, 042 00 Košice, Slovakia

Received: 20.05.2020
Accepted: 30.05.2020

**ABSTRACT**

The paper focuses on the possibility of HPDC molds restoration for aluminium casting by laser and MAG weld cladding with a welding wire of the same grade like the base material. A chemical analysis of the weld deposits showed a decrease in the content of some elements in the MAG deposit due to the higher thermal input to the weld bath. The lower heat input of laser welding has resulted in a higher incidence of fusion defects lack between the weld deposit and the base material. Thermal conditions during welding affected hardness of weld deposits and their abrasive resistance as well. The resistance of materials against dissolution when immersed in AlSi8Cu3 alloy was similar for both deposits and the base metal.

**Keywords:** HPDC; mold; immersion test; linear polarisation; abrasive wear test

### INTRODUCTION

The production of molds for HPDC (a high pressure die casting) is the largest investment in a mass production of castings. Its return is closely related to its lifetime. Wear of hot working steels used for mold and dies production has stimulated many research activities. Jhavar [1] analyzed in detail the causes of dies and molds failure, while Anderson [2] conducted a similar study for extrusion tools and moreover Ebara [3] and Chander [4] for forging dies. Subsequently Markežič [5] focused on the HPDC process and considered the main mechanisms of mold failure: soldering (or die sticking), corrosion, erosion, thermal fatigue and cracking. Soldering is the bonding of the cast material to the mold surface and is the result of simultaneous metallurgical and mechanical bonding. Corrosion is associated with the loss of mold material due to metallurgical processes - especially metallurgical sticking and dissolution of the mold material by processed melt. Erosion is also characterized by the loss of material from the mold, but it is caused only mechanically - by flow of the melt in the mold [6]. The intensity of erosion increases with the mold temperature. The combination of high temperatures and pressures in the mold leads to thermal cracking of the mold material where the maximum mold temperature as well as the heating/cooling rate of the individual casting cycles play an important role [7]. Such a thermal load regime of the mold insert can also lead to oxidation of the surface layers and change of the microstructure [8] and hence the microhardness of the mold insert surface. According to Markežič [5], an adequate hardness of the mold functional surface is an essential characteristic that helps prevent the initiation and spread of wear and damage mechanisms. Subsequently, suitable technologies for the mold renovation were sought - local refilling of the material, which is missing after part deep removal of the material with cracks. In addition to the cold spraying technology tested by Lee [9] and showing promising results - the restored layer had a higher wear resistance than the original material, Chen [10] considers weld cladding to be undoubtedly the dominant restoration technology. For this purpose, for example Brezinova [11-13] tested with good results, CMT welding technology, or classic arc technologies [14-17], which are characterized by a high heat input produced in the weld bead and relatively a large volume of deposited metal. In order to minimize preheating and post-welding heat treatment, a multi-layer deposition is recommended for arc technologies, with the next layer providing heat treatment to the previous layer [15]. The relatively wide HAZ caused a great affection of the base material, and since according to Borrego [18] in the case of tensile residual stresses present in the deposit, the deposit could be just weaker point of the restored mold, the attention was next redirected to hybrid technologies [17] and technologies with a lower thermal input, in particular laser welding [18-25]. Laser welding allows, according to Borrego [18] and Cong [21,22], to achieve a smaller change in a chemical composition around the deposit, narrow HAZ, very precise deposition of a small volume of the filler material at a specified location without distortion. However, laser welding also has drawbacks. Borrego [18] notes that laser deposit can be at risk of tensile residual stresses, especially if it is single-layered [19] and planar defects, which can become cracks initiation sites. Vundru [19] in addition notes multilayer weld deposits have a high probability of compressive overall residual stresses which will improve their fatigue resistance.

Other ways of increasing the fatigue life of laser cladding are also being sought. Cong [21] tested positively the effect of biomimetic laser remelting on the fatigue life of laser cladding, and in [22] also tested the surface remelting with a certain pattern laser. Positive results are attributed to grain refinement and martensite formation at the melting point, which increases the hardness and resistance of the weld deposit to cracks propagation. Weld deposits, after machining, also requires to be coated by thin coatings which according to Knotek [26] can increase the life of the mold up to three times. Ch. Chen [10] emphasizes the need to predict the service life of restored mold parts which could help in making decision whether it is effective to proceed with a mold restoration.

The aim of this work is to determine the quality of the renovation layers created by laser and MAG welding using the same base and additive material (Uddeholm Dievar) in terms of chemical composition, continuity between the base material and weld clad, hardness, corrosion properties and change of the Young's modulus near the surface after corrosion exposition.

### MATERIAL AND METHODS

#### Base material (BM)

Base material – Uddeholm Dievar is a high performance Cr-Mo-V alloyed hot work tool steel, which offers a very good resistance to a high temperature tempering, gross cracking, hot wear and plastic deformation. The chemical composition given by steel producer: 0.35 % C, 0.2 % Si, 0.5 % Mn, 5 % Cr, 2.3 % Mo, 0.6 % V.

#### Weld deposition

Three-layer weld depositions by laser and MAG welding with a wire electrode of 1 mm in diameter made of the same steel Dievar were performed under following welding conditions:

**Laser welding (TruDisk 4002)**
- laser power 1.8 kW
- welding speed 10 mm/s
- focusing +6 mm above base material
- wire feed speed 0.7 m/min
- protective gas Ar 4.6 (30 l/min)
- optic cable diameter 0.4 mm

**MAG welding (Kemppi)**
- current 180 A
- voltage 25 V
- welding speed 5.7 m/min
- protective gas: 18% $CO_2$ + 82%Ar (M21 STN EN ISO 14175)
- gas flow rate: 14 l/min

**Chemical analysis of materials**

The test specimens with weld deposit were subjected to a chemical analysis by a spark optical emission spectrometer Belec Compact Port. The chemical analysis was performed three times on the base material, welding wire and also on the weld deposit.

**Metallographic analysis of materials**

A test samples were cut from the deposits and used for identification of the microstructure, corrosion resistance and hardness. Samples were metallographically processed and etched by 2% Nital and Cor etching agent (120 ml $CH_3COOH$, 20 ml HCl, 3 g picric acid, 144 ml $CH_3OH$).

**Measurement of hardness**

The microhardness of the base material and weld deposits were measured on Shimadzu HMV-2 along by three parallel lines in constant spacing across the sample thickness including weld deposit, HAZ, and base material. Load force applied was 980.7 mN (HV0.1), time 15 s.

**Linear polarisation method**

The corrosion properties of the base material and the weld deposit were determined using a linear polarization method with a three-electrode connection – weld deposit/base material, saturated calomel electrode and platinum electrode in 3.5% NaCl solution. The material OCP was measured in the unloaded circuit within 30 minutes, followed by polarization to the cathodic and anodic region ± 250 mV. Tafel curves have been further analysed with aim to determine $r_{corr}$.

**Hot-dip corrosion test by immersion in molten metal**

The dissolution of the base material and the deposits in processed melt was tested by immersion test. The ground and polished specimens of the base material and weld deposits were exposed in an AlSi8Cu3 alloy melt at a temperature of 680 ± 20°C for 300 minutes. The dissolution rate was identified by measuring the thickness of the compact layer of dissolution products.

**Abrasive wear test**

An abrasive wear was determined by the relative movement of the material relative to the abrasive cloth with grit size of P80 and P120 under load of 19.62 N (2 kg) and wear track was 40 m. The test was performed three times for each - base material, MAG and a laser weld deposition. A fresh abrasive cloth was used for each test.

**RESULTS AND DISCUSSION**

**Chemical analysis of materials**

Table 1 shows the chemical analysis of the base material, welding wire and the deposits as the average of the three measurements.

**Table 1** The chemical analysis of the base material, wire and weld deposits, wt. %, Fe – balance, P<0.002, S=0.004

| | C | Si | Mn | Cu | Al | Cr | Mo | Ni | V |
|---|---|---|---|---|---|---|---|---|---|
| **BM** | 0.457 | 0.18 | 0.40 | 0.07 | 0.02 | 4.98 | 2.04 | 0.09 | 0.72 |
| **wire** | 0.362 | 0.16 | 0.37 | 0.05 | 0.02 | 4.14 | 3.73 | 0.35 | 0.09 |
| **laser** | 0.445 | 0.20 | 0.28 | 0.40 | 0.01 | 4.58 | 2.19 | 0.08 | 0.76 |
| **MAG** | 0.338 | 0.13 | 0.26 | 0.53 | <0.002 | 4.36 | 2.04 | 0.07 | 0.52 |

The change in the content of the individual elements in the weld over the base and filler material is due to the mixing of the base and filler material and the oxidation-reduction processes during the transfer of the molten metal in the arc. A greater loss of additive elements is observed with MAG technology due to the higher heat input to the weld area.

**Metallography of weld deposits**

Fig. 1 shows the macrostructure of the laser weld deposit, the microstructure of the base material, the heat affected zone and the weld deposit.

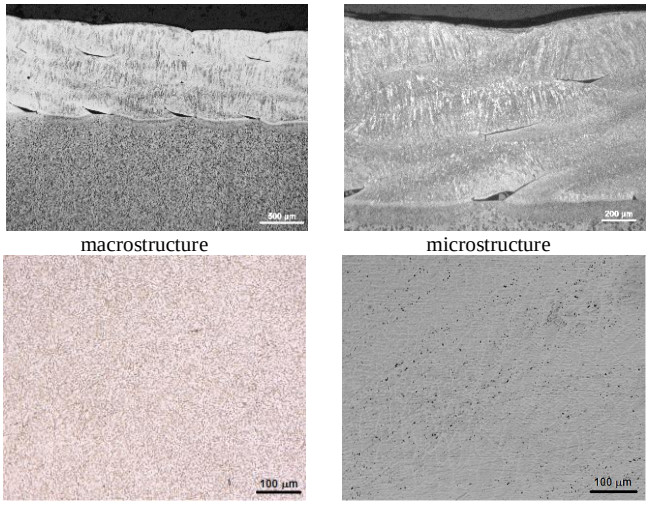


macrostructure microstructure

microstructure of BM laser weld deposit

**Fig. 1** Macro- and microstructure of laser weld deposit and BM, Nital, LM

Crack defects were not observed by the light microscopy technique in the Dievar base material under 1 mm thick weld deposit. In the middle of deposit thickness, isolated microcavity defects were present. On the boundary between the weld deposit and the base material there were defects in the connection (the lack of fusion defects) of 0.50 mm average length which occasionally corresponded to the crack defects. Between the weld metal and the base material, as well as between the adjacent deposit layers, there were present the lack of fusion lenticular defects. Capello [27] also notes that the first layer in the multilayer laser cladding is critical because it provides attachment to the substrate. In the area of fusion defects lack between the base material and the weld deposit, lines of oxygen and elements present in the weld deposit were detected by a semi-quantitative EDX microanalysis. In the vicinity of the crack roots which corresponded to lack of fusion defects between the deposit and base material, only the alloying elements in the deposit were present. Defects are not of metallurgical origin as examined. The defects at the base material – a weld deposit interface and the defects between the weld deposit layers are due to the low heat input during laser welding, which was not sufficient to ensure completely remelting the previous material layer. Borrego in [18] also observed the same defects at certain welding parameters. He confirmed that these defects became initiation sites in a fatigue test, especially when the tensile residual stress acts in the deposit. It is therefore necessary to pay attention to the optimization of the welding process and to keep in balance the positives of low heat input and the risk of fusion defects lack.

Fig. 2 shows the macrostructure of the MAG weld deposit, the microstructure of the base material, the heat affected zone and the weld deposit.

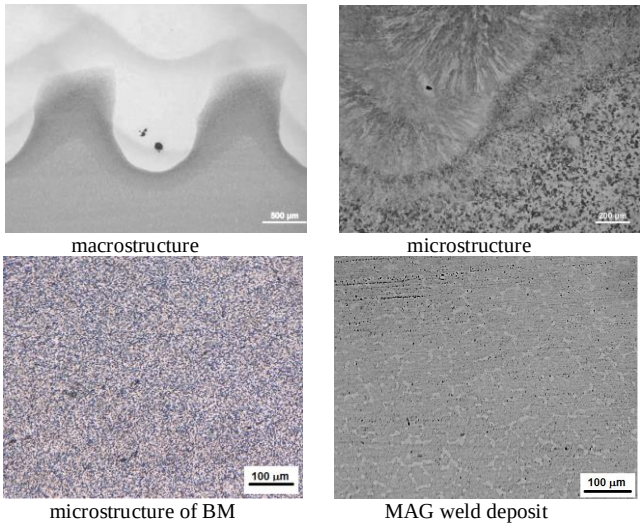


macrostructure microstructure

microstructure of BM MAG weld deposit

**Fig. 2** Macro- and microstructure of MAG weld deposit and BM, Nital, LM

Crack defects were not observed by the light microscopy technique in the Dievar base material under a 2.2-3.2 mm thick weld deposit. Isolated defects – microcavities were present as a result of entrapped gas bubbles. There were observed no defects in the connection between the base material and the weld deposit, nor between the adjacent layers in deposit. No cracks were observed by light microscopy technique. This is related to the higher thermal input of MAG technology compared to laser welding technology. The microstructure of the experimental material, soft annealed, consists of carbides heterogeneously distributed in the ferritic matrix. Transition between BM and MAG deposit shows characteristic undulating pattern, observed also by Nevskii in [28] in plasma deposits. Pattern formation is ascribed to flow of an incompressible viscous fluid at deposit/BM interface and to combination of Rayleigh–Taylor and Kelvin–Helmholtz instabilities, which dominates at specific transversal velocity.

The micro- and macro-structure of the weld deposit shows the heat affection lines of the first bead by next deposited layer. Based on the work of Suarez [14], it is possible to assume a slight tempering of the first layer by next one, which could temper sudden changes in hardness across the deposit. The hardness profile of the weld deposit is given in the next chapter.

Macrodefects either in the form of lack of fusion defects or air bubbles, but also microstructural formations such as heterogeneously distributed carbides can be considered as stress concentrators, from which, at the moment when the driving forces for crack propagation exceed the stress intensity factor, cracks can propagate in the weld or in the base material. The speed of short-crack propagation depends, among other things, on the grain composition (size, orientation etc.), but also on the residual stresses present in the weld. Although the presence of compressive residual stresses is generally considered to be positive, Gliha [29] states that at the stress levels much lower than the fatigue limit, a short crack begins to propagate through the field of compressive residual stresses. Due to the decreasing compressive residual stress during the crack propagation, the crack closure decreases and effective stress intensity factor increases. The result is the quickly increasing short-crack propagation. Despite the decelerated initial crack propagation due to the compressive residual-stress field, the crack, sooner or later, propagates to the domain of the tensile residual stress. Then the crack propagates faster.

**Microhardness of weld deposits**

Fig. 3 shows course of microhardness from weld deposit made by both technologies through HAZ to base material.

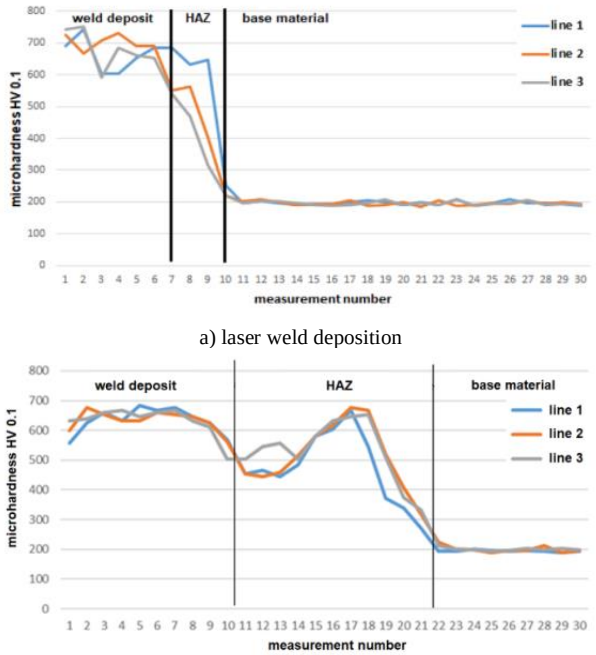


a) laser weld deposition




b) MAG weld deposition

**Fig. 3** Graphic course of hardness from MAG weld deposit, through HAZ to base material

The average hardness of the base material was 195 HV0.1. The hardness of the laser deposit was highest in the top layer (680 HV 0.1), dropping sharply through the heat affected zone to the hardness of the base material. Due to the lower heat input, the HAZ area was narrower compared to the MAG technology. The course of hardness through laser cladding is similar to that found Kattire in [24] on the same material. By phase analysis he proved connection between hardness and microstructure in deposit areas. The highest hardness in top layer of deposit is caused by harder carbides distributed in the martensitic matrix. Far from the surface, their precipitation decreases to the area with less hard-type carbides located in the tempered martensite matrix.

The highest hardness was detected in the surface layer of the MAG weld deposit (670 HV 0.1). Another hardness peak was recorded again in the weld deposit however at a depth of 5-7 mm below the surface (663 HV 0.1). At a greater distance, the hardness dropped very quickly through HAZ to the hardness of the base material (197 HV0.1). Suarez in [14] attributes the peaks in the hardness of multi-weld deposits to their too short overlapping, with alternating tempered and non-tempered areas. Hu [15] notes that the first layer which is welded without preheating and hence its cooling rate is high, has a fine-grain structure and contains hardening phases, and even after the next layer deposition, tempered grain size remains still fine. The temperature of the first layer serves as the preheating for the next layer deposition, and the temperature of the entire workpiece increased continuously with the deposition of the subsequent layers. Therefore, the cooling speed decreased as well as the fraction of the hardening phases, which resulted in lower hardness. Both deposits are characterized by high surface hardness, which, according to Markežič [5], may lead to decreases in the density and depth of thermal fatigue cracks.

**Corrosion resistance of materials – Tafel analysis**

Table 2 shows the corrosion characteristics measured and calculated by Tafel analysis valid for the base metal - Dievar and weld deposits made by particular technologies.

**Table 2** Results of Tafel analysis for Dievar

| | $E_{corr}$ [mV] | $I_{corr}$ [µA] | bc [mV] | ba [mV] | $r_{corr}$ [mmpy] | Rp [Ohm] |
|---|---|---|---|---|---|---|
| **BM** | -579 | 7.84 | 834 | 75 | 0.29 | 3311 |

| | | | | | | |
|---|---|---|---|---|---|---|
| **Laser** | -482 | 8.53 | 367 | 114 | 0.31 | 3088 |
| **MAG** | -499 | 12.70 | 789 | 109 | 0.46 | 2739 |

Table 2 shows higher corrosion rate of both weld deposits compared to BM. This is a consequence of a change in the chemical composition of the weld due to melting, as the content of all important elements has been reduced, which can be seen in Table 1. The lower decarburization of the laser deposit resulted in a minimal increase in $r_{corr}$, while in the MAG deposit the slightly higher decarburization resulted in a more pronounced increase in the corrosion rate.

**Hot-dip corrosion by immersion in Al alloy**

Fig. 4 shows the results of area cross-sectional microanalysis (mapping) through the interface between the base material and melt or between welds and AlSi8Cu3 melt after 300 minutes of immersion.

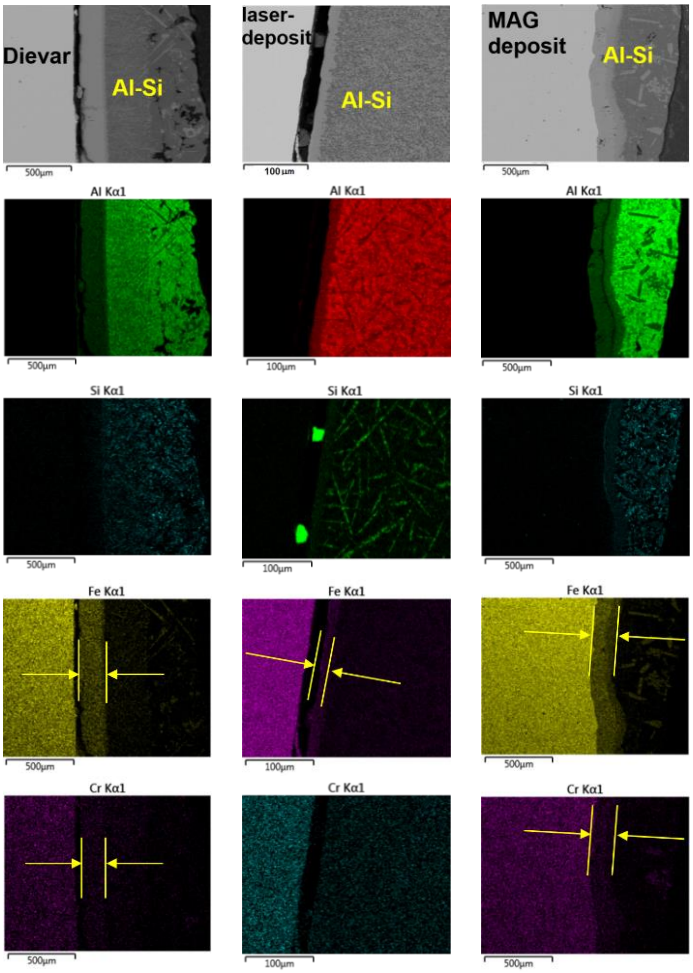


**Fig. 4** EDX mapping of the base material/weld deposits interface after immersion test

For both a ground and polished test specimens after 300 minutes of exposure in the melt of an aluminum alloy, a compact layer of the dissolving products of the base material or weld deposits remained on the both surfaces of the test specimens. Its thickness was determined using cross-sections and verified by mapping, mainly by Fe and Al maps. Thickness of compact layer on base material, laser deposit and MAG deposit was 200 µm, 25 µm and 180 µm, respectively. Fe map indicates a respective dissolution of the base material/weld deposit in processed melt, whereas Al map indicates the dissolution of melt in the base material/weld deposit. It can be concluded, that resistance of the experimental weld deposits was not worse compared to hardened Dievar reference (base) material, moreover, resistance of laser deposit was noticeably higher.

Zhu [30] observed, when tested the solubility of the same steel in Al alloy's melt, the intermetallic layer that formed by consuming the base metal. Fe-Al binary diagram describes the occurrence of several intermetallic phases. The intermetallic layer is always more brittle than the original metal. Its formation also affects the mold surface properties and the relatively hard mold surface becomes more vulnerable. The dissolution products are washed away from the mold surface by a melt stream and the dissolution can continue in the next casting cycle. This phenomenon cannot be completely avoided. It is important to ensure that the resistance of weld deposits against dissolution is at least at the same level as resistance of new mold. The results confirmed such resistance.

**Abrasive wear test**

Fig. 5 shows the cumulative mass loss of the base material and weld deposits at two abrasive cloth grit sizes.

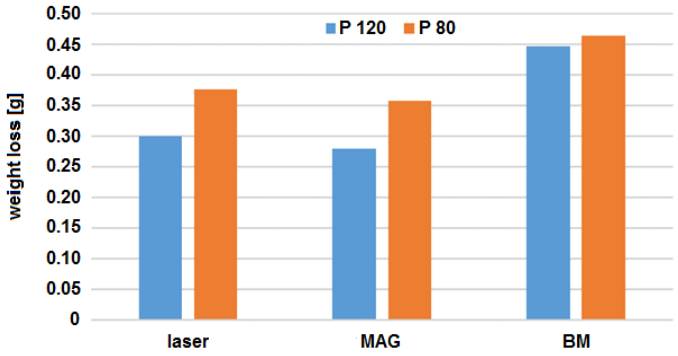


**Fig. 5** Mass loss of base material and weld deposits after wear test

Fig. 5 shows a slightly higher abrasive wear resistance of weld deposits against the base material. This is in direct proportion to the higher hardness of the weld deposits compared to the base material. The abrasive cloth with a grit size P80 caused higher material removal than P120. The results of the test indicate that when restore the molds by welding with both technologies, we will obtain a layer with higher wear resistance than the original base material.

However, the wear resistance of weld deposits is related not only to their hardness, but also to the residual stresses in the weld deposits. Although monitoring of residual stresses has not been included in experimental work, current publications show that the volume expansion caused by phase changes (especially martensitic transformation) in the weld deposit during the cooling process acts against shrinkage forces in the weld deposit. Thereby tensile residual stresses in the deposit are reduced and need of deposit post treatment is partially replaced. As a result, the hardness and abrasion resistance of the deposit are improved [31].

**CONCLUSIONS**

The paper brought the research results of weld deposits made by laser and MAG welding technology. The results subsequently showed the importance of welding process optimization which affects the occurrence of internal defects in relevant deposits. Their presence can be manifested in fatigue characteristics. Due to lower heat input, laser deposits showed numerous lack of fusion defects between BM and deposit, and also between individual layers of deposit. Structure of MAG deposit included sporadic gas entrapped bubbles only. The temperature conditions in both technologies have a direct impact on the microhardness profile of weld deposits. Hardness of top layer in both deposits are about the same (670-680 HV 0.1), hardness of base material is 195 HV 0.1. Due to lower heat input and narrow HAZ, hardness in laser deposit dropped very soon under the surface, whereas in MAG deposit high hardness maintained several mm under the surface. Despite of identical base material and welding wire used, corrosion resistance of deposits is slightly lower compared to base material due to change in chemical composition in deposits by burning off some elements, namely Cr. Change of chemical composition and corrosion rate is more pronounced in MAG deposit ($r_{corrMAG}$=0.46 mmpy, $r_{corrLASER}$=0.31 mmpy, $r_{corrBM}$=0.29 mmpy). Judging by the

thickness of interface compact layer of dissolution products formed by immersion in melt processed in HPDC process, the resistance of MAG weld deposit against dissolution in melt is at the level of resistance of original mold material (compact layer thickness about 0.2 mm), whereas resistance of laser weld deposit is significantly higher (compact layer thickness about 0.025 mm). Wear resistance copied hardness results, high hardness of deposits resulted in higher abrasive wear resistance compared to bas material, higher resistance showed MAG deposit compared to laser technology. In all tests, laser cladding showed slightly better results however contains more internal defects.
Authors recommend MAG welding when depositing larger areas and needing more deposited thickness. The weld deposit should be multilayered and the individual layers should be deposited immediately after each other. Less invasive laser welding is also recommended for multi-layer deposition, for smaller areas and less thicknesses.

**Acknowledgments:** Authors are grateful for the support of experimental works by projects VEGA No. 1/0497/20 "Application of progressive technologies in the restoration of functional surfaces of products" and APVV-16-0359 "The utilization of innovative technology for repair functional surfaces of mold casting dies for castings in automotive industry".

**REFERENCES**

1. S. Jhavar, C. P. Paul, N. K. Jain: Engineering Failure Analysis, 34, 2013, 519-535. http://dx.doi.org/10.1016/j.engfailanal.2013.09.006
2. M. J. Anderson, K. McGuire, R. C. Zante, W. J. Ion, A. Rosochowski, J. W. Brooks: Journal of Materials Processing Technology, 213(1), 2013, 111–119., http://dx.doi.org/10.1016/j.jmatprotec.2012.09.002
3. R. Ebara, K. Kubota: Engineering Failure Analysis, 15(7), 2008, 881–893. https://doi.org/10.1016/j.engfailanal.2007.10.016
4. S. Chander, V. Chawla: Materials Today: Proceedings, 4(2), 2017, 1147-1157. https://doi.org/10.1016/j.matpr.2017.01.131
5. R. Markezic, I. Naglic, N. Mole, R. Sturm: Engineering Failure Analysis, 95, 2019, 171-180. https://doi.org/10.1016/j.engfailanal.2018.09.010
6. Y. F. Wang, Z. G. Yang: Wear, 265(5-6), 2008, 871-878. https://doi.org/10.1016/j.wear.2008.01.014
7. A. Persson, S. Hogmark, J. Bergström: Surface and Coatings Technology, 191(2-3), 2005, 216-227. https://doi.org/10.1016/j.surfcoat.2004.04.053
8. J. Brezinova, D. Draganovska, A. Guzanova, P. Balog, J. Vinas: Metals, 6(2), 2016, 36. https://doi.org/10.3390/met6020036
9. J. C. Lee, H. J. Kang, W. S. Chu, S. H. Ahn: CIRP Annals, 56(1), 2007, 577-580. https://doi.org/10.1016/j.cirp.2007.05.138
10. Ch. Chen, Y. Wang, H. Ou, Y. He, X. Tang: Journal of Cleaner Production, 64, 2014, 13-23. http://dx.doi.org/10.1016/j.jclepro.2013.09.014
11. J. Brezinová et al.: Metals, 9(11), 2019, 1232. https://doi.org/10.3390/met9111232
12. J. Brezinova, M. Dzupon, D. Jakubeczyova, M. Vojtko, A. Guzanova, J. Brezina: Analysis of the quality duplex coating in melt of Al-Si based alloy, In: *Annual International Conference on Materials Science, Metal & Manufacturing, Global Science & Technology Forum*, Singapore, 2018, p.108-112
13. J. Brezinova, J. Vinas, P.O. Maruschak, A. Guzanova, D. Draganovska, M. Vrabel: *Sustainable renovation within metallurgical production*, first ed., RAM–Verlag, Lüdenscheid, Germany, 2017, 215 p.
14. A. Suarez, A.M. Suarez, W.T. Preciado: Procedia Engineering, 100, 2015, 584-591. https://doi.org/10.1016/j.proeng.2015.01.408
15. Z. Hu, X. Qin, T. Shao: Procedia Engineering, 207, 2017, 2203-2208. https://doi.org/10.1016/j.proeng.2017.10.982
16. Y. Zhao, X. Shi, K. Yan, G. Wang, Z. Jia, Y. Heb: Journal of Materials Processing Technology, 262, 2018, 382-391. https://doi.org/10.1016/j.jmatprotec.2018.07.003
17. Y. Zhang, G. Chen, C. Zhou, Y. Jiang, P. Zhong, Sh. Li: Journal of Materials Processing Technology, 245, 2017, 309-317. http://dx.doi.org/10.1016/j.jmatprotec.2017.02.029
18. L. P. Borrego, J. T. B. Pires, J. M. Costa, J. M. Ferreira: Engineering Failure Analysis, 16(2), 2009, 596–607. https://doi.org/10.1016/j.engfailanal.2008.02.010
19. Ch. Vundru, S. Paul, R. Singh, W. Yan: Procedia Manufacturing, 26, 2018, 952-961. https://doi.org/10.1016/j.promfg.2018.07.122
20. M. Franz, J. Bliedtner, C. Haupt: Procedia Engineering, 69, 2014, 237-240. https://doi.org/10.1016/j.proeng.2014.02.227
21. D. Cong et al.: Optics and Laser Technology, 53, 2013, 1-8. https://doi.org/10.1016/j.optlastec.2013.04.024
22. D. Cong et al.: Optics and Lasers in Engineering, 54, 2014, 55-61. http://dx.doi.org/10.1016/j.optlaseng.2013.09.012
23. C. Navas, A. Conde, B. J. Fernandez, F. Zubiri, J. Damborenea: Surface and Coatings Technology, 194(1), 2005, 136-142. https://doi.org/10.1016/j.surfcoat.2004.05.002
24. P. Kattire, S. Paul, R. Singh, W. Yan: Journal of Manufacturing Processes, 20, 2015, 492-499. http://dx.doi.org/10.1016/j.jmapro.2015.06.018
25. R. Song, S. Hanaki, M. Yamashita, H. Uchida: Materials Science and Engineering A, 483–484, 2008, 343-345. https://doi.org/10.1016/j.msea.2006.10.207
26. O. Knotek, F. Löffler and B. Bosserhoff, PVD coatings for diecasting moulds: Surface and Coatings Technology, 62, 1-3, 1993, 630-634. https://doi.org/10.1016/0257-8972(93)90310-K
27. E. Capello, D. Colombo, B. Previtali: Journal of Materials Processing Technology, 164-165, 2005, 990-1000. https://doi.org/10.1016/j.jmatprotec.2005.02.075
28. S. Nevskii, V. Sarychev, S. Konovalov, A. Granovskii, V. Gromov: Journal of Materials Research and Technology, 9(1), 2020, 539-550. https://doi.org/10.1016/j.jmrt.2019.10.083
29. V. Gliha, P. Maruschak, T. Vuherer: Materials and Technology, 47(4), 2013, 441-446.
30. H. Zhu: *Dissolution rate and mechanism of metals in molten aluminium alloy A380*, Purdue University, Indiana, USA, 2014, Open Access Theses. 465, https://docs.lib.purdue.edu/open_access_theses/465
31. S. Xu, X. Chen, S. Konovalov: Effect of phase transition temperature and particle size on residual stresses and properties of laser cladding layer, In: *IOP Conf. Series: Materials Science and Engineering, Metallurgy 2017*, Novokuznetsk, Russia, 411, 2018, p. 1-8. https://doi.org/10.1088/1757-899X/411/1/012084

OPEN ACCESS

# ACTA METALLURGICA SLOVACA

2020, VOL. 26, NO. 2, 42-44

**RESEARCH PAPER**

## EFFECT OF THE PLASTIC STRAIN AND DRAWING QUALITY ON THE FRICTIONAL RESISTANCE OF STEEL SHEETS

*Tomasz Trzepiecinski*

*Department of Materials Forming and Processing, Department of Materials Forming and Processing, Rzeszow, Poland*

*Corresponding author: tomtrz@prz.edu.pl, tel.: +48 17 743 2527, Faculty of Mechanical Engineering and Aeronautics/Rzeszow University of Technology, al. Powst. Warszawy 8, 35-959 Rzeszów, Poland

Received: 14.05.2020
Accepted: 04.06.2020

**ABSTRACT**

The aim of the research presented in this article is to investigate the frictional resistance of steel sheets with different drawing quality. Friction tests have been carried out using the bending under tension (BUT) test which simulates the contact conditions at the rounded edge of the punch in sheet metal forming operations. The effect of sheet deformation and temper state on the value of the coefficient of friction has been studied. It was found that increasing the value of elongation of the sheet is associated with an increase in the value of the COF for both friction conditions analysed. The intensity of work hardening, by changing the mechanical properties of the sheet, is a factor that changes contact conditions. The lubricant which is typically used in plastic working provided a reduction of frictional resistance by approximately 3.6-14%, depending on the degree of sheet deformation.

**Keywords:** coefficient of friction; friction; mechanical engineering; sheet metal forming; steel sheets; work hardening

### INTRODUCTION

The frictional resistances between the surfaces of both the deformed material and the tools in the sheet metal forming (SMF) process are one of the most important factors affecting the distribution of deformation in different zones of the workpiece. Many factors affect processes that arise in the contact zone, i.e. the normal pressures, surface topography of sheet plate and tools, physicochemical phenomena, mechanical properties of the sheet material, and type of lubricant [1-4]. Physicochemical phenomena occurring in the contact interface depend on the kinds of materials and chemical affinity of the friction pair. Friction connections between two bodies in contact are destroyed during reciprocal transition of contact pairs. The amount of frictional resistance arising is mainly determined by the shear strength of the friction connections [5, 6].

Friction and elastic deformation of the sheet metal have a great effect on the implementation of metal forming processes [7, 8]. Friction causes tangential stresses on the contact surface that change the stress state and cause non-uniformity in deformation and an increase in forming forces. Moreover, friction acts as a brake on the flow of material in the surface layers, which can lead to crack initiation. In addition, friction significantly increases tool wear [9, 10]. Lubrication of tools and the workpiece is used to reduce friction. It is important that the lubricant should have sufficient viscosity at the forming temperature and that it forms a thin, continuous film in an interface which is resistant to high pressures [11-14].

In SMF, there is initially a small actual area of contact between the tools and the workpiece. After applying pressure the elastic-plastic deformation of surface asperities occurs, which increases the actual area of contact [15, 16]. This leads to an increase in tangential stresses when the contacting surfaces move together. The shape of the contact surface affects the size of the nominal area of the contact surface. Furthermore, the stretching of the sheet metal and the work hardening phenomenon lead to a perpetual change in the surface topography of the sheet metal [17, 18]. Due to the occurrence of different contact conditions in particular areas of the drawpiece with regard to the state of stress and strain, and the speed of sliding, a number of tests have been developed to model friction conditions, i.e. the strip drawing test, bending under tension test, drawbead test, or a special test which simulates the material flow in specific areas of the stamping tools [19-21].

In this paper, the bending under tension (BUT) test has been used to investigate the effect of plastic strain (specimen elongation) and drawing quality on the amount of frictional resistance. The test sheets have been fabricated in three states: drawing quality (DD), deep drawing quality (DDQ) and extra deep drawing quality (EDDQ). The BUT test has been carried out using a special tribological simulator.

### EXPERIMENTAL

#### Material

Steel sheets in three states of fabrication: DQ, DDQ and EDDQ, were used as test material. The mechanical properties of the sheets were determined in a uniaxial tensile test on a Schenck type UTS 100 testing machine according to the ISO 6892-1 standard. The samples were cut along (0°) and transverse (90°) to the sheet rolling direction. The strain hardening properties have been determined by approximation of the true stress-true strain relation using the Hollomon equation $\sigma = K \cdot \varepsilon^n$, where σ is the true stress, $\varepsilon$ is the true strain, $K$ is the strength coefficient and n is the strain hardening exponent. Three samples were tested for each direction and then the average values of specific parameters were determined (Table 1).

In order to compare the effect of temper state on the frictional resistance of the sheets, the surface roughness of the sheets should be as similar as possible. The sheets for friction tests were selected so that the roughness average *Sa* was in the smallest possible range. *Sa* is a commonly used parameter to characterise surface roughness in industry. The *Sa* of the test sheets was in the range 0.302-0.362 μm. Surface roughness was measured using a Taylor-Hobson Surtronic 3+ device.

#### Test method

The bending under tension test permits the determination of the frictional resistance at the rounded edge of the punch (Fig. 1) in SMF. Friction tests have been conducted using a special friction simulator (Fig. 2) mounted on a universal tensile testing machine. A strip sheet was held at both ends in tension members. The specimen is wrapped around a cylindrical fixed roll with a diameter of 20 mm and loaded in a universal tensile testing machine. A roll made of cold-working tool steel was used with surface parameters *Ra* measured parallel to the roll axis: 0.32 μm. The coefficient of friction (COF) has been determined based on the back tension force $F2$ [N] and front tension force $F1$ [N] according to the relationship:

$$\mu = \frac{2}{\pi} ln\left(\frac{F1}{F2}\right) \tag{1.}$$

where: $F1$ [N] - front tension force,
$F2$ [N] - back tension force.

**Table 1** Basic mechanical properties of steel sheets

| State | Nominal sheet thickness *t*, mm | Yield stress $\sigma_p$, MPa | Ultimate tensile stress $R_m$, MPa | Elongation, % | Strength coefficient *K*, MPa | Strain hardening exponent *n* |
|---|---|---|---|---|---|---|
| DQ | 1.0 | 193 | 352 | 35 | 558 | 0.17 |
| DDQ | 1.0 | 162 | 311 | 41 | 452 | 0.21 |
| EDDQ | 1.0 | 152 | 281 | 43 | 484 | 0.22 |

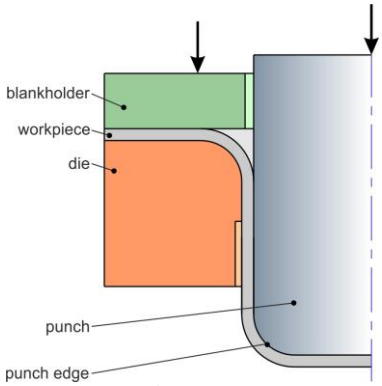


**Fig. 1** Region of the rounded edge of punch

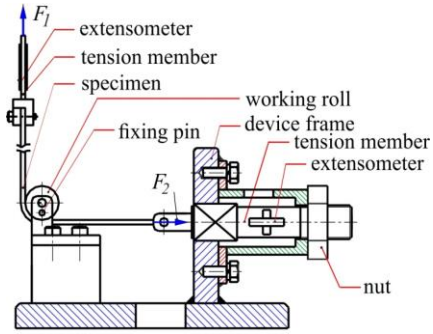


**Fig. 2** Schematic view of the testing device

Tensile forces were measured using extensometers. The deduction of equation 1 may be found in [5]. Both tensile forces were measured simultaneously during the test so that it was possible to determine the COF for the specific strain of the strip sheet. The constant stretching speed was set as 0.3 mm·s$^{-1}$. Strip specimens were cut along the sheet rolling direction and were carefully prepared to assure a constant width of 10 mm. The initial length of the specimen measured between the load cells was $L_0$ = 135 mm. The friction tests were carried out in dry and lubricated conditions. Machine oil LAN-46 (Orlen Oil) with a kinematic viscosity of 43.9 mm$^2$·s$^{-1}$ (at 40°C), viscosity index 94, ignition temperature 232°C, and flow temperature -10°C was used as lubricant. To produce both conditions, rolls and specimens were degreased using acetone.
The lubricant was distributed uniformly on the surface of the samples at 2 g·m$^2$ using a shaft [22]. The specimen elongation was measured according to the relationship:

$$\lambda = \frac{\Delta L}{L0} \cdot 100\% \qquad (2.)$$

where: $\Delta L$ [mm] – the displacement of the gripper of a tensile machine,
$L0$ [mm] - the initial length of the specimen measured between the load cells.

## RESULTS AND DISCUSSION

In general, increasing the value of elongation of the sheet is associated with an increase in the value of COF for both friction conditions analysed (Figs. 3, 4). Under dry friction conditions, stabilisation of the frictional resistance is visible after exceeding a deformation of approximately λ = 0.2 (Fig. 3). This effect is also invisible in the case of lubricated conditions (Fig. 4). The work hardening of the sheet increases its hardness and stabilises the topography of the sheet surface.

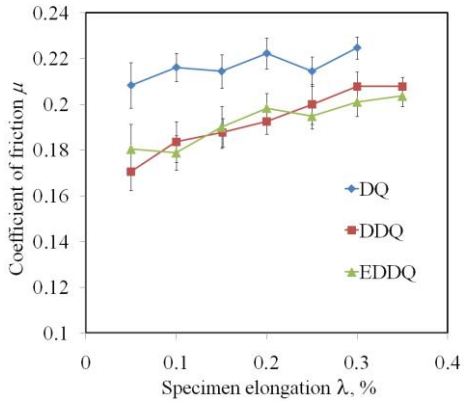


**Fig. 3** Effect of specimen elongation on the COF for dry friction conditions

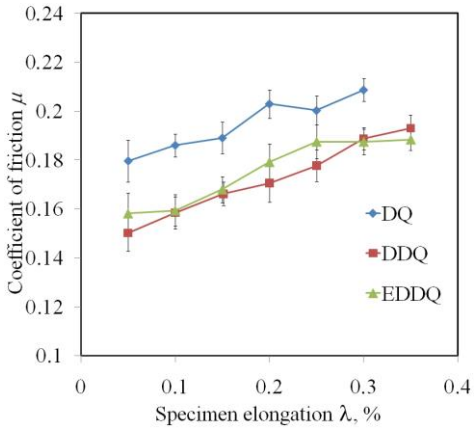


**Fig. 4** Effect of specimen elongation on the COF for lubricated conditions

Pressure is then transmitted through the material core, while the actual area of contact does not change further. The greater the elongation of the specimen, the greater the contact pressure acts on the surface of the countersample which is associated with work hardening [23]. The greater is the pressure, the lower is the lubrication efficiency. The lubricant in the oil pockets is subjected to increased pressure, which is not able to balance the increasing resistance of the contacting surfaces as a result of ploughing and flattening of the workpiece surface. It can be concluded that the dominant mechanism under high pressure was the mechanical interaction of the surface asperities. The highest frictional resistance was observed for the DQ sheet, which is characterised by the largest susceptibility to material strengthening (Fig. 5).
To study the degree of friction reduction induced by the lubricant, the following coefficient has been introduced:

$$\gamma = \frac{\mu d - \mu l}{\mu l} \cdot 100\% \qquad (3.)$$

where: $\mu$d - the COF determined in dry conditions,
$\mu$l - the COFs determined in lubricated conditions.

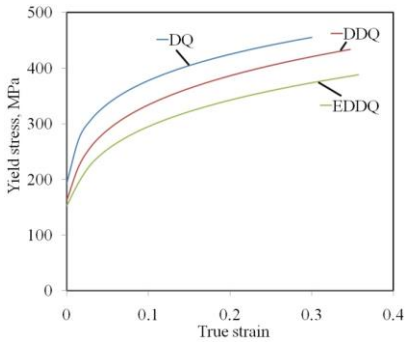


**Fig. 5** Strain hardening curves

Lubrication efficiency described by the coefficient γ decreases most with the degree of deformation of the DQ sheet (Fig. 6). With a sheet deformation of λ = 0.15 mm, very similar efficiency was observed for all sheets tested. The sheet that exhibits the largest work hardening at larger deformations shows a significant reduction in lubrication efficiency. The most favourable properties of the lubricant were demonstrated during the testing of the DDQ sheet.

In the case of this sheet, the most uniform lubricant interaction was observed over the entire range of sheet deformation. The ability of the lubricant to reduce frictional resistance under high pressure is particularly important in the automotive industry where the components are fabricated with surface finish. The roughness valleys (Fig. 7) that entrap lubricant between the tool surface and the workpiece surface act as lubricant reservoirs.

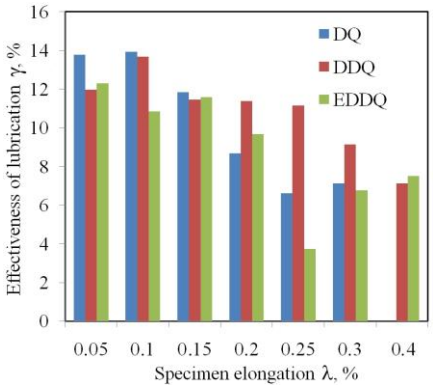


**Fig. 6** Effect of specimen elongation on the effectiveness of lubrication

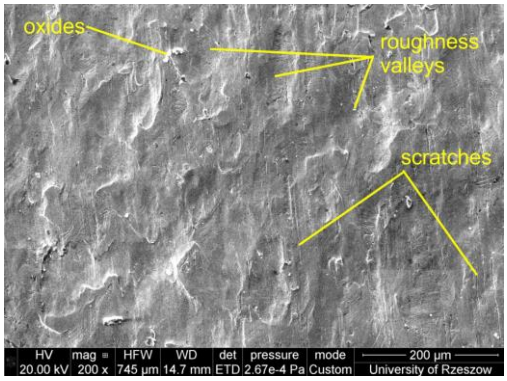


**Fig. 7** Scanning Electron Microscopy (SEM) micrograph of sheet surface (λ = 0.2, DDQ sheet metal, dry friction).

## CONCLUSION

The difference in the COF values between DDQ and EDDQ sheets over the entire range of deformations is very similar. The intensity of work hardening is a factor that changes contact conditions since it changes the mechanical properties of the sheet. The COF value for the DQ sheet was about 0.02-0.03 higher compared to the other sheets. The typical lubricant used in plastic working provided a reduction of frictional resistance of approximately 3.6-14%, depending on the value of the sheet deformation (Fig. 6). Lubrication efficiency decreased with increasing normal pressure as a result of the increasing of both front and back tensile forces. This leads to intensification of the mechanical interactions of the surface asperities. Under such conditions the lubricant could not balance these resistances.

**Acknowledgments:** The authors of this paper would like to kindly thank Dr. Wojciech Bochnowski from the University of Rzeszow for the preparation of the SEM micrographs.

## REFERENCES

1. J. Hol, M. V. Cid Alfaro, M. B. de Rooij, T. Meinders: Wear, 286-287, 2012, 66-78. https://doi.org/10.1016/j.wear.2011.04.004
2. E. Zdravecká, M. Marton, A. Gmiterko, J. Tkáčová: Tribology in Industry, 36(1), 2014, 3-8.
3. M. Tomáš, E. Evin, J. Kepič, J. Hudák: Metals, 9(10), 2019, 1058. https://doi.org/10.3390/met9101058
4. H. Wei, G. Hussain, A. Iqbal, Z.P. Zhang: International Journal of Advanced Manufacturing Technology, 101, 2019, 2533-2545. https://doi.org/10.1007/s00170-018-3096-1
5. M.R. Lovell, Z. Deng: Tribology International, 35(2), 2002, 85-95. https://doi.org/10.1016/S0301-679X(01)00097-4
6. W. Wang, Y. Zhao, Z. Wang, M. Hua, X. Wei: Tribology International, 93, 2016, 17-28. https://doi.org/10.1016/j.triboint.2015.09.011
7. J. Slota, M. Jurcisin, L. Lazarescu: Acta Metallurgica Slovaca, 20(2), 2014, 236-243. https://doi.org/10.12776/ams.v20i2.298
8. J. Bidulska, T. Kvackaj, R. Bidulsky, M.A. Grande: Kovove Materialy, 46(6), 2008, 339-344.
9. L. Kirkhorn, V. Bushlya, M. Andersson, J.E. Ståhl: Wear, 302(1-2), 2013, 1-2, 1268-1278. https://doi.org/10.1016/j.wear.2013.01.050
10. J. Kondratiuk, P. Kuh: Wear, 270(11-12), 2011, 839-849. https://doi.org/10.1016/j.wear.2011.02.011
11. H.B. Löfgren: Theoretical and Applied Mechanics Letters, 8(1), 2018, 57-61. https://doi.org/10.1016/j.taml.2018.01.002
12. J. Hol, V. T. Meinders, M. B. de Rooij, A. H. van den Boogaard: Tribology International, 8, 2015, 112-128. https://doi.org/10.1016/j.triboint.2014.07.015
13. B.H. Lee, Y.T. Keum, R.H. Wagoner: Journal of Materials Processing Technology, 130-131, 2002, 60-63. https://doi.org/10.1016/S0924-0136(02)00784-7
14. D. Wiklund, B.G. Rosén, L. Gunnarsson: Wear, 264(5-6), 2008, 474-479. https://doi.org/10.1016/j.wear.2006.08.032
15. W.R.D. Wilson, S. Sheu: International Journal of Mechanical Sciences, 30(7), 1988, 847-868. https://doi.org/10.1016/0020-7403(88)90002-1
16. C. Wang, R. Ma, J. Zhao, J. Zhao: Journal of Manufacturing Processes, 27, 2017, 126-137. https://doi.org/10.1016/j.jmapro.2017.02.016
17. M. Ramezani, Z.M. Ripin: International Journal of Advanced Manufacturing Technology, 51, 2010, 93-102. https://doi.org/10.1007/s00170-010-2608-4
18. P.L. Menezes, K. Kumar, Kishore, S.V. Kailas: International Journal of Advanced Manufacturing Technology, 40, 2009, 1067-1076. https://doi.org/10.1007/s00170-008-1425-5
19. K. Seshacharyulu, C. Bandhavi, B.B. Naik, S.S. Rao, S.K. Singh: Materials Today: Proceedings, Vol. 5, No. 9, p. 18238-18244. https://doi.org/10.1016/j.matpr.2018.06.160
20. A. Makhkamov, D. Wagre, A.M. Baptista, A.D. Santos, L. Malheiro: Ciência & Tecnologia dos Materiais, 29(1), 2017, e249-e253. https://doi.org/10.1016/j.ctmat.2016.07.002
21. L. Figueiredo, A. Ramalho, M. C. Oliveira, L. F. Menezes: Wear, 271(9-10), 2011, 1651-1657. https://doi.org/10.1016/j.wear.2011.02.020
22. T. Trzepieciński, R. Fejkiel: Tribology International, 115, 2017, 78-88. https://doi.org/10.1016/j.triboint.2017.05.007
23. H.G. Lemu, T. Trzepieciński: Strojniski vestnik-Journal of Mechanical Engineering, 59, 2013, 41-49. https://doi.org/10.5545/sv-jme.2012.383

OPEN ACCESS

# ACTA METALLURGICA SLOVACA

2020, VOL. 26, NO. 2, 45-48

**RESEARCH PAPER**

## PRODUCTION OF COMPOSITE PELLETS FROM WASTE COFFEE GROUNDS, MILL SCALE AND WASTE PRIMARY BATTERY TO PRODUCE FERROMANGANESE; A ZERO WASTE APPROACH

*Selçuk YEŞİLTEPE*[1]*, *Mustafa Kelami ŞEŞEN*[1]

Istanbul Technical University, Metallurgical and Materials Engineering Department, Maslak, Istanbul, Turkey

*Corresponding author: yesiltepes@itu.edu.tr, tel.: +90 212 285 7061, Istanbul Technical University, Metallurgical and Materials Engineering Department, Turkey.

Received: 07.05.2020
Accepted: 26.05.2020

**ABSTRACT**

This study was aimed to produce ferromanganese by using waste battery as manganese source, mill scale as iron source and waste coffee ground as reduction agent and carbon source. Waste batteries were collected from waste battery collection bins. Mill scale was collected from hot rolling workshop. Waste coffee grounds were household used coffee. All starting materials were characterized. Weighted raw materials blended with addition of bentonite as a binder. Pelletizing equipment was used to produce composite pellets. Produced pellets were dried then used for reduction experiments. Reduction experiments were conducted in Argon purged tube furnace for 1250 $^{o}$C, 1300 $^{o}$C and 1400 $^{o}$C according to thermodynamic background. Produced ferromanganese samples were characterized for chemical compositions and metallization rate.

**Keywords:** waste battery, pelletizing, mill scale, waste coffee, recycling, zero waste.

### INTRODUCTION

Waste management is gaining importance because of depleting natural resources. Increasing consumption of materials with increasing population gained popularity to recycling and material recovery technologies. Energy efficiency is another important issue in recycling operations. Recycling of a material decreases the energy consumption by cutting off raw material preparing steps in production.

Waste battery is considered as a hazardous waste because of acidic or basic electrolyte in the battery system [1]. Primary batteries or in other words single use batteries are designed for one time using with irreversible chemical reactions to produce electrical current [2]. There are different types of batteries with different ingredients, the most known and used primary battery composition is ZnO – $MnO_2$ with option of alkaline and Zn – C varieties [3]. The difference between Zn – C and alkaline batteries is used electrolyte. Zn – C batteries uses $ZnCl_2$ as electrolyte while alkaline battery uses KOH [4]. Cathode and anode structures are similar in both battery types [2]. Recycling of single use batteries studied from different researchers with different methods. General approach for recycling single use batteries is pyrometallurgical method because of fast and efficient process [3]. Primary waste battery recycling consists of reduction – evaporation of Zn at first step followed by total or partial reduction of manganese oxides to produce various manganese based chemicals or alloys [5, 6]. High vapour pressure of Zn at relatively low temperatures to Mn available the vaporization - condensation route for Zn recovery in battery recycling [6]. Vacuum applied processes can be applied to decrease Zn evaporation temperature [6, 7]. After Zn recovery batteries can be used as Mn raw material and generally considered for ferromanganese production [3, 6].

Waste coffee grounds are evaluated in various recycling applications due to large amount of waste [8]. Coffee is the second most used trading good after petroleum worldwide [9]. Waste coffee grounds are used with and without treatment in various applications. Waste coffee grounds are valorized to produce carbon based materials generally [8, 10, 11]. Active carbon [12], pharmaceutical compounds [11], biodiesel [10], anode material [13] are produced via valorization of waste coffee grounds. Chemical treatment is applied to waste coffee grounds to refine unwanted compounds in order to obtain desired products without using valorization in different applications [14, 15]. Large consumption amounts and accessible waste stream worldwide, offers different recycling or reusing opportunity to waste coffee grounds.

Hot rolling process is applied to steel slabs in order to produce thinner steel sheet. Mill scale is the lost material from steel slab due to oxidation at annealing step of hot rolling [16]. Mill scale is consists of oxides of elements in steel which is Fe in large portions. Recycling of mill scale is generally reuse of material in steelmaking process as an iron source [17]. Mill scale can be used in production of iron based materials as well[18]. Mill scale contains high iron amount thus can be evaluated as raw material for steel producing instead of blending in other resources[19], [20]. Recycling of mill scale and other steelmaking dusts requires pre-treatment of sample in order to use in conventional steelmaking process. Agglomeration is applied to iron containing dusts due to small particle size that restricts use in blast furnace operation [16,17–21-23]. Pelletizing can be used as an agglomeration process in the recycling of mill scale.

This study is aimed to produce ferromanganese with using waste coffee grounds as a reductive carbon source, waste battery paste as manganese source and mill scale for iron source. Pelletizing process is applied to produce composite pellets for reduction. Reduction of pellets is conducted in controlled atmosphere tube furnace. Characterization of starting materials and end product is done.

### MATERIAL AND METHODS

#### Raw Materials

Waste coffee grounds are collected from household wastes. Collected waste coffee grounds are washed with distilled water and dried at 105 $^{o}$C for 24 hours. DTA-TG analysis of waste coffee grounds is applied to sample of 1 mg. Waste battery is obtained from municipal battery collection points. Waste batteries are shredded; steel casing and battery paste is separated. Chemical analysis of battery paste is done with standard procedure of Atomic Absorption Spectroscopy. The battery paste is washed with distilled water to wash out the battery electrolyte. Mill scale is chemically analyzed with AAS and XRD technique is used to determine phases of oxides. Further explanation of characterization results of raw materials are discussed in Results. Blend composition is given in Table 1. Bentonite that used in pelletizing process as binder is Na-based bentonite obtained from Tokat-Turkey. Chemical composition of Na-bentonite is analyzed with AAS and phases are determined by X-ray analysis.

**Table 1.** Blend composition of pelletizing raw materials.

| Element | % |
|---|---|
| Zn | 14.4 |
| Mn | 20.3 |
| Fe | 20.19 |
| C | 4.3 |
| Bentonite | 2.0 |
| Oxides | 38.81 |

#### Pelletizing

Pelletizing of raw materials is done to produce composite ferromanganese pellets. Total 1500 g of blend is used. Materials are calculated to have 150% excess carbon with Fe/Mn ratio of 1:1. Raw materials are blended with Na-bentonite of

%2 wt. as binder. Laboratory scale pelletizing disc of 50 cm diameter is used with 40 rpm rotational speed. Agglomeration of blended dust is obtained by manual water spraying. Produced pellets are tested for free fall test for elasticity determination. Water spraying of pellets continued until free fall number of 3 is obtained. Produced pellets are dried at 105 °C for 24 hours before firing/reducing in Argon purged tube furnace.

**Thermodynamic Calculations**

Reduction of metallic oxides by carbon is the general practice for many manufacturing process. Production of ferromanganese needs extensive CO partial pressure for reduction of MnO [24]. CO is produced in reduction systems via Boudouard reaction. Boudouard reaction is the basis of carbothermic reduction system. Boudouard reaction is given as;

$$2CO \leftrightarrow C + CO_2 \quad (1)$$

CO is produced or consumed in the reduction system according to equilibrium of Boudouard reaction. CO is more stable at elevated temperatures than $CO_2$. Due to this thermodynamic background reduction reactions are expected to start with solid C then proceed to CO gas-solid reactions.

Free energy calculations for reduction of Zn, Fe and Mn oxides are done with HSC 6.1 thermodynamic database. Gibbs free energy of oxides along with CO and $CO_2$ are given in Figure 1. Ellingham diagram shows reduction of FeO occurs below 800 °C while ZnO carbothermal reduction is about 950 °C. MnO reduction with CO occurs at the temperature of 1400 °C. MnO can be reduced by Mn or Fe carbides formed in system. High solubility of Fe and Mn in each other at high temperatures can decrease the activation energy need in MnO reduction.

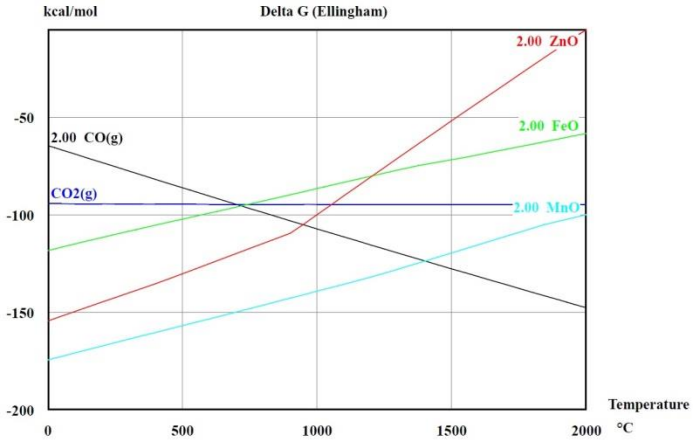


**Fig 1.** Ellingham diagram of Zn, Fe, Mn oxides with CO and CO2.

Ellingham diagram shows reduction conditions for metal oxides in the system. Reduction reactions of ZnO and MnO are expected to take place in CO atmosphere. On the other hand, FeO carbothermic reduction is at the equilibrium temperature of the Boudouard reaction. That means FeO can be reduced via both C and CO or in other words direct and indirect reaction take place in FeO reduction simultaneously. Reduction reactions of metal oxides are given as;

$$MnO + CO = Mn + CO_2 \quad (2)$$
$$ZnO + CO = Zn + CO_2 \quad (3)$$
$$FeO + CO = Fe + CO_2 \quad (4)$$
$$FeO + C = Fe + CO \quad (5)$$

**Reduction Process**

Reduction roasting process is proposed based on thermodynamic calculations and literature knowledge. Proposed flow diagram of process is given in Figure 2. Raw materials of waste coffee grounds, mill scale and waste battery paste are blended with bentonite powder. Blend is pelletized with water addition in laboratory scale pelletizing disc with diameter of 50 cm. Pellets are dried then direct reduced in Argon purged (1 lt/min) tube furnace at 1250, 1300 and 1400 °C. Chemical analysis of pellets is conducted with Atomic Absorption Spectroscopy. Condensed ZnO is found in furnace exit. ZnO could not be collected in experiments due to lack of facilities for condensation chamber.

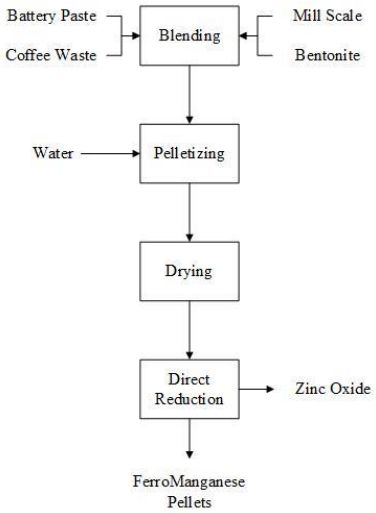


**Fig 2.** Flow sheet of process.

**Characterization Methods**

Raw materials are analyzed with Atomic Absorption Spectroscopy techniques via Perkin Elmer Analyst 800. All of raw materials are leached with aqua regia solution at 110 °C on hot plate for 30 minutes. Solution is analyzed via AAS with standard protocol. XRD analysis' of materials are conducted with PANalytical PW 3040/60 using Cu Kα radiation (λ=0.154 nm). DTA-TG analysis is conducted with Perkin Elmer Diamond under Ar flow at temperature increase rate of 5 °C/min. Pellet free fall number is determined by free fall of pellets from 50 cm of height until crack occurs. Moisture content of pellets is determined by placing in incubator at 105 °C for 24 hours then measuring the weight difference. Pelletizing efficiency is calculated with formulae;

$$\text{Efficiency\%} = \frac{\text{Acceptable Pellets (9–16 mm)}}{\text{Initial Mass of Blend}} \text{x100} \quad (6).$$

Pellets are sieved manually after pelletizing and pellets in the range of 9-16 mm are accepted as green pellets. Efficiency of Zn removal, Fe metallization and Mn metallization are calculated with formulae;

$$\text{Efficiency\%} = \frac{\text{Reduced Mass}}{\text{Initial Mass}} \text{x100} \quad (7).$$

**RESULTS AND DISCUSSION**

Raw materials are characterized with techniques mentioned in Experimental Materials and Methods section. DTA-TG analysis of coffee grounds is given in Figure 3. Coffee ground is analyzed and pyrolysis occurred under Argon atmosphere. Stable carbon is found to be in left over mass after gasification in DTA-TG analysis. Stable carbon amount is 18.5% in used spent ground coffee waste. Pyrolysis process of spent ground coffee starts in 300 °C and finishes about 500 °C. Mass loss of spent ground coffee waste continues with higher temperature exposure but to a limited extend. 18.5 % of spent ground coffee waste is taken into account in calculations for reductive carbon source.

Pyrolysis of waste coffee grounds produces reduction agent of carbon in the pellets. Carbothermal reduction of zinc, iron and manganese oxides requires high energy and CO partial pressure [6, 24]. Pyrolysis and reduction process takes place simultaneously in the reduction vessel. Thermodynamic calculations along with DTA/TG analysis can be concluded into that pyrolysis is followed by reduction reaction.

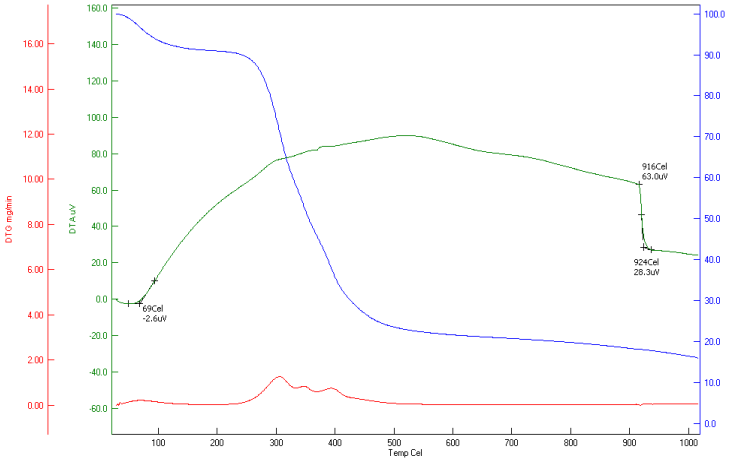


**Fig 3.** DTA-TG analysis of spent ground coffee waste.

Chemical composition of washed, dried waste battery is given in Table 2. Waste battery paste is rich in manganese and zinc oxides. Alkaline based electrolyte in alkaline batteries is the cause of K in battery paste. Manganese is evaluated is main manganese source for ferromanganese production. Zinc is planned to be evaporated and condensed as zinc oxide in furnace.

**Table 2.** Chemical analysis of spent battery paste.

| Element | % |
|---|---|
| Zn | 29.1 |
| Mn | 40.37 |
| K | 2.32 |
| Fe | 1.35 |
| Pb | 0.0018 |
| Loss of Ignition | 26.96 |

Mill scale chemical analysis and XRD analysis is given in Table 3 and Figure 4 consecutively. Main compound in mill scale is iron and iron oxides. Mill scale is collected from hot rolling workshop. Chemical composition of mill scale represents original chemical composition of steel slab in oxide form. Table 3 shows large amount of iron without excessive alloying elements.

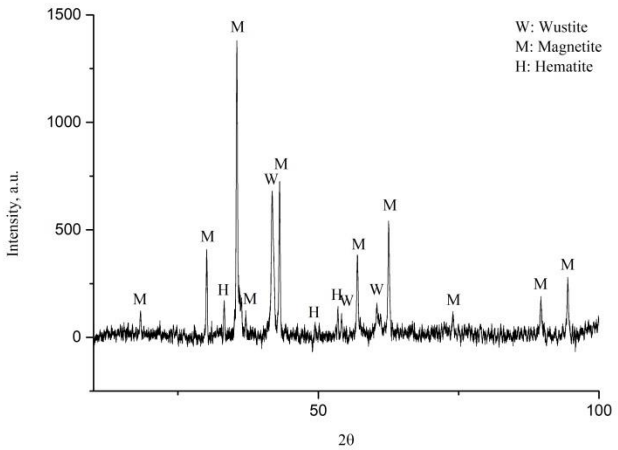


**Fig 4.** XRD pattern of mill scale.

**Table 3.** Chemical analysis of mill scale.

| Compound | % |
|---|---|
| **Iron Oxides(total)** | 98.33 |
| **MnO** | 0.58 |
| **$SiO_2$** | 0.21 |
| **$Cu_2O$** | 0.24 |
| **$Cr_2O_3$** | 0.29 |
| **Others** | 0.35 |

Na-bentonite chemical analysis is given in Table 4. Bentonite consists of aluminum calcium silicates with addition of $Na_2O$. Relatively higher $Na_2O$ level of bentonite is the cause of Na-bentonite naming.

**Table 4.** Chemical analysis of bentonite.

| Compound | % |
|---|---|
| **$SiO_2$** | 52.70 |
| **$Al_2O_3$** | 20.40 |
| **$Fe_2O_3$** | 5.17 |
| **CaO** | 4.86 |
| **MgO** | 1.83 |
| **$K_2O$** | 1.10 |
| **$Na_2O$** | 2.75 |
| **LOI*** | 11.19 |

LOI: Loss Of Ignition

Pelletizing experiment results are collected in three subjects; pelletizing efficiency, free fall test and moisture content. All results are given in Table 5. Free fall numbers and moisture content of green pellets meet the green pellet requirements for pelletizing. Efficiency of pelletizing process is adequate to consider the process feasible.

**Table 5.** Green pellet properties.

| Property | Result |
|---|---|
| **Free Fall Mean Number** | 3 |
| **Moisture Content** | 10.44 % |
| **Pelletizing Efficiency** | 91.18% |

Metallization rate of iron and manganese is calculated after reduction experiments. Produced ferromanganese alloy is characterized with AAS technique. Zinc is evaporated from reaction chamber and zinc evaporation rate is calculated with leftover zinc in ferromanganese. Results of ferromanganese chemical analysis are given in Table 6. Metallization rate is visualized in Figure 5. The produced ferromanganese alloy is low in manganese than calculated value. This result shows that the alloy cannot be considered as ferromanganese but a master alloy in ferromanganese production.

Use of waste coffee grounds as reducing agent in composite pellets is efficient in reduction of manganese, iron and zinc oxides. Pyrolysis of waste coffee grounds produces amorphous carbon skeleton of coffee grain with high surface area [13]. High surface area, direct contact of reagents eases the reduction process. Reagent contact and short diffusion pathway for reducing gases helps the reduction process. Reduction temperature of the pellets is lower than thermodynamic calculated reduction point nevertheless metallization of 70% in manganese was achieved in this study. XRD analysis of pellets that reduced at 1400 $^{o}$C conducted to understand what is produced. XRD results explains low metallization rate of manganese. MnO peaks are exhibited along with manganese peaks while the rest is cementite ($Fe_3C$). Thermodynamic background supports this result that MnO needs high CO pressure and high temperature to be reduced [24]. Further reduction of MnO needs higher CO partial pressure hence approximately 29% Mn left in MnO form. Increasing the reduction rate of MnO can be achieved by increasing the temperature or CO partial pressure. XRD result of reduced pellets is given in Figure 6.

**Table 6**. Chemical analysis of Ferromanganese.

| Element | %, 1250 $^{o}$C | %, 1300 $^{o}$C | %, 1400 $^{o}$C |
|---|---|---|---|
| Fe | 44.8 | 46.6 | 49.1 |
| Mn | 34.7 | 35.6 | 35.7 |
| Zn | 0.032 | 0.015 | 0.014 |
| Others | Balance | Balance | Balance |

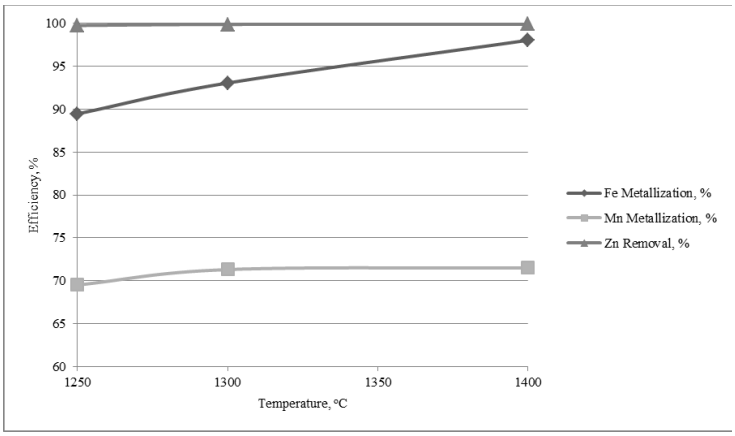


**Fig 5**. Fe and Mn metallization rate with Zn removal rate.

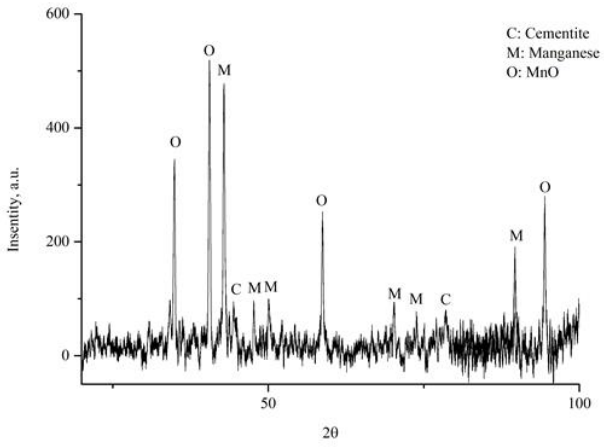


**Fig 6.** XRD analysis of reduced pellet at 1400 °C.

**Conclusion**

Pelletizing of waste coffee grounds, waste battery paste and mill scale is a promising solution for recycling of these wastes. The produced pellets have sufficient properties for producing ferromanganese. Pelletizing process efficiency is calculated 91.18% which can be evaluated as successful. This process can utilize three different waste into two useful products; ferromanganese and zinc oxide. Waste batteries are classified as hazardous waste and by this process it can be turned into a useful product. Pelletizing process and solid state reaction ease the operation of waste utilization. Zinc oxide on the other hand can be evaluated in producing zinc metal or various compounds. The wastes are totally converted into useful products and economical value is obtained.

**References**

1. Yeşiltepe S, Sesen MK (2019) Battery Collection in Turkey, Case Study of Küçükçekmece Municipality. J. Int. Environmental Application & Science, 14:116–121.
2. Espinosa DCR, Mansur MB (2012) Recycling batteries. Waste Electr Electron Equip Handb 365–384. https://doi.org/10.1533/9780857096333.3.365.
3. Bernardes AM, Espinosa DCR, Tenório JAS (2004) Recycling of batteries: A review of current processes and technologies. J Power Sources 130:291–298. https://doi.org/10.1016/j.jpowsour.2003.12.026.
4. Gallegos M V., Falco LR, Peluso MA, et al (2013) Recovery of manganese oxides from spent alkaline and zinc-carbon batteries. An application as catalysts for VOCs elimination. Waste Manag. 33:1483–1490. https://doi.org/10.1016/j.wasman.2013.03.006.
5. Ebin B, Petranikova M, Steenari BM, Ekberg C (2016) Production of zinc and manganese oxide particles by pyrolysis of alkaline and Zn-C battery waste. Waste Manag 51:157–167. https://doi.org/10.1016/j.wasman.2015.10.029.
6. Yeşiltepe S, Buğdaycı M, Yücel O, Şeşen MK (2019) Recycling of alkaline batteries via a carbothermal reduction process. Batteries 5:. https://doi.org/10.3390/batteries5010035.
7. Saotome Y, Nakazawa Y, Yamada Y (1999) Disassembling and materials recovering process of alkaline manganese dry batteries by vacuum-aided recycling systems technology (VARS Tech.). Vacuum 53:101–104. https://doi.org/10.1016/S0042-207X(98)00401-1.
8. Kovalcik A, Obruca S, Marova I (2018) Valorization of spent coffee grounds: A review. Food Bioprod Process 110:104–119. https://doi.org/10.1016/j.fbp.2018.05.002.
9. Chung CC, Chen ST, Chen YY, Chung CY (2014) The empirical study for national determinant of coffee consumption. Adv Mater Res 962–965:1275–1278. https://doi.org/10.4028/www.scientific.net/AMR.962-965.1275.
10. Caetano NS, Caldeira D, Martins AA, Mata TM (2017) Valorisation of Spent Coffee Grounds: Production of Biodiesel via Enzymatic Catalysis with Ethanol and a Co-solvent. Waste and Biomass Valorization 8:1981–1994. https://doi.org/10.1007/s12649-016-9790-z.
11. Mata TM, Martins AA, Caetano NS (2018) Bio-refinery approach for spent coffee grounds valorization. Bioresour Technol 247:1077–1084. https://doi.org/10.1016/j.biortech.2017.09.106.
12. Hernández Rodiguez M, Yperman J, Carleer R, et al (2018) Adsorption of Ni(II) on spent coffee and coffee husk based activated carbon. J Environ Chem Eng 6:1161–1170. https://doi.org/10.1016/j.jece.2017.12.045.
13. Gao G, Cheong L-Z, Wang D, Shen C (2018) Pyrolytic carbon derived from spent coffee grounds as anode for sodium-ion batteries. Carbon Resour Convers 1:104–108. https://doi.org/10.1016/j.crcon.2018.04.001.
14. Li RX, Shen XL, Zhou Y, et al (2016) Preparation and properties of polyurethane films with spent coffee grounds. Mater Sci Forum 848:148–151. https://doi.org/10.4028/www.scientific.net/MSF.848.148.
15. Zuorro A, Lavecchia R (2013) Preparation and characterization of magnetically responsive biosorbents from coffee industry residues. Appl Mech Mater 394:3–7. https://doi.org/10.4028/www.scientific.net/AMM.394.3.
16. Chen L (2013) Utilization of steelmaking and hot-rolling mill waste. Appl Mech Mater 261–262:627–630. https://doi.org/10.4028/www.scientific.net/AMM.260-261.627.
17. Zhang J, Liu S, Niu F, Xu Z (2013) Reviews on the comprehensive utilization of metallurgical dust from iron and steel plant. Appl Mech Mater 295–298:3075–3079. https://doi.org/10.4028/www.scientific.net/AMM.295-298.3075.
18. Bugdayci M., Alkan M., and Turan A. (2018) Production of Iron Based Alloys from Mill Scale through Metallothermic Reduction. High Temp. Mater. Proc. 37(9-10): 889–898. https://doi.org/10.1515/htmp-2017-0073.
19. Gaballah N.M., Zikry A.F., Khalifa M.G., Farag A.B., and Shalabi M.E.H. (2013) Production of Iron from Mill Scale Industrial Waste via Hydrogen, Open J Inorg. Non-Metall Mater. 2013: 23–28. http://dx.doi.org/10.4236/ojinm.2013.33005.
20. Martín MI, López FA & Torralba JM (2012) Production of sponge iron powder by reduction of rolling mill scale, Ironmaking & Steelmaking, 39:3, 155-162, https://doi.org/10.1179/1743281211Y.0000000078.
21. Maalem B, Berdjane D, Belahssen O, et al (2019) Identification of thermal and microstructural properties of hot rolling scale. Acta Metall Slovaca 25:291–296. https://doi.org/10.12776/ams.v25i4.1360.
22. Drobíková K, Plachá D, Motyka O, et al (2016) Recycling of blast furnace sludge by briquetting with starch binder: Waste gas from thermal treatment utilizable as a fuel. Waste Manag 48:471–477. https://doi.org/10.1016/j.wasman.2015.11.047.
23. Li XB, Wang W, Zhang DH, Xiong L (2014) Basic properties of iron and steel making dust. Adv Mater Res 937:187–190. https://doi.org/10.4028/www.scientific.net/AMR.937.187.
24. Sesen FE (2017) Practical reduction of manganese oxide. J Chem Technol Appl 01:1–3. https://doi.org/10.35841/chemical-technology.1.1.26-27.

OPEN ACCESS

# ACTA METALLURGICA SLOVACA

2020, VOL. 26, NO. 2, 49-53

**RESEARCH PAPER**

## THE IMPACT OF SHEAR GAP SIZE ON THE QUALITY OF THE SHEARED SURFACE IN ELECTRICAL STEEL SHEET BLANKING

*Emil Spišák[1]*, Janka Majerníková[1], Ľuboš Kaščák[1], Peter Mulidrán[1]*

[1)]Technical University of Košice, Faculty of Mechanical Engineering, Košice, Slovakia

*Corresponding author: emil.spisak@tuke.sk, Tel.: +421 55 602 3502, Department of Mechanical Engineering Technologies and Materials, Technical University of Košice, Letná 9, 042 00 Košice, Slovakia)

Received: 30.04.2020
Accepted: 28.05.2020

**ABSTRACT**

The quality of the sheared surface when blanking, also known as die-cutting, is the result of several factors. Based on current knowledge about blanking, the following technological parameters – shear gap size, blunting of the shearing tool, lubrication in the shearing process, and deformation rate – can be considered as decisive parameters on the quality of the sheared surface. The main material characteristics include yield strength, tensile strength, ductility, and ferrite grain size. The paper is focused on the influence of the shear gap on the quality of the shear surface of electrical sheets with different chemical composition and different mechanical properties. The quality of the cutting surface was characterized by the size of the plastic cutting area. The relationships between the size of the shear gap, which ranged from 1 to 7% of the thickness of the cut material and the size of the plastic shear area, were evaluated and measured macroscopically.

**Keywords:** electrical steel; shear gap; sheared surface

### INTRODUCTION

The constant pressure to reduce energy consumption brings along the need to increase energy efficiency and reduce the energy intensity of industrial machinery and equipment. Increasing energy efficiency is mostly focused on improving the technical parameters of energy equipment. One way of reducing energy intensity is to increase the efficiency of electric drives for machines and equipment. This is possible by using materials that have lower energy losses. Energy losses in electrical machines are greatly affected by the type of electrical steel used.

Electrical steel is one of the basic materials, used in the production of electrical rotating machines and transformers. Two major characteristics of electrical machines – performance and efficiency – depend on the quality of electrical steels. The quality of steel directly affects the efficiency of the use of electricity. The efficient use of electricity is one of the main factors determining the range of electric vehicles. Therefore, in recent years considerable attention has been paid to the issue of further improving the quality of isotropic steel sheets for electrical engineering and optimizing their production and processing. The resulting magnetic properties of electrical steel depend on numerous factors, including the chemical composition of the material, metallurgical purity, structural and metallographic characteristics, equilibrium or non-equilibrium changes, precipitate morphology and distribution, segregation enrichment of grain boundary surfaces, processing and heat treatment, deformation, and residual stress.

At present, electrical steel sheets are produced in metallurgical plants and delivered to the customers in the semi-processed and fully processed state. In Europe, the use of electrical steel for the production of electric motor cores in the semi-processed state is preferred. Asia and America typically use electrical steel in a fully processed state. This difference is caused by using different electrical steel processing technologies and varying technological know-how across countries. The increase in the use of electrical steel in the fully-processed state is caused by the possibility of its direct use without final processing, in less demanding applications, and in the availability of higher quality grades, that are not available in the semi-processed state.

Electrical steels are one of the most important magnetic materials produced today. Despite the increasing use of permanent magnets, their use for the production of stator and transformer cores is dominant. There are two basic types of electrical steels: grain-oriented steel and non-grain-oriented steel, both fully and semi-processed. The non-grain-oriented electrical steels are produced in the form of cold-rolled sheets with a thickness of 0.25, 0.35, 0.5 and 0.65 mm and are classified according to the maximum specific losses in W / kg.

Isotropic electrical steels belong to the group of soft magnetic materials and are used in various electrical applications and equipment. They are characterized by low losses caused by magnetization alternating electric field. High-silicon steels (often referred to as silicon steels) were developed at the beginning of the 20th century and very quickly became the preferred material used to build the cores of large transformers, motors, and generators. In 2018, the share of electrical steel increased to 3% of the total steel production [1], [2]. With the growth of electric vehicle production, the consumption of steel for the production of electric motor cores is also expected to increase.

The requirements for these steels are high permeability and induction, low magnetic losses and low magnetostriction. In certain specific cases, exceptional mechanical properties are also required. High permeability and induction reduce the size and weight of the cores. Low magnetic losses reduce heat generation and energy consumption. Mechanical properties affect shearability, resistance to fatigue fracture resulting from sudden changes in mechanical stress and resistance to material deformation at high rotor or stator speeds [3-5].

The chemical composition of these steels is similar – especially as far as the basic alloying elements are concerned, and the manufacturing processes have not changed significantly for years. However, steel losses with a given Si and Al contents are much lower today than in previous decades. According to the electrical steel manufacturers, they made very little change in the basic chemistry used in standard, commercial types. International, national (EN- STN 10126) and (EN- STN 10165), EN-STN 10126 and company standards H-204 (Internal standard Embraco TST00H-204) determine only maximum specific losses (and often minimum polarization/throughput), but in principle they do not reduce the loss limit.

Conventional electromagnetic properties of electrical steels are defined by wattage losses, magnetic induction, and magnetic polarization. The mentioned properties are determined by microstructural and substructural parameters such as grain size and morphology, the density of crystallographic disorders, preferred crystallographic orientation, the chemical composition of the solid solution and the presence of secondary particles. Individual parameters used in the thermo-mechanical process of production of electrical steel directly influence the final magnetic quality of materials.

Most electrical equipment manufacturers, with the exception of the transformer and specialty applications manufacturers, require low core losses and high magnetic induction from the electrical steel. These magnetic properties are mainly influenced by grain size and crystallographic texture.

The effect of grain size on magnetic properties was first described in 1912 by W. E. Ruder, who discovered that hysteresis losses decrease as grain size increases. Since then, the effect of grain growth has been the subject of numerous scientific papers and literature. Hence, as the grain size increases, hysteresis losses

decrease, while eddy current losses increase. The result is an optimum grain size that minimizes the sum of hysteresis and eddy current losses. The optimum grain size varies depending on the chemical composition and texture. J. T. Park and J. K. Kim [6] specified optimum grain size of 100–150 μm for steels containing 1.85% and 3.2% Si. On the other hand, the texture also greatly affects hysteresis losses. The authors further claimed in their study that the material with a favorable texture exhibits lower core losses than the one with an unfavorable texture – despite having the same grain size. This indicates that losses can be further reduced by an appropriate texture. In view of the above, a key factor in the production and finishing of isotropic steels is the growth of grains to the optimum size with a favorable texture.

## THE EFFECT OF SHEARING ON THE DEGRADATION OF MAGNETIC PROPERTIES

When the sheet is sheared and the lamella shape is formed, the metal is separated, and the crystal lattice is disrupted. The properties of the material near the sheared edge are significantly altered. In 1971, Carlberg [7] first suggested that the area of degradation of properties near the sheared edge of an electrical steel strip can be considered as wide as 1 mm. Schmidt [8] identified a shear-affected area at a width of 0.35 mm with an increase in losses of 30-40% and a corresponding induction decrease of 70% at the same magnetic field strength. In 1992, T. Nakata [9] stated that the degradation of the magnetic properties of the strip of non-oriented silicon steel sheet due to shearing is in the region of 10 mm from the sheared edge and the deterioration is particularly significant 5 mm from the edge. Several other authors including F. Ossart, E. Hug, O. Hubert, C. Buvat, R. Billardon [10], and A. Kedous-Lebouc [11] paid attention to local degradation in the active part of the stator lamella sheared from an electrical steel sheet. Subsequently, V. Manescu et al. [12] and N. Takahashi [13], [14] compared the impact in terms of different shearing technologies.

In spite of different initial views, the average shear-affected area is generally considered to be equal to the thickness of the sheared material. The size of the affected area depends on parameters such as steel hardness, ductility, tensile strength, yield strength, surface insulation, grain size, shear clearance, and shearing tool geometry. Many authors researched microstructural changes during the recovery of distorted grains, e.g. Talbot [15] examining pure iron and Hu [16] silicon steel. Most of the works are devoted to restoring the magnetic properties after annealing in the area of deformation after shearing and rolling, see Landgraf [17].

Fig. 1 shows the principle of blanking process and Fig. 2 shows zones of a sheared surface.

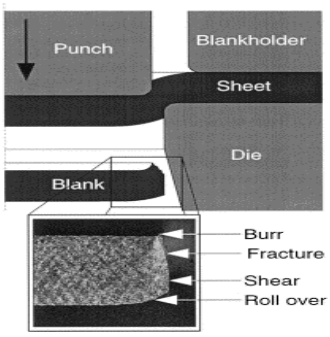


**Fig. 1 Scheme of the blanking process and a sheared surface profile**

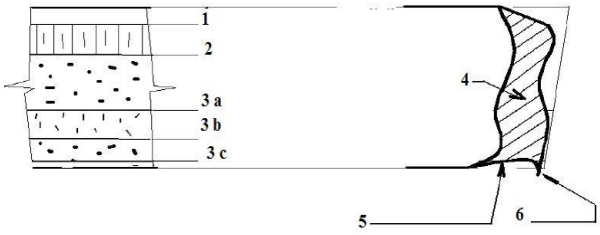


**Fig. 2 Zones of a sheared surface (1 – rollover, 2 – plastic shear, 3a – fracture, 3b – abrasion, 3c – fracture, 4 – hardened area, 5 – tool mark, 6 – burr)**

## MATERIAL AND METHODS

### Materials used in the experimental study

Thin electrical steel sheets with the following designations were used for experimental research: material B – steel ISOVAC M450 – 50K Voest Alpine, material C – steel M450 – 50K Arcelor Mittal and material E – steel M450 – 50PP Thyssen Krupp Bochum.

The chemical composition of the used steel sheets is given in Tables 1, 2 and 3. The materials differed mainly in the different silicon contents. For sheet B – ISOVAC M450 – 50K (Voest Alpine), the Si content was 0.574%, for sheet C – M450 – 50K (Arcelor Mittal) the Si content was 0.148% and for E – steel M450 – 50PP (Thyssen Krupp Bochum) the Si content was 1.630%.

**Table 1** Chemical composition of material – B [wt.%]

| C | Mn | Si | P | S | Al | Cu |
|---|---|---|---|---|---|---|
| 0.0059 | 0.506 | 0.574 | 0.034 | 0.0036 | 0.418 | 0.011 |
| **Ni** | **Cr** | **As** | **Nb** | **Mo** | **Co** | **Sn** |
| 0.010 | 0.019 | <0.001 | <0.002 | 0.003 | <0.002 | <0.002 |
| **Sb** | **W** | **B** | **Ca** | **Zr** | **$N_2$** | |
| <0.002 | <0.003 | <0.0002 | <0.0002 | <0.001 | 0.0017 | |

**Table 2** Chemical composition of material – C [wt.%]

| C | Mn | Si | P | S | Al | Cu |
|---|---|---|---|---|---|---|
| 0.0026 | 0.609 | 0.148 | 0.089 | 0.0075 | 0.117 | 0.017 |
| **Ni** | **Cr** | **As** | **Nb** | **Mo** | **Co** | **Sn** |
| 0.021 | 0.028 | <0.001 | <0.002 | <0.002 | 0.002 | <0.002 |
| **Sb** | **W** | **B** | **Ca** | **Zr** | **$N_2$** | |
| <0.002 | <0.003 | 0.0002 | <0.0002 | <0.001 | 0.0024 | |

**Table 3** Chemical composition of material – E [wt.%]

| C | Mn | Si | P | S | Al | Cu |
|---|---|---|---|---|---|---|
| 0.0027 | 0.209 | 1.630 | 0.046 | 0.0010 | 0.138 | 0.013 |
| **Ni** | **Cr** | **As** | **Nb** | **Mo** | **Co** | **Sn** |
| 0.018 | 0.030 | <0.001 | <0.002 | <0.002 | <0.002 | <0.002 |
| **Sb** | **W** | **B** | **Ca** | **Zr** | **$N_2$** | |
| <0.002 | <0.003 | <0.0002 | 0.0002 | <0.001 | 0.0056 | |

The mechanical properties were determined on standard specimens by a uniaxial tensile static test according to standard STN EN ISO 6982-1. From each type of tested sheet, five samples were taken for the uniaxial tensile test. The measured mechanical properties of the tested sheets are shown in Table 4.

**Table 4** Mechanical properties of the experimental electrical steels

| Direction | Material | $Rp_{0,2}$ [MPa] | $R_m$ [MPa] | $A_{80}$ [%] |
|---|---|---|---|---|
| 0° | B | 413 | 477 | 16.9 |
| 0° | C | 359 | 395 | 24.1 |
| 0° | E | 317 | 440 | 34.8 |
| **Direction** | **Material** | **$Rp_{0,2}$ [MPa]** | **$R_m$ [MPa]** | **$A_{80}$ [%]** |
| 90° | B | 403 | 480 | 17.5 |
| 90° | C | 358 | 398 | 25.9 |
| 90° | E | 315 | 442 | 34.4 |

Material B achieved an average ductility value A80 in the range of 16.9–17.5%. The ductility of material C ranged from 24.1 to 25.9% and the ductility of material E was 34.4–34.8%. For all materials examined, the ductility values measured in the direction perpendicular to the rolling direction and the ductility

values measured in the rolling direction were approximately the same. The materials showed no anisotropy of mechanical properties [18].
Sheets with different grain sizes were used for comparison. The microstructure of the sheets used in the experiment is shown in Fig. 3–5. The steel sheets B had a fine-grained structure (Fig. 3), while the sheets E had a structure with significantly larger grains (Fig. 5).

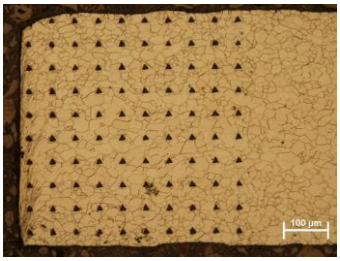


**Fig. 3 Microstructure of material B**

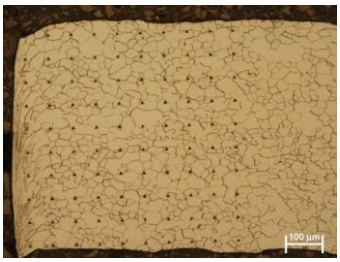


**Fig. 4 Microstructure of material C**

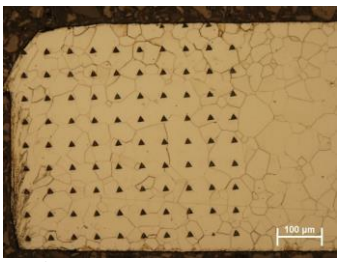


**Fig. 5 Microstructure of material E**

**Experimental setup, equipment, results and analysis**

Four shear gap values were chosen to investigate the dependence of the sheared surface quality on the shear gap. The chosen shear gap sizes were based on our previous research as 1%, 3%, 5% and 7% of the thickness of the sheared materials. The nominal thickness of all experimental materials was 0.5 mm.
The experiments were conducted by blanking in a progressive shearing tool with a spring-loaded guide plate and a guide stand (Fig. 6a). The tool was used in a hydraulic press with a nominal force of 400 kN.

**a)** **b)**

**Fig.6 a) Blanking tool, b) Specimen**

Table 5 shows the real values of the punch diameters when 1, 3, 5 and 7% shear gap was used. The dimensions of the punches were measured using a digital micrometer and Zeiss Calypso coordinate measuring machine (CMM). The diameters of the dies were constant: ø 25.013 mm and ø 15.049 mm.

**Table 5** Shear gap values and punch dimensions of the shearing tool

| Shear gap [%] | Diameter of outer punch [mm] | Diameter of inner punch [mm] |
|---|---|---|
| **1%** | 25.003 | 15.039 |
| **3%** | 24.983 | 15.019 |
| **5%** | 24.963 | 14.989 |
| **7%** | 24.943 | 14.969 |

The shape of the sheared surface on the outer perimeter of the blanks was investigated in the cutouts of an annular shape (Fig. 6b). An analysis of the outer surface of the blanks was performed with a Keyence microscope. The ratio of the plastic shear area to the gross area of the section zone was evaluated. The samples were observed around the sheared edge perimeter and evaluated in the rolling direction. Based on the observations, it can be stated that the shear area around the sheared edge perimeter was approximately the same for all blanks of a particular shear gap. The smallest deviations in the ratio of the plastic shear area to the gross section area were measured at a 1% shear gap. Significantly larger variations in the quality of the sheared surface around the perimeter of the blank were observed at a shear gap of 5% and 7%. Fig. 7–9 show the sheared surfaces of the investigated materials at different shear gaps [19], [20].

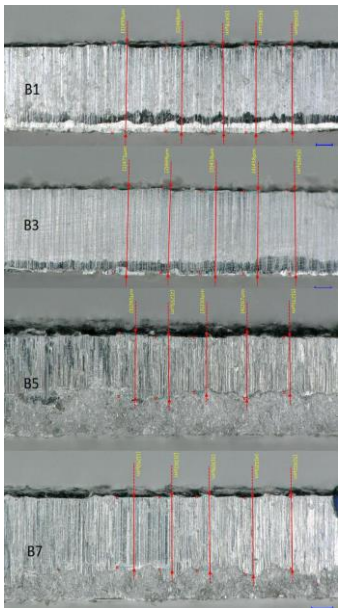


**Fig. 7 Examined sheared surfaces of material B at different shear gap values**

It can be concluded from the analysis of the impact the shear gap on the quality of the shear area of the examined material B that when a 1% and a 3% shear gap is used, then the entire shear area is formed by plastic shearing (plastic deformation). At these shear gaps, the material was not exposed to shear stress and there were no visible signs of shear stress around the perimeter of the cut material. At a 5% shear gap, the smallest area of the plastic shear was measured, which was about 50% of the gross area of the section. Paradoxically, with a shear gap of 7%, the plastic shear area of this material increased to about 65%. This was probably due to a deviation in the punch cylindricality at the measured location.

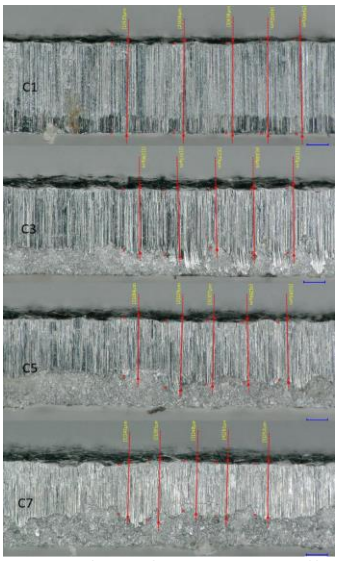


**Fig. 8 Examined sheared surfaces of material C at different shear gap values**

From the analysis of the impact of the shear gap on the quality of the shear area of the examined material C, it can be concluded that at a 1% shear gap, the entire shear area is formed by plastic shearing (plastic deformation). There was no fracture zone at this shear gap at all. At a 3% shear gap, the plastic shear value was measured to be 100–80% of the gross area of the section. At this shear gap, uneven values of the size of the plastic shear occurred around the perimeter of the blank. At a 5% shear gap, the plastic shear area was more uniform over the entire perimeter and represented 65–70% of the gross area of the section.
At the 7% shear gap, the plastic shear area of the material was less uniform around the perimeter and represented 60–65% of the gross area of the section.

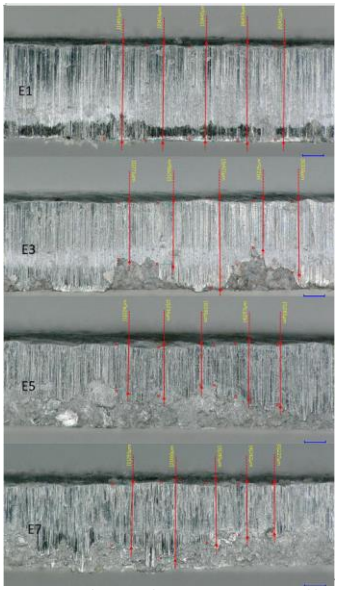


**Fig. 9 Examined sheared surfaces of material E at different shear gap values**

It can be concluded from the analysis of the impact of the shear gap on the quality of the sheared surface of the investigated material E that at a 1% shear gap, the entire shear area is formed by plastic shearing (plastic deformation). There was no shear stress at this shear gap at all. At a 3% shear gap, the plastic shear area was measured to be about 90–50% of the gross area of the section. At this shear gap, an uneven plastic shear area occurred around the perimeter of the blank. During die-cutting, large grains were torn off the perimeter of the material.

The same phenomenon was also observed at 5 and 7%. The plastic shear area was uneven around the perimeter of the blank and ranged from 100 to 50%. Fig. 10 and 11 enable us to compare the shear area of the investigated materials at 1% and 5% shear gap. As stated above, at a 1% shear gap, all experimental materials were exposed to plastic shear around the perimeter of the blank. At this shear gap, the quality of the sheared surface is not influenced by the chemical composition of the sheet nor by the mechanical and plastic properties of the investigated electrical steel sheets.

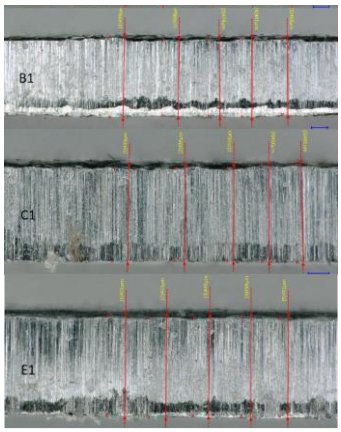


**Fig. 10 Sheared surfaces of investigated materila at 1% shear gap**

After analyzing the sheared surfaces of the specimens at the 5% shear gap, it can be stated that the plastic shear area was in the range of 100–50% of the gross area of the section. The lowest plastic shear value was measured for material B, whose ductility values were the lowest. The shear area of this material was uniform around the perimeter. For material C, the plastic shear value at a 5% shear gap ranged from 70 to 65% and it was less uniform. Material E had the highest ductility of all the examined materials, the plastic shear area at this shear gap ranged from 100 to 50%. Such a large dispersion of the plastic shear values is caused by tearing off large grains of material during die cutting [21], [22].

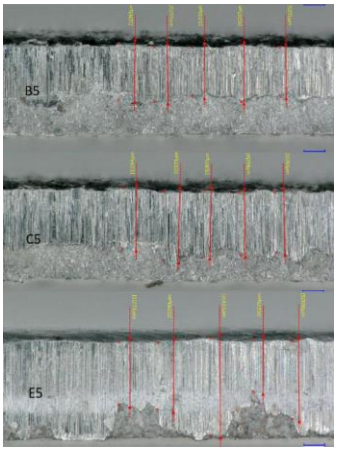


**Fig. 11 Sheared surfaces of investigated materials at 5% shear gap**

**DISCUSSION**

In the experimental research into the impact of the shear gap on the quality of the sheared surface, materials with different chemical composition, mainly differing in silicon content were selected. The examined materials had different mechanical and plastic properties. The ductility of the examined materials ranged from 16 to 35%. The materials also differed in the manufacturing method and grain size. All investigated materials exhibited minimal anisotropy of the plastic properties (they were almost isotropic), which is a very important factor in terms of punching circular blanks. From the obtained results it can be concluded that at a 1% shear gap, the chemical composition, plastic properties or material structure

do not affect the quality of the sheared surface as indicated by the size of the plastic shear area. The plastic shear area of all materials examined was 100% of the gross area of the section.

At the shear gap of 3%, the impact of the material structure began to be obvious. The plastic shear areas reached 100% only for material B, for the other examined materials, they ranged from 80 to 50% of the gross area of the section. Material E, having the highest ductility, exhibited the lowest and least uniform values of the plastic shear area. These plastic shear areas were somewhat distorted in this material because large grains of material were torn off during die cutting.

At 5 and 7% shear gap, all materials showed a decrease in the plastic shear area to 70–50% of the gross area of the section. With these shear gaps, the inhomogeneity of the plastic shear area around the perimeter of the blank was lower for all examined materials. Even at these shear gaps, the greatest inhomogeneity of the plastic shear areas was observed in the material with the highest ductility (material E).

## CONCLUSION

Based on the experimental results of the impact of the shear gap on the quality of the sheared surface when die-cutting electrical sheets of different grades, the following conclusions can be drawn:

- when shearing electrical steel sheets in a tool with a shear gap of 1% of the material thickness, neither the chemical composition nor the mechanical and plastic properties affect the quality of the sheared surface, which is characterized by the size of the plastic shear area,
- blanking materials in a tool with a shear gap of 3% of the material thickness results in a decrease in the size of the plastic shear area, especially for materials with a higher ductility value,
- when die-cutting sheets in a tool with a shear gap of 5 and 7% of the material thickness, the plastic shear areas decreased for all materials examined. The greatest inhomogeneity of the plastic shear area was measured for the sheets with the highest ductility. In these sheets, the inhomogeneity was mainly caused by the large grains of material being torn off during die cutting.

Based on the performed experiments, it is recommended to use shear gaps in the range of 1–2% of the material thickness in the blanking tools for trouble-free cutting of circular cut-outs made of electrical steel sheets (rotors and stators of electric rotating machines).

**Acknowledgments:** Authors are grateful to APVV for support of experimental work under grant APVV-14-0834 and APVV-17-0381.

## REFERENCES

1. [11.4.2006] http://www.worldsteel.org/steel-by-topic/statistics/steel-statistical-yearbook.html, Steel Statistical Yearbooks 2010 to 2019
2. E. Spišák, J. Slota, J. Majerníková: Chemické listy, 105, 2011, p. 485-487
3. R. Bidulsky, J. Bidulska, P. Petrousek, A. Fedorikova, E. Dudrova, M.A. Grande: Acta Physica Polonica A, 131(5), 2017, 1367-1370. https://doi.org/10.12693/APhysPolA.131.1367.
4. R. Bidulsky, J. Bidulska, R. De Oro, E. Hryha, M. Maccarini, I. Forno, M.A. Grande: Acta Physica Polonica A, 128(4), 2015, 647-650. https://doi.org/10.12693/APhysPolA.128.647.
5. R. Bidulsky, M.A. Grande, L. Ferraris, P. Ferraris, J. Bidulska: Acta Physica Polonica A, 118(5), 2010, 802-803. https://doi.org/10.12693/APhysPolA.118.802.
6. J. T. Park, J. K. Kim: Recrystallization, Grain growth and texture evolution in nonoriented electrical steel, Mater. Sci. Forum, 10(1), 2007, 657-664. https://doi.org/10.4028/www.scientific.net/MSF.558-559.657.
7. P. M. Carlberg: The cutting of electrical steel sheets, In.: *Translation of presentation at the Kernkontoret Punching Conference*, Stockholm, November 1971.
8. K. H. Schmidt: Journal of Magnetism and Magnetic Materials, 2, 1975, 136. https://doi.org/10.1016/0304-8853(75)90116-X.
9. T. Nakata, M. Nakano, K. Kawahara: IEEE Transactions on Magnetics, 7, 1992, 453-457. https://doi.org/10.1109/TJMJ.1992.4565422.
10. F. Ossart, E. Hug, O. Hubert, C. Buvat, R. Billardon: IEEE Transactions on Magnetics, Vol. 36, 2000, 3137-3140. https://doi.org/10.1109/20.908712.
11. Kedous-Lebouc, B. Cornut, J. C. Perrier, Ph. Manfé, Th. Chevalier: Journal of Magnetism and Magnetic Materials, 254-255, 2003, 124-126. https://doi.org/10.1016/S0304-8853(02)00803-X.
12. V. Manescu, G. Paltanea, H. Gavrila, I. Peter: The Influence of Punching and Laser Cutting Technologies on the Magnetic Properties of Non-oriented Silicon Iron Steels, In.: *International Symposium on Fundamentals of Electrical Engineering*, University Politehnica of Buchurest, Nov. 2014
13. N. Takahashi, H. Morimoto, Y. Yunoki, D. Miyagi: Journal of Magnetism and Magnetic Materials, 320, 2008, e925-e928. https://doi.org/10.1016/j.jmmm.2008.04.170.
14. Yujing Liu, S. K. Kashif, A. M. Sohail: Engineering considerations on additional iron losses due to rotational fields and sheet cutting, In.: International Conference on Electrical Machines, 2008.
15. J. Talbot: *Recovery and Recrystallization of Metals*, Interscience, New York, 1963, p. 269.
16. H. Hu: *Recovery and Recrystallization of Metals*, Interscience, New York, 1963, p. 311.
17. F. J. G. Landgraf, M. Emura: Journal of Magnetism and Magnetic Materials, 242, 2002, 152-156. https://doi.org/10.1016/S0304-8853(01)01184-2.
18. J. Majerníková, E. Spišák: Applied Mechanics and Materials, 474, 2014, 279-284. https://doi.org/10.4028/www.scientific.net/AMM.474.279.
19. J. Majerníková, E. Spišák: Advances in Science and Technology Research Journal. 11(4), 2017, 141-146. https://doi.org/10.12913/22998624/78168.
20. E. Spišák, Ľ. Kaščák, J. Majerníková, M. Džupon: Strength of Materials, 49(4), 2017, 605-611. https://doi.org/10.1007/s11223-017-9904-2.
21. E. Spišák, J. Majerníková, Ľ. Kaščák: Advances in Science and Technology Research Journal. 10(32), 2016, 248-253. https://doi.org/10.12913/22998624/65759.
22. Záverečná správa projektu APVV-14-0834, Technical University of Košice, 2018 (in Slovak).

OPEN ACCESS

# ACTA METALLURGICA SLOVACA

2020, VOL. 26, NO. 2, 54-62

**RESEARCH PAPER**

## DRY SLIDING WEAR AND SURFACE MORPHOLOGICAL EXAMINATION OF AN ALUMINIUM MATRIX COMPOSITE REINFORCED WITH PALM KERNEL SHELL

*Francis Odikpo Edoziuno[1]*, Benjamin Ufuoma Odoni[2], Francis Ireti Alo[3], Cynthia Chinasa Nwaeju[4]*

*[1,2]Department of Metallurgical Engineering, Delta State Polytechnic, P.M.B. 1030 Ogwashi-Uku, Nigeria.*

*[3]Department of Material Science and Engineering, Obafemi Awolowo University, Ile-Ife, Nigeria.*

*[4]Department of Mechanical Engineering, Nigeria Maritime University, Okerenkoko, Warri, Delta State, Nigeria.*

** Corresponding Author's email: francisedoziuno@gmail.com, Tel. +234806 342 2650; Department of Metallurgical Engineering, Delta State Polytechnic, P.M.B. 1030 Ogwashi-Uku, Nigeria.*

Received: 26.04.2020
Accepted: 22.05.2020

**ABSTRACT**

The wear resistance and microstructural features of aluminium AA6063 based composites reinforced with seven different mass fractions of palm kernel shell (PKS) particles (0, 2.5, 5, 7.5, 10, 12.5 & 15wt%) fabricated by stir-casting, were characterized using pin-on-disk tribometer, optical microscope and image analysis. Image analysis revealed both the particle size and shape descriptors for the composites microstructural features. The average grain sizes of all the composites were higher than that of the unreinforced AA6063 matrix. Wear test conducted under dry sliding condition show that the volume reduction and specific wear rate increased to a maximum at 5wt% PKS addition and then decreased to the lowest level at 10wt% PKS. Subsequent addition of PKS above 10wt% yielded a further increase in the composites volume loss and specific wear rate. Composite sample reinforced with 10wt% PKS exhibited wear resistance response better than that of the unreinforced alloy. Image analysis afforded a comprehensive understanding of the microstructural features of the composites which influenced their behaviours.

**Keywords:** ImageJ; Image analysis; dry sliding wear; AA6063; Palm Kernel Shell; Aluminium matrix composites.

### INTRODUCTION

The aim of developing metal matrix composite is to combine the desirable properties of the metal such as lightweight, high ductility, electrical and thermal conductivities with the properties of the reinforcement such as low coefficient of thermal expansion, high stiffness, and strength with abrasion resistance to produce material with a combination of desired physical and mechanical properties [1]. Aluminium metal matrix composites (AMMCs) are engineered materials made by incorporating single or hybrid non-metallic reinforcement(s) into aluminium or its alloy to tailor the properties such as strength, hardness, stiffness, electrical and thermal conductivity and various other properties. AMMCs found applications in aerospace, automotive, defence, marine, thermal management, electrical and electronic as well as sports goods. Aluminium alloys 2000, 5000, 6000 and 7000 series are the most frequently utilised matrix in the fabrication of AMMCs [2, 3]. AMMCs offer high strength to weight ratio, improved thermal conductivity, abrasion/wear resistance, creep resistance, dimensional stability and exceptionally good stiffness-to-weight ratio. Also, they have better high temperature performance [4–8]. Aluminium AA6063 is a class of aluminium alloy 6000 series having silicon and magnesium as the major alloying elements. Their major areas of application are in the automobile and aeronautic industries.

Wear phenomenon could be described as a progressive loss of materials by solid surfaces in dynamic contact [9–12]. The wear of composite materials have been classified into abrasive wear, adhesive wear, fatigue wear, erosive wear, fretting wear, oxidative wear and corrosive wear, depending on the mechanism of materials removed from the surface of bodies in contact or relative motion [9, 10, 13, 14]. In a sliding wear process, materials are removed by the dynamic interaction of two surfaces in relative contact, resulting in dimensional loss and material's volume reduction [9].

Materials' physical and mechanical properties are derived from their microstructural characteristics [15]. The development and use of automatic image analyzing tools and techniques for determining microstructural characteristics of materials have greatly reduced the rigour and tediousness associated with manual techniques [16]. Image analysis is concerned with accurately quantifying the microstructural features. Quantitative analysis of materials' microstructural features can be achieved using image analysis software. Either optical or scanning electron microscope micrographs can be used during image analysis [17, 18]. More commercial software programs, such as Amira, Comsol multiphysics, imageJ, etc., are available for the analysis of microstructural features of engineering materials [19, 20]. Image analysis is generally concerned with the acquisition of quantitative information and description of various parameters of the microstructure of a material such as determination of percentage fraction of phases or phase quantities, grain size estimation, grain shape, circularity and spatial distribution of microstructural elements observed using microscopic techniques [19, 21]. Microstructures with similar descriptors have similar materials properties [22]. Circularity or roundedness, for instance, is calculated as a shape parameter index in the ImageJ software. This image analysis software program supports standard image processing functions such as logical and arithmetical operations between images, contrast manipulation, convolution, Fourier analysis, sharpening, smoothening, edge detection, and median filtering. It does geometric transformations such as scaling, rotation, and flips. The general steps for materials structural analysis involves; surface preparation (cutting, grinding, polishing and etching), microscopic examination and image acquisition, image processing, quantitative image analysis (size, shapes and distribution of grains) and interpretation of results [19]. Image analysis had been utilized by researchers to quantify and measure the concentration of surface discolouration in laser-nitrided titanium alloy surface using the colour threshold function [23], analysed and compare the structure of two construction steels [19], quantify and estimate the microstructural parameter of ferritic-martensite dual phase steel [21]. Leica Qwin image analysis system was used to measure pore structures and pore distribution in aluminium powder metallurgy alloy [24]. The experimental demonstration has found image analysis procedure to be very effective in the measurement of materials grain size, pore structures and distribution and recommended for application in the ceramic and metallic industries, especially in powder metallurgy sintering operations [12, 24–27].

There is a research-established correlation of materials' microstructure with wear loss and hardness. It was shown that microstructural characteristics affect wear behaviour of sintered steel [27]. Lower wear loss is found to correlate with higher hardness and superior microstructure (one having higher dendrite density).

Conversely, higher wear loss correlates with lower hardness and poor microstructure [23]. This paper describes an investigation of the dry sliding wear behaviour of aluminium AA6063 reinforced with particles of palm kernel shell and microstructural analysis of the optical micrograph using image analysis software package.

## MATERIALS AND METHODS

### Collection and Preparation of Reinforcement Material

Palm kernel shell was obtained from an oil mill in Agbor, Delta State, South-South of Nigeria. The collected palm kernel shell (PKS) were washed with warm water, dried in direct sunlight for two weeks and grinded to a fine powder using the normal grain (wheat, corn, beans, etc.) grinding machine at the Ogwashi-Uku market. Particle size analysis of the palm kernel shell particle was carried out in Metallurgical Engineering laboratory, Delta State Polytechnic, Ogwashi-Uku. 100g of the PKS was placed unto a set of sieves arranged in descending order of fineness and shaken for 15mins to achieve complete classification. The PKS particles retained beneath the 212µm sieve was utilized in the research. The powder PKS was used in the unashed and untreated condition, as some other researchers had investigated it as a reinforcement in the processed and treated conditions [28–30].

### Production of Composite by Stir Casting

The metal matrix composite was fabricated in the metallurgical Engineering laboratory of Delta State Polytechnic, Ogwashi-Uku, using the stir casting method. The sample was produced by varying the weight per cent of the reinforcing material (PKS) particles in the range of 0 to 15 wt.% at 2.5 wt.% interval, while the balance is aluminium alloy AA6063 matrix. The aluminium alloy was charged into a preheated stainless steel melting pot placed in an electric resistance furnace. The furnace was heated to ±700 ºC for 3 h. The PKS particles were preheated to 50 ºC in an oven for 3 h before they were added to the molten aluminium to improve the wettability and harmonize the temperature. The furnace temperature was first raised to 750 ºC to melt the alloy completely and then cooled to 600 ºC to keep the melt in a semi-solid state. At this stage, the preheated palm kernel shell particles were added and mixed manually using a steel stirring rod according to [29, 31]. After manual mixing and homogenisation, the composite slurry was placed back in the furnace and reheated to a temperature of 750 ºC and then poured into a preheated cylindrical mild steel mould with the dimension of length 200 mm x 16 mm diameter. The unreinforced aluminium AA6063 was also cast and used as the control sample for comparison.

### Dry Sliding Wear Test

The wear test was carried out at room temperature on a Pin-on-Disc tribometer under dry sliding condition. A 10N constant load (N) was applied on all the specimens with dimension 40mm x 10mm x 6mm while sliding distance varied during the test. The procedure during the wear test involved; determination of the initial weight of the specimen, inserting and fixing the specimen on the specimen holder, applying the constant load on the supporting rod so that the stylus pin made firm contact with the specimen, turning the electric motor on to rotate the disc for just 2000 revolution cycles at a rotation speed of 200rpm. The specimen is finally weighed and the sliding distance covered measured. During sliding wear test using pin-on-disc equipment, the sliding speed of the wear process is dependent on the revolution of the disc and the contact point between the pin and the centre of the disc [32]. Wear evaluation was carried out by expressing the friction effects in terms of material volume loss ($mm^3$) as a function of the sliding distance and the applied load. The specific wear rate, **($W_S$)** was computed from the test results/parameters using equation (1) [33]. The magnitude of wear resistance ($W_R$) given in equation (3) is determined by taking the inverse of wear rate [30, 34], equation (2).

$$W_S = \frac{Volume\ Loss}{Applied\ Load \times Sliding\ Distance} \quad (1)$$

$$Wear\ rate\ \left(mm^3/_{Nm}\right) = \frac{Volume\ loss\ (mm^3)}{Sliding\ Distance\ (m)} \times 1000 \quad (2)$$

$$W_R = \frac{Sliding\ Distance\ (S)}{Volume\ Loss(V_{loss})} \times 1000 \quad (3)$$

### Morphological Examination Using Optical Microscope

The samples for optical metallographic examination were prepared and optical microscopy (OM) was carried out following the procedure described in [19, 35]. The metallographic characterization was carried out at 640× magnification. It should be noted, that a major condition for accurate image analysis is correct surface preparation of metallographic samples so that individual microstructural features would be sufficiently contrastive during image analysis [16, 36]. Inadequate specimen's preparation and wrong choice of etching technique were identified as major problem in using image analysis to reveal microstructural features [26].

### Image Analysis of the Microstructure

ImageJ software package was used for image processing and image analyses. This automatic image analysing software is capable of defining and counting object in the picture, analysing their surface, length, boundaries, moments, quantifying of grains and measurement of grain sizes, the volume fraction of phase and depositing the results of analyses to spreadsheet data files [18]. The following procedures with detailed description given in [22, 23, 37, 38] were applied in conducting the ImageJ analysis: firstly, the surface morphology of the composites and the unreinforced aluminium alloy samples was captured by an optical microscope and exported as a high-resolution micrograph. Then the high-resolution micrograph was imported in the ImageJ software for image analysis. Finally, various functions and tools in imageJ software program were employed for specific measurement and analysis. Flowchart of the detailed procedures for the Image analysis is given as a block diagram in figure 1.

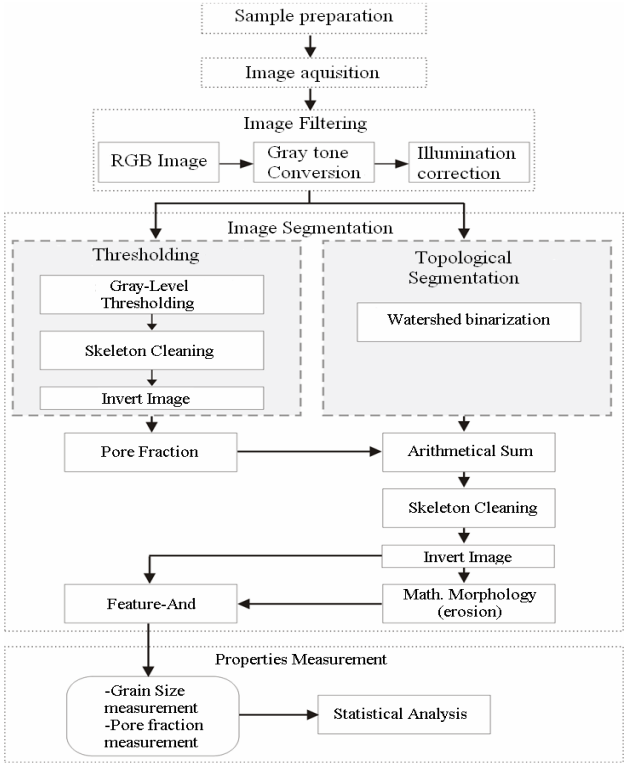


**Fig. 1** Block diagram depicting the imageJ analysis procedure adapted from [25].

## RESULTS AND DISCUSSION

### Wear Behaviour of PKS/AA6063 Matrix Composites

The effects of reinforcement concentration applied normal load and sliding speed on the dry sliding wear properties (weight loss, volume loss, specific wear rate and wear resistance) are discussed in this investigation. Table 1 gives the result of the wear test and the sliding wear parameters. Graphical analysis of the influence of the reinforcement concentration (% weight fraction) on the specific wear rate, volume loss and wear resistance of the PKS reinforced aluminium alloy AA6063 matrix composites are given in Figures 2 – 7.

**Table 1** Wear parameters and results of dry sliding wear test

| Sample | Weight loss (g) | Sliding Distance (mm) | Volume Loss ($mm^3$) | Specific Wear Rate ($mm^3/Nm$) | Wear Resistance ($mm/mm^3$) |
|---|---|---|---|---|---|
| **Control** | 0.0015 | 3.4 | 0.79 | 0.27 | 4303.80 |
| **2.5% pks** | 0.0057 | 2.5 | 2.64 | 0.66 | 946.97 |
| **5% pks** | 0.0091 | 2.6 | 4.60 | 1.20 | 565.22 |
| **7.5%pks** | 0.0076 | 2.4 | 2.11 | 0.51 | 1137.44 |
| **10% pks** | 0.0009 | 2.4 | 0.53 | 0.13 | 4528.30 |
| **12.5% pks** | 0.0033 | 2.7 | 2.09 | 0.56 | 1291.87 |
| **15%pks** | 0.0031 | 2.8 | 2.33 | 0.65 | 1201.72 |

It could be readily observed from Table 1 that the weight loss of the composites increased as the reinforcement content increases to a maximum at 5% PKS and then decreased to a minimum at 10% PKS content. Despite that, the applied normal load was constant at 10N during the tribological test. Generally, the composites with higher per cent weight fraction of the reinforcement (10, 12.5 & 15%), recorded lower weight loss during the sliding wear experiment. While, those with lower content of the particulate reinforcement (2.5, 5 & 7.5%) have a higher loss in weight during wear test.

Considering the influence of the reinforcement concentration on the specific wear rate, and volume loss of the AA6063 matrix composites shown in Figures 2 & 3, it could be noticed that the volume reduction and specific wear rate increased to a maximum at 5wt% PKS content and then decreased to the lowest level at 10wt% PKS. Subsequent addition of PKS above 10wt% resulted in a further increase in the composites volume loss and specific wear rate. The composite sample reinforced with 10wt% PKS has a specific wear rate and volume loss far lower than that of the unreinforced alloy.

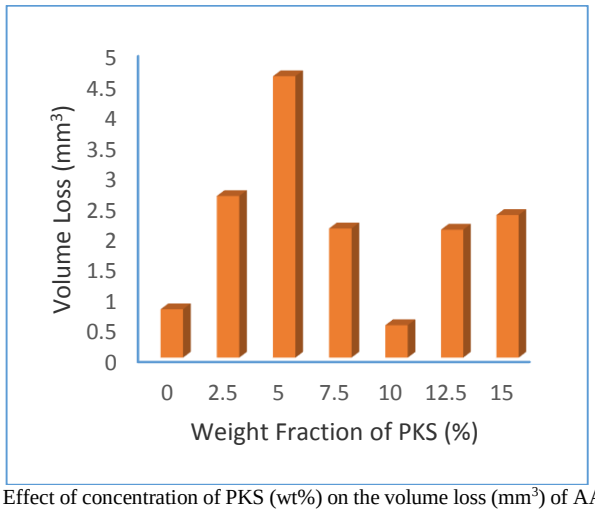


**Fig. 2** Effect of concentration of PKS (wt%) on the volume loss ($mm^3$) of AA6063 matrix composites during sliding wear test

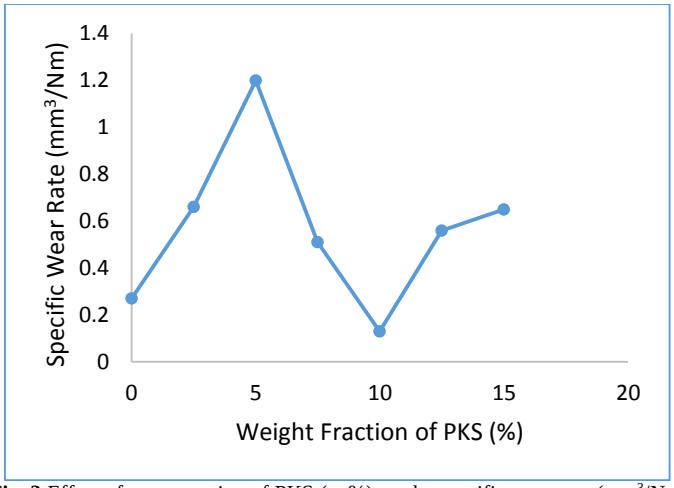


**Fig. 3** Effect of concentration of PKS (wt%) on the specific wear rate ($mm^3/Nm$) of AA6063 matrix composites during sliding wear test

The influence of the reinforcement weight content on the sliding distance covered during the dry sliding wear experiment is analysed in Figure 4. Evaluation of the figure revealed that the sliding distance covered reduced progressively from 3.5mm to 2.4mm, as PKS particles were added to the aluminium alloy matrix, despite that all the specimen were rotated just 2000 cycle at the rotation speed of 200rpm. This could be as a result of the frictional effect of the composites surface roughness, unlike the smooth-surfaced control sample. This is also corroborated by the average grain sizes of the microstructure obtained by image analysis (Table 2), which increased as more PKS were added to the AA6063 matrix. As expected, the composite sample reinforced with 10wt% PKS covered the lowest sliding distance during the abrasive sliding.

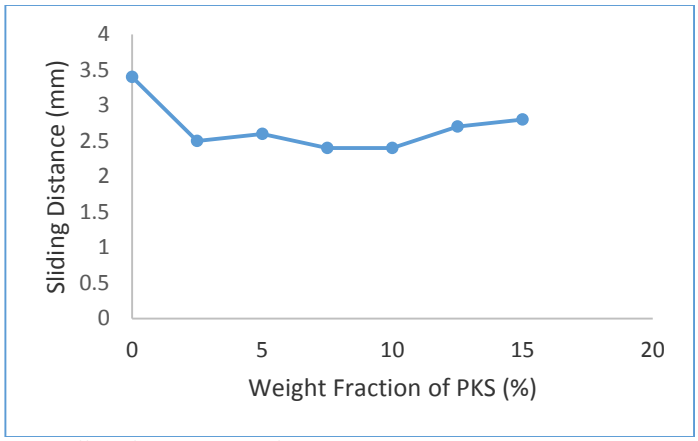


**Fig. 4** Effect of concentration of PKS (wt%) on the sliding distance (mm) covered during sliding wear test

In figure 5 is depicted, the impact of reinforcement concentration (wt%) on the sliding wear resistance of the composites. All the composites samples have lower wear resistance than the unreinforced AA6063 alloy, except the 10wt% PKS reinforced sample. Maximum wear resistance was recorded at 10wt% PKS content.

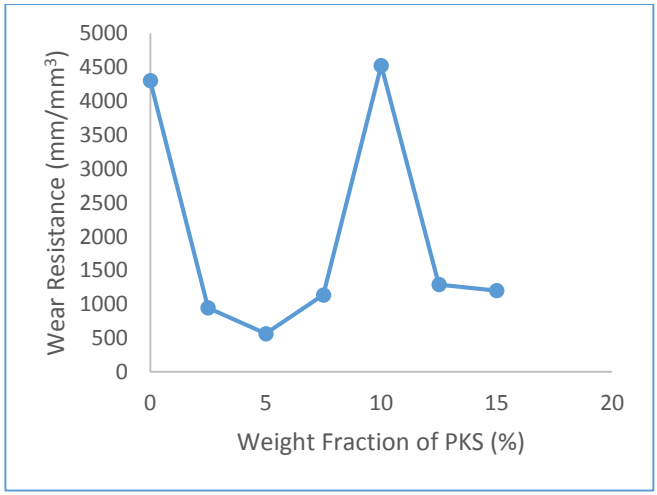


**Fig. 5** Effect of concentration of PKS (wt%) on the wear resistance (mm/mm$^3$) of AA6063 matrix composites during sliding wear test

**Image Analysis of PKS/AA6063 Matrix Composites**

Relevant quantitative descriptors (stereological parameters) are used in characterizing the dimensional and morphological characteristicss of materials. The quantitative description of the microstructure involves the use of a set of numbers that define density, size, shape, and spatial arrangements (three-dimensional properties) of the microstructural features [22]. These quantitative descriptors are based on the theory of geometrical probability and can be obtained from measurements carried out on the microstructural image using specific functional tools of the image analysis software package. The most common quantitative microstructural measurement is that of the grain size of materials [22]. Analyze particle function was used to determine the perimeter, the grain counts, average size, %Area, circularity, solidity, etc. Composite sample reinforced with 15wt% PKS recorded the maximum count of grains, while the 5wt% PKS reinforced sample has the lowest grain count. The average particle sizes of 5, 7.5 and 15wt%PKS reinforced composites were higher than that of the unreinforced AA6063 matrix, which may correlate to the high wear rate observed for those reinforcement weight fractions. The quantitative results in Table 2 display the particle size descriptors, which were used to compute the various particle shape descriptors given in Table 3.

The circularity, a popular shape factor/parameter allows for evaluating the shape of grains. Circularity, C, is a dimensionless value, which can be used to estimate the degree to which the particle resembles a circle, with consideration of the smoothness of the perimeter. It is the ratio of the perimeter of a circle of the same area as the particle to the perimeter of the particle. This implies that circularity is a measurement of both the form and roughness of the particle. Thus, if a particle is not perfectly round, or a smooth circle, the circularity value will be lower [24, 39]. The shape descriptors in Table 3 revealed that the unreinforced aluminium alloy matrix has the highest value of circularity, closely followed by the 15wt% PKS reinforced composite. Feret's diameters characterize the particles outer horizontal and vertical dimensions; length and width (FeretX and FeretY). Aspect ratio, AR is defined as the ratio of the Feret's minimum length to the Feret's maximum length. Thus, as the width and length of the shape approach the same value, the aspect ratio approaches one [39]. This does not necessarily mean the shape is circular, though a perfect circle will have an aspect ratio of 1.0 [24]. Often, very symmetric shapes like square, regular octagon, equilateral triangle and symmetric cross, have a very high aspect ratio. Elongated shapes have lower values of aspect ratios [22]. From Table 3, the AR of the unreinforced alloy is higher than that of the PKS reinforced AA6063 matrix. It also has the lowest elongation ratio of 1.796. The highest elongation ratio of 2.153 was obtained by the composite sample reinforced with 7.5wt% PKS, which also have the lowest AR of 0.464. When a shape becomes less smooth or more irregular (or rougher), the perimeter of the shape may increase very quickly, depending on the size and number of the irregularities in the shape contributing to the roughness [39]. The irregularity of the unreinforced alloy was highest followed by the 7.5wt% PKS reinforced composite. Equivalent circle diameter (ECD) is the diameter of the circle having the same area as the area of the particle. Solidity, S, is a dimensionless value which measures the overall concavity of a particle. It can be defined as the image area, A, divided by the convex hull area, Ac. This implies that, as the particle becomes more solid, the image area and convex hull area tend to approach each other, resulting in a solidity value of unity. Conversely, as the particle shape digresses from a closed circle, the convex hull area increases and the computed solidity decreases. As a shape becomes rougher or less solid, the solidity value will approach zero. Conversely, shapes that are very smooth, and rounded have solidity values that approach one. From Table 3, the shape of the particles of the composite reinforced with 7.5%PKS is more rounded than other samples.

**Table 2** Summary of Image Analysis Results of Particle Size (Size Descriptors) for AA6063/PKS Composites and the Unreinforced AA6063

| Sample | Slice | Grain Count | Total Area | Average Size(μm) | % Area (A) | Perimeter (P) | Feret (F) | FeretX | FeretY | Feret Ange | MinFeret (mF) |
|---|---|---|---|---|---|---|---|---|---|---|---|
| **Control** | Black & White Threshold | 546 | 33476 | 61.311 | 45.272 | 34.731 | 6.126 | 148.354 | 106.147 | 120.482 | 3.411 |
| **5wt% PKS** | Black & White Threshold | 433 | 27003 | 62.363 | 41.372 | 38.704 | 8.849 | 147.083 | 125.353 | 128.681 | 4.184 |
| **7.5wt%PKS** | Black & White Threshold | 481 | 37852 | 78.694 | 45.946 | 39.593 | 7.834 | 147.981 | 143.657 | 117.873 | 3.638 |
| **15wt% PKS** | Black & White Threshold | 758 | 50341 | 66.413 | 40.861 | 27.847 | 6.869 | 176.017 | 165.468 | 136.986 | 3.281 |

**Table 3** Microstructural Parameters and Shape Descriptors of AA6063/PKS Composites and the Unreinforced AA6063 Obtained from the Image Analysis Results

| Sample | Circularity | Irregularity | Solidity | Aspect Ratio (AR) | Elongation Ratio (ER) | ECD |
|---|---|---|---|---|---|---|
| **Control** | 0.797 | 5.611 | 0.83 | 0.557 | 1.796 | 7.592 |

| | | | | | | |
|---|---|---|---|---|---|---|
| **5wt% PKS** | 0.742 | 4.374 | 0.796 | 0.473 | 2.115 | 7.258 |
| **7.5wt%PKS** | 0.772 | 5.054 | 0.845 | 0.464 | 2.153 | 7.649 |
| **15wt% PKS** | 0.786 | 4.054 | 0.827 | 0.478 | 2.094 | 7.213 |

ECD is equivalent circle diameter.

Figure 6a-d show the original images of AA6063, AA6063/5wt% PKS, AA6063/7.5wt% PKS and AA6063/15wt% PKS composites taken with metallurgical Optical microscope. The composites photomicrographs (Figure 6c-d) show a good dispersion of the PKS particulate reinforcement in the Al-Mg-Si

alloy matrix with small areas of reinforcement particles agglomeration, which characterizes stir-cast metal matrix composites [40]. There are areas of discolouration observable in the original optical micrographs running across grain boundaries and masking the microstructural features of the base alloy and composites (Figure 6). Image processing (image- colour adjust and threshold, noise elimination) of the original micrographs, produced a uniform surface colour in the images and reveal contrastive microstructural features (Figures 7 & 8).

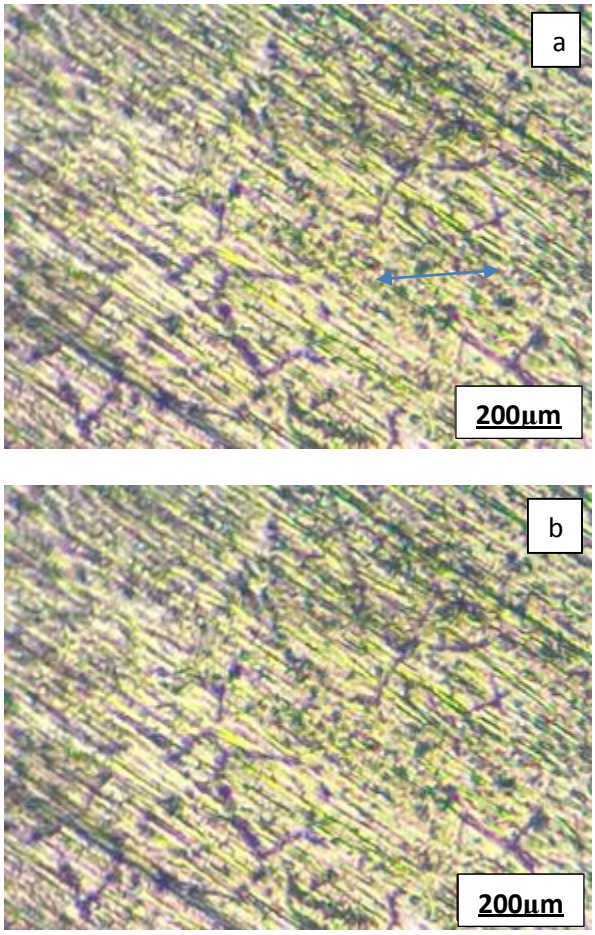


**Fig. 6** Original optical micrographs of (a) Unreinforced AA6063, (b) AA6063/5wt%PKS, (c) A6063/7.5wt%PKS and (d) AA6063/15wt%PKS Composites at 640× magnification

Automatic thresholding is an important parameter in image analysis used to determine the division and segment between grains and grain boundaries. Threshold function is applied to determine the surface fraction indicated by the ratio of colour to the general surface of the entire image. According to ASTM standards E112-96 and E1382-97 requirements, the threshold is adjusted to detect either the grain interior or grain boundaries [16, 36]. Figures 7 & 8 reveal the processed and thresholded images of the reinforced and unreinforced AA6063 alloy. To obtain an image with a clear and accurate segmentation of grains and grain boundaries, the processed and thresholded images of Figure 7 were further subjected to noise elimination and conversion to binary form (black and white threshold), which is useful for subsequent quantitative and qualitative measurements during image analysis and microstructural descriptions. Small particles or matrix inside the grains are considered noise and must be eliminated. It could be observed that the grains of the micrographs in Figure 8 occupy differentiated homogenous area after noise elimination. There is the precipitation of larger, contrasting and more rounded grain sizes, especially in Figure 8d. Figure 10 reveals the phase fraction or volume of the shaded area, which are shown quantitatively in Table 2 as the % Area. It shows the particle distribution in both the reinforced and unreinforced matrix. While Figure 9a-d depict the interactive 3D surface plot of the particle distribution. The colour intensity on the 3D surface plot gives a graphic vision and description of the observed surface morphology of the composites [19].

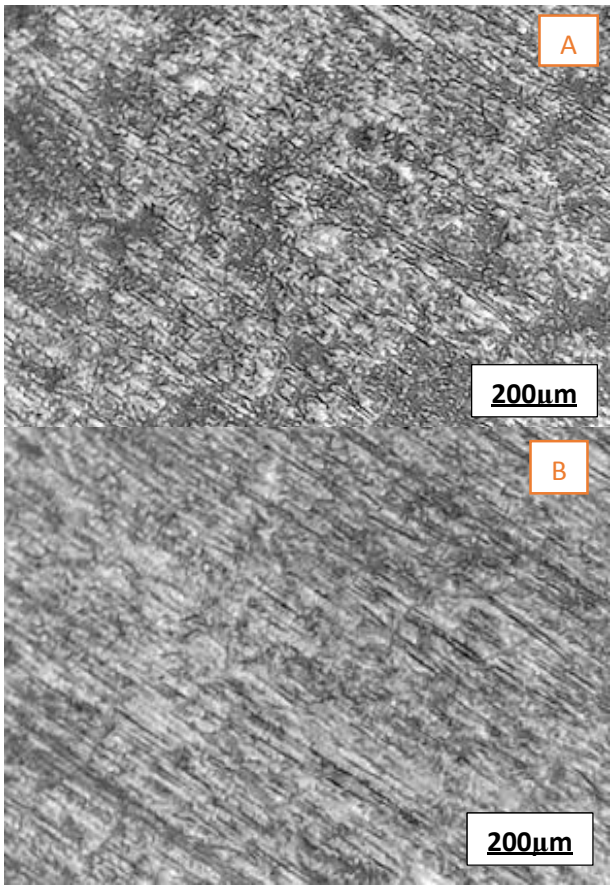


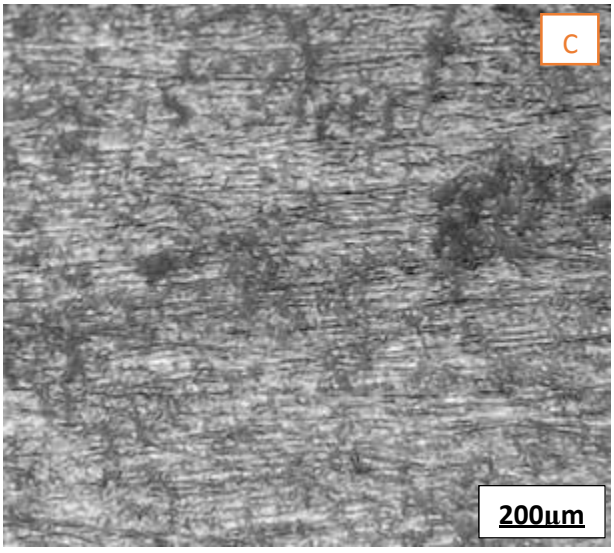


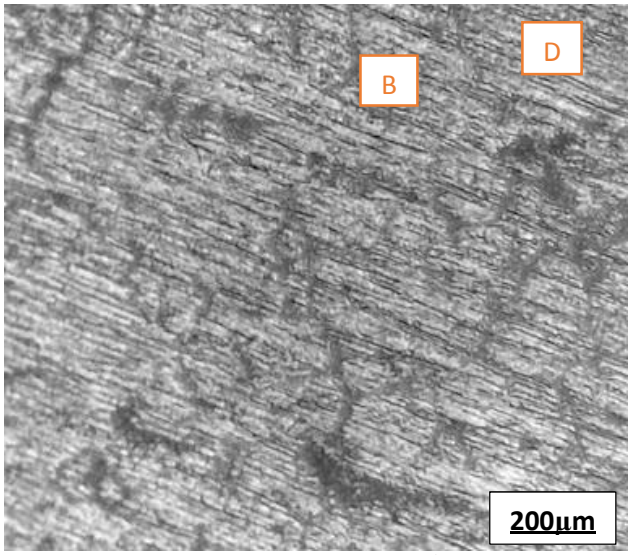


**Fig. 7** Processed and threshold colour images (blue) after eliminating noise using the image analysis (a) Unreinforced AA6063, (b) AA6063/5wt%PKS, (c) A6063/7.5wt%PKS and (d) AA6063/15wt%PKS Composites

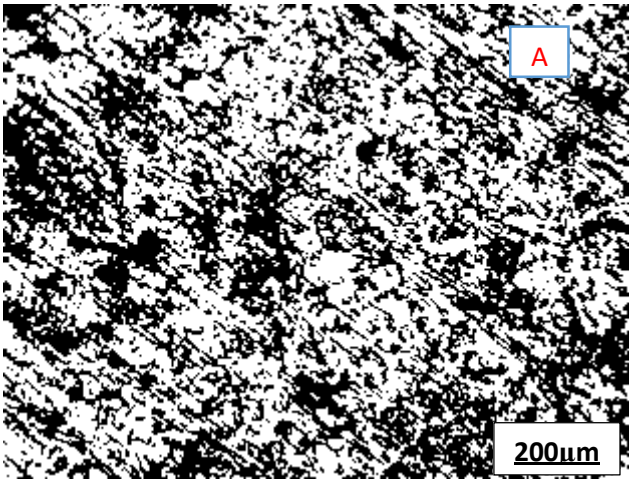


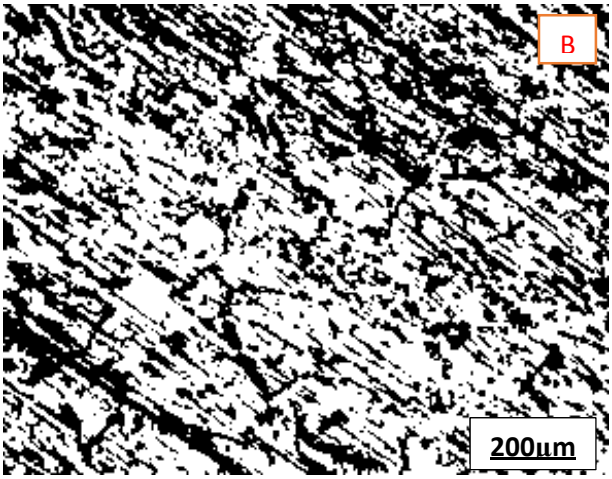

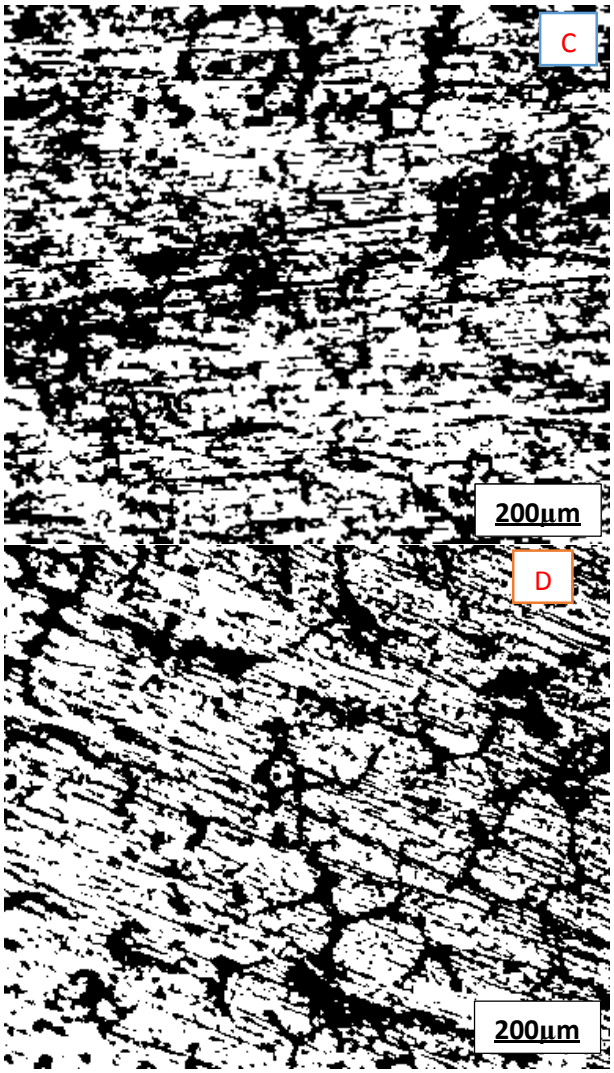


**Fig. 8** Processed and thresholded (black and white) images (a) Unreinforced AA6063, (b) AA6063/5wt%PKS, (c) A6063/7.5wt%PKS and (d) AA6063/15wt%PKS Composites

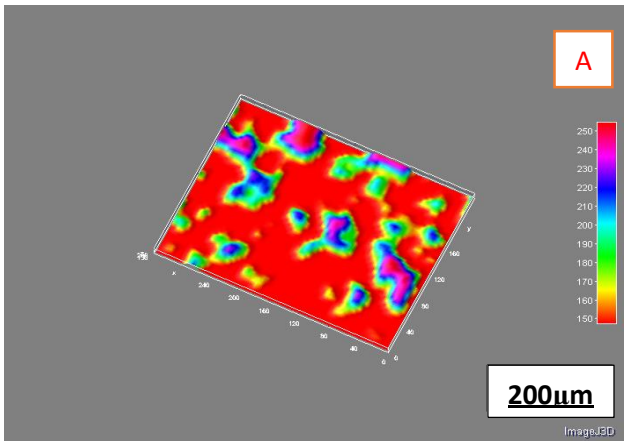


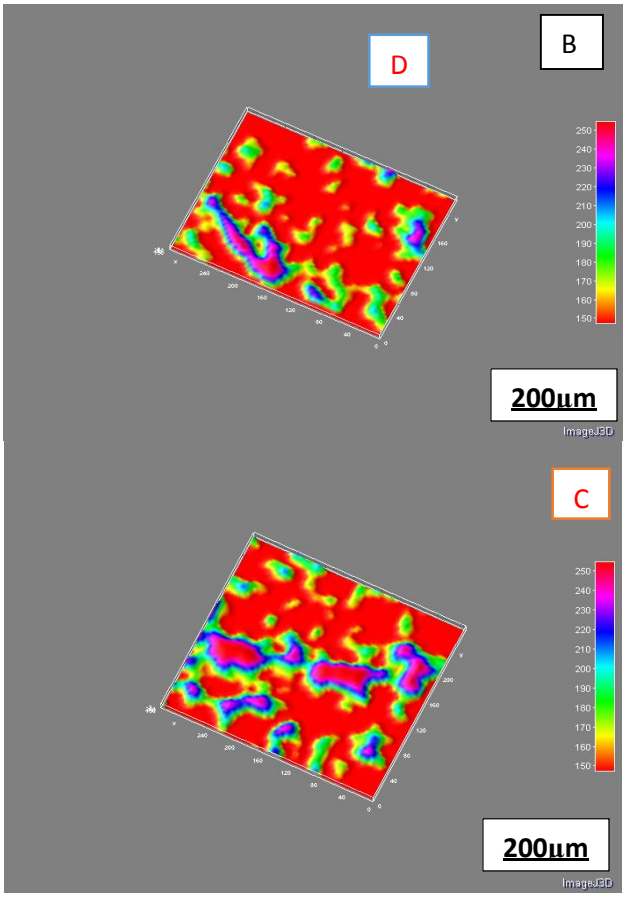


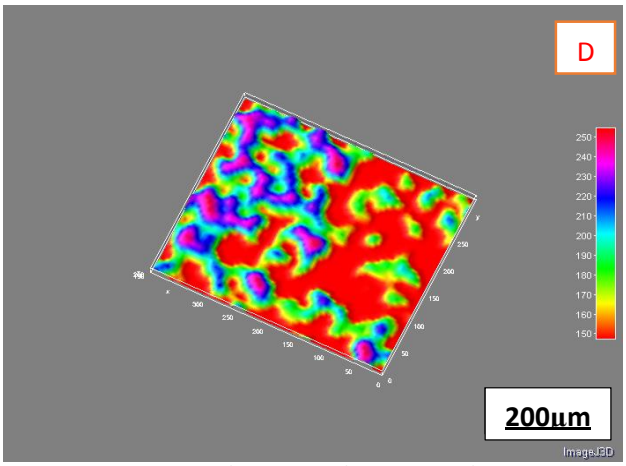


**Fig. 9** Interactive 3D surface plot of (a) Unreinforced AA6063, (b) AA6063/5wt%PKS, (c) A6063/7.5wt%PKS and (d) AA6063/15wt%PKS Composites

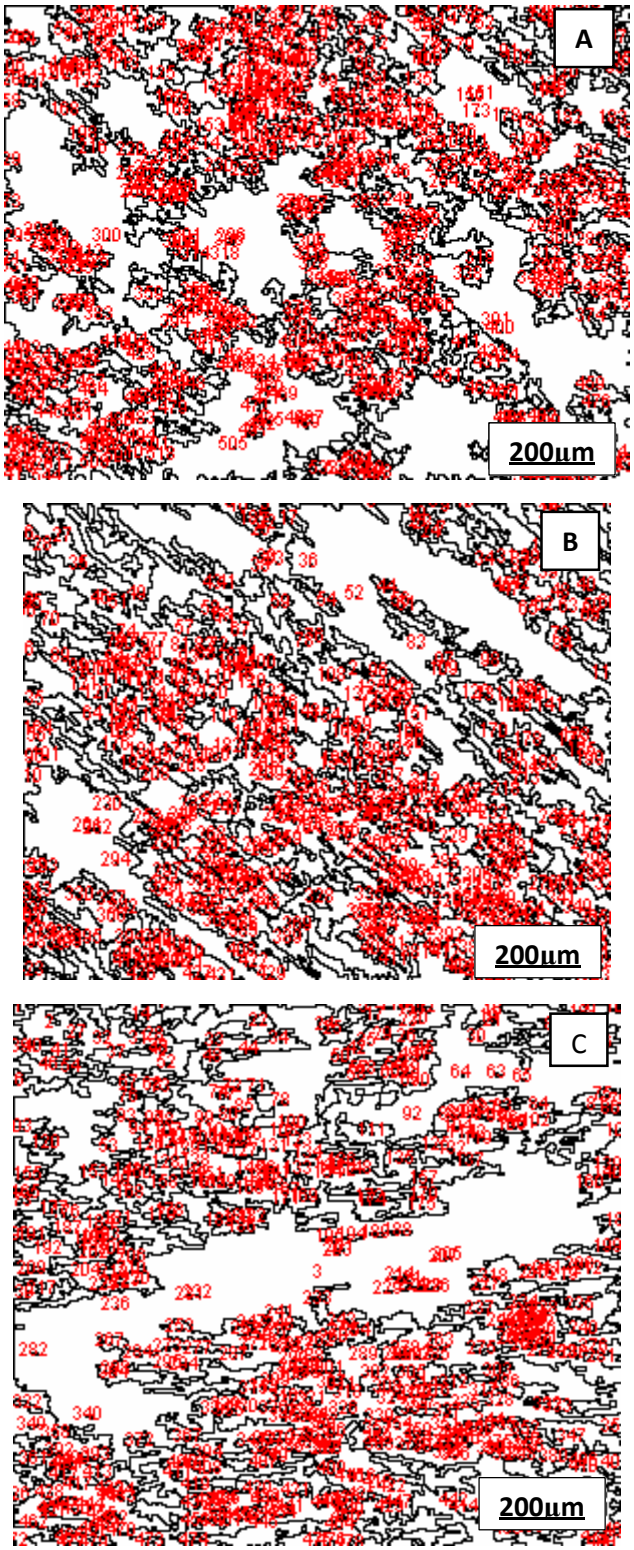


**Fig. 10** Map drawing of the particle area distribution of black and white threshold (using Analyse tool) for (a) Unreinforced AA6063, (b) AA6063/5wt%PKS, (c) A6063/7.5wt%PKS and (d) AA6063/15wt%PKS Composites

## CONCLUSION

From the foregoing observations and analysis, it would be proper to conclude that better and enhanced wear properties were obtained by the 10wt% PKS reinforcement. The least sliding distance was covered in that sample during the abrasive sliding experiment due to higher surface friction opposing the sliding motion, despite the application of constant load and uniform number of cycles of revolution. It is shown that image analysis tools are useful for the assessment of microstructural features, such as particles size and shape descriptors and properties of aluminium matrix composites. Several particles shape and size factors were employed to sufficiently describe the non-spherical particles of the reinforced composites having some degree of roughness.

## REFERENCES

1. Akaluzia, R.O., Edoziuno, F.O., Adediran, A.A., Odoni, B.U., Edibo, S., Olayanju, T.M.A.: Evaluation of the effect of reinforcement particle sizes on the impact and hardness properties of hardwood charcoal particulate-polyester resin composites. Materials Today: Proceedings, 2020. https://doi.org/10.1016/j. matpr.2020.02.980
2. Sanjay, M.R., Arpitha, G.R., Naik, L.L., Gopalakrisha, K., Yogesha, B.: Applications of Natural Fibers and Its Composites : An Overview. Natural Resources, 7, 2016, 108–114. https://doi.org/10.4236/nr.2016.73011
3. Rao, V.R., Chowdary, J.R., Balaji, A., Krishna, D.S., Bhavabhuthi, B.P.R., Sreevatsava, G., Abhiram, K.: A Review on Properties of Aluminium Based Metal Matrix Composites via Stir Casting. International Journal of Scientific & Engineering Research, 7(2), 2016, 742–749.
4. Dasgupta, R.: Aluminium Alloy-Based Metal Matrix Composites : A Potential Material for Wear Resistant Applications. ISRN Metallurgy 2012, 2012, 594573 . https://doi.org/10.5402/2012/594573
5. Babalola, P.O., Bolu, C.A., Inegbenebor, A.O., Odunfa, K.M.: Development of Aluminium Matrix Composites : A review. Online International Journal of Engineering and Technology Research, 2, 2014, 1–11.
6. Muley, A. V, Aravindan, S., Singh, I.P.: Nano and hybrid aluminum based metal matrix composites : an overview. Manufacturing Review, 2(15), 2015. https://doi.org/10.1051/mfreview/2015018
7. Dinesh, M., Ravindran, R.: Aluminium AA 7075 properties enhanced by Zirconium and Chromium nano particle. International Journal of ChemTech Research, 9(01), 2016, 296–301.

8. Bodunrin, M.O., Alaneme, K.K., Chown, L.H.: Aluminium matrix hybrid composites : a review of reinforcement philosophies ; mechanical , corrosion and tribological characteristics. Journal of Materials Research and Technology, 4(4), 2015, 434–445. https://doi.org/10.1016/j.jmrt.2015.05.003
9. Gaurav, A., Amar, P., Rajesh, K.S.: Parametric Optimization and Three-Body Abrasive Wear Behavior of Sic Filled Chopped Glass Fiber Reinforced Epoxy Composites. International Journal of Composite Materials, 3(2), 2013, 32–38. https://doi.org/10.5923/j.cmaterials.20130302.02
10. Suresha, B., Siddaramaiah, Kishore, Seetharamu, S., Kumaran, P.S.: Investigations on the influence of graphite filler on dry sliding wear and abrasive wear behaviour of carbon fabric reinforced epoxy composites. Wear, 267, 2009, 1405–1414. https://doi.org/10.1016/j.wear.2009.01.026
11. Moghadam, A.D., Omrani, E., Menezes, P.L., Rohatgi, P.K.: Mechanical and tribological properties of self-lubricating metal matrix nanocomposites reinforced by carbon nanotubes (CNTs) and graphene – A review. Composites Part B, 2015. https://doi.org/10.1016/j.compositesb.2015.03.014
12. Bidulsky, R., Grande, M.A., Dudrova, E., Kabatova, M., Bidulska, J.: Dry sliding wear behaviour of low alloyed sintered steels in relation to microstructure and fracture behaviour. Powder Metallurgy, 59(2), 2016, 121–127. https://doi.org/10.1179/1743290115Y.0000000022
13. Ashok Kumar, R.T., Mohan, N., Mahesha, C.: Sliding Wear Characteristics of Fiber Reinforced Fillers Filled Polymer Based Composites : A Review. International Journal of Materials Science, 10(2), 2015, 133–169.
14. Wang, B.C., He, H., He, X.F., Chen, H.D., Huang, B.: Wear resistance , oil resistance , morphology and vulcanization performances of ethylene-vinyl acetate / acrylonitrile butadiene rubber composites. Express Polymer Letters, 13(12), 2019, 1088–1103. https://doi.org/10.3144/expresspolymlett.2019.94
15. Wang, M.Y., Williams, J.J., Jiang, L., Carlo, F. De, Jing, T., Chawla, N.: Three Dimensional ( 3D ) Microstructural Characterization and Quantitative Analysis of Solidified Microstructures in Magnesium-Based Alloys. Metallogr. Microstruct. Anal. 1, 2012, 7–13. https://doi.org/10.1007/s13632-012-0008-x
16. Vander Voort, G.F.: *Metallography: Principles and Practice*. ASM International, Philadelphia, 1999.
17. Erisir, E., Bilir, G.O.: *Quantitative Analysis of Microstructure Constituents of Dual Phase Steels*. In: Proceedings of the 2nd International Iron and Steel Symposium (IISS'15). , Karabuk, 2015.
18. Kipanyula, M.J., Sife, A.S.: Global Trends in Application of Stereology as a Quantitative Tool in Biomed Research. Biomedical Research International. 2018, 2018, 1825697. https://doi.org/10.1155/2018/1825697
19. Alo, F.I., Ajoge, E.O., Kunle, M.O., Isadare, D.A., Oyedele, A.A., Emordi, N.: Comparision of Imagej Analysis of Structure of Two Constructional Steel. American Journal of Engeering & Applied Sciences. 1(1), 2018. https://doi.org/10.3844/ajeassp.2018
20. Rishi, N.R.: Particle Size and Shape Analysis using Imagej with Customized Tools for Segmentation of Particles. International Journal of Engeering Research & Technology. 4(11), 2015, 247–250.
21. Burikova, K., Rosenberg, G.: *Quantification of Microstructural Parameter Ferritic-Martensite Dual Phase Steel by Image Analysis*. In.: METAL 2009 - 18th International Conference on Metallurgy and Materials, Conference Proceedings2009, 185-189.
22. ASM: Practical Guide to Image Analysis. ASM International, Philadelphia, 2000.
23. Chan, C.-W., Lee, S., Smith, G.C., Donaghy, C.: Fibre Laser Nitriding of Titanium and its Alloy in Open Atmosphere for Orthopaedic Implant Applications : Investigations on Surface Quality, Microstructure and Tribological Properties. Surface Coatings Technology, 309, 2017, 628–640. https://doi.org/10.1016/j.surfcoat.2016.12.036
24. Bidulská, J., Kvačkaj, T., Kočiško, R., Bidulský, R., Grande, M.A., Donič, T., Martikan, M.: Influence of ECAP-Back Pressure on the Porosity Distribution. Acta Physica Polonica A, 117(5), 2010, 864–868. https://doi.org/10.12693/APhysPolA.117.864
25. Diogenes, A.N., Hoff, E.A., Fernandes, C.P.: Grain size measurement by image analysis : An application in the ceramic and in the metallic industries. In: Proceedings of the 18th International Congress of Mechanical Engineering. , Ouro Preto, 2005.
26. Bidulska, J., Bidulsky, R., Grande, M.A., Kvackaj, T.: Different Formation Routes of Pore Structure in Aluminum Powder Metallurgy Alloy. Materials, 12(22), 2019, 3724. https://doi.org/10.3390/ma12223724
27. Bidulsky, R., Grande, M.A., Bidulska, J., Vlado, M., Kvackaj, T.: Wear Mechanism of Chromium Pre-Alloyed Sintered Steel. High Temperature Materials and Processes, 28(3), 2009, 175–180. https://doi.org/10.1515/HTMP.2009.28.3.175
28. Oladele, I.O., Ibrahim, I.O., Adediran, A.A., Akinwekomi, A.D., Adetula, Y. V, Olayanju, T.M.A.: Modified palm kernel shell fiber / particulate cassava peel hybrid reinforced epoxy composites. Results in Materials, 5, 2020, 100053. https://doi.org/10.1016/j.rinma.2019.100053
29. Oladele, I.O., Okoro, A.M.: The effect of palm kernel shell ash on the mechanical properties of as-cast aluminium alloy matrix composites. Leonardo Journal of Science, Jan-June, 2016, 15–30.
30. Ikumapayi, O.M., Akinlabi, E., Akinlabi, S.A.: Characterization of high strength aluminium – based surface matrix composite reinforced with low-cost PKSA fabricated by friction stir processing. Materials Research Express, 6, 2019. https://doi.org/10.1088/2053-1591/ab395b
31. Edoziuno, F.O., Adediran, A.A., Odoni, B.U., Utu, O.G., Olayanju, A.: Physico-chemical and morphological evaluation of palm kernel shell particulate reinforced aluminium matrix composites. Materials Today: Proceedings, 2020. https://doi.org/10.1016/j.matpr.2020.03.641
32. Hariharasakthisudhan, P., Rajan, S.B., Sathickbasha, K.: Inspiration of reinforcements , manufacturing methods , and microstructural changes on wear behavior of metal matrix composites – a recent review. Materials Research Express, 2020. https://doi.org/10.1088/2053-1591/ab6918
33. Nicolais, L., Meo, M., Milella, E. eds: Composite Materials - A Vision for the Future. Springer-Verlag, London, 2011.
34. Friedrich, K., Zhang, Z., Schlarb, A.K.: Effects of various fillers on the sliding wear of polymer composites. Composite Science and Technology, 65, 2005, 2329–2343. https://doi.org/10.1016/j.compscitech.2005.05.028
35. Orhadahwe, T.A., Adeleke, A.A., Aweda, J.O., Ikubanni, P.P., Odusote, J.K.: Microstructural image analysis of mild carbon steel subjected to rapid cyclic heat treatment. Journal of Chemical Technology and Metallurgy, 55, 2020, 198–209.
36. Peregrina-barreto, H., Terol-villalobos, I.R., Rangel-magdaleno, J.J., Herrera-navarro, A.M., Morales-hernandez, L.A., Manriquez-Guerrero, F.: Automatic grain size determination in microstructures using image processing. Measurement, 46, 2013, 249–258. https://doi.org/10.1016/j.measurement.2012.06.012
37. Chan, C., Smith, G.C.: Fibre laser joining of highly dissimilar materials : Commercially pure Ti and PET hybrid joint for medical device applications. Materials Design, 103, 2016, 278–292. https://doi.org/10.1016/j.matdes.2016.04.086
38. Goriewa-duba, K., Duba, A., Wachowska, U., Wiwart, M.: An Evaluation of the Variation in the Morphometric Parameters of Grain of Six Triticum Species with the Use of Digital Image Analysis. Agronomy, 8, 2018, 296. https://doi.org/10.3390/agronomy8120296
39. Olson, E.: Particle Shape Factors and Their Use in Image Analysis – Part 1 : Theory. Journal of GXP Compliance, 15(3), 2011.
40. Alaneme, K.K., Oganbule, C.A., Adewale, A.: Circumferential Notch Test Based Fracture Toughness Investigation of Al-Mg-Si Alloy Composites Reinforced with Alumina and Quarry Dust. Journal of Chemical Technolology and Metallurgy, 55, 2020, 469–478.

OPEN ACCESS

# ACTA METALLURGICA SLOVACA

2020, VOL. 26, NO. 2, 63-66

RESEARCH PAPER

## MEASUREMENT OF THE ABSORPTION-BASED HYDROGEN STORAGE CAPACITY OF $Ti_{0.95}Zr_{0.05}Cr_{0.8}Mn_{0.8}V_{0.2}Ni_{0.2}$ ALLOY

*Tomáš Brestovič[1], Natália Jasminská[1], Marián Lázár[1], Ľubica Bednárová[1*], Romana Dobáková[1]*

[1]Technical University of Košice, Faculty of Mechanical Engineering, Letná 9, 042 00 Košice, Slovakia

*lubica.bednarova@tuke.sk, Tel.: +421 55 602 4104, Department of Power Engineering, Faculty of Mechanical Engineering, Technical University of Košice, Letná 9, 042 00 Košice, Slovakia

Received: 06.04.2020
Accepted: 26.05.2020

**ABSTRACT**

The article describes potential application of the BCC alloy $Ti_{0.95}Zr_{0.05}Cr_{0.8}Mn_{0.8}V_{0.2}Ni_{0.2}$ in the hydrogen absorption process. It deals with the measurements of the PCI (Pressure Concentration Isotherm) characteristics applying the volumetric method. With regard to the fact that it is an indirect measurement method, the thermodynamic description was analysed in details and subsequently used to identify the weight capacity of the stored hydrogen. The article presents a detailed description of the procedure for measuring the free volume of the measuring equipment using helium which is able to penetrate into pores and apertures with the size of only a few nanometres but does not participate in the absorption into the intermetallic structure of the alloy. The hydrogen absorption into the tested alloy was initiated by repeatedly performed activation of the alloy surface. The final section of the article presents the examination of the cyclic stability of the absorption-desorption cycle within the repeated monitoring of the maximum weight capacity of the stored hydrogen.

**Keywords:** hydrogen storage, alloy, absorption, PCI, activation

### INTRODUCTION

The complete implementation of the use of hydrogen as an energy carrier requires efficient, safe, and cheap storage thereof [1-3]. Compared to gaseous and liquid storage systems, storage of hydrogen in metal hydrides (MH) exhibits several advantages [4-8]. The most important ones include mainly high volumetric density and low operating pressure; this represents significant improvement of the safety of applications thereof in the transportation segment, in various industries, or in households [9, 10]. The development of novel MH materials requires the identification of their PCI (Pressure Concentration Isotherms) curves indicating the changes in the pressure depending on hydrogen concentration at a constant temperature [11-13]. The PCI curve shows the hydrogen absorption at the equilibrium pressure until the alloy is fully saturated, as indicated by a sharp pressure increase at the maximum concentration.

The kinetics of alloy activation and storage capacity are also affected by the chemical composition of the alloy [14-16]. The impact of elementary composition on the hydrogenation characteristics of the BCC alloys was subjected to multiple investigations. As for the $Ti_{0.95}Zr_{0.05}Cr_{0.8}Mn_{0.8}V_{0.2}Ni_{0.2}$ alloy, the addition of Zr and Ni has a significant effect on the activation process. Without these components, the activation was required, at the temperatures of 300 to 750 °C. After the addition of the above mentioned elements, there is no need for the thermal activation of the alloy, unless it was exposed to oxygen; therefore, it may be assumed that the hydride surface will not be covered with the layer of oxides. The alloy with a similar composition was also investigated by Yu et al. [17].

### DESCRIPTION OF THE SPECIMEN PREPARATION AND THE MEASURING SYSTEM ASSEMBLY

For the purpose of the PCI measurements, 6.177 g of the alloy were produced applying the arc welding method. In order to ensure higher homogeneity of the specimen, it was subjected to three cycles of melting and cooling to the ambient temperature. The resulting powder product was ground in the inert argon atmosphere and subsequently subjected to the X-ray diffraction. The results of the final chemical composition of the specimen are listed in Table 1.

**Table 1** Composition of the resulting specimen

| Element | *Desired alloy composition [wt.%]* | *Achievedalloy composition [wt.%]* |
|---|---|---|
| Ti | 28.88 | 28.57 |
| V | 6.46 | 6.77 |
| Cr | 26.41 | 25.94 |
| Mn | 27.91 | 28.09 |
| Ni | 7.45 | 7.58 |
| Zr | 2.89 | 2.78 |

The measurements of the desorption PCI curve were carried out applying the volumetric method based on the principle of the gradual release of hydrogen into a volumetric cylinder [18-20]. After releasing a small amount of hydrogen, it was necessary to stabilise the pressure in the storage system. Subsequently, the amount of the released hydrogen was monitored and calculated for normal conditions with concurrent monitoring of the pressure in the hermetically sealed equipment and the hydrogen temperature. The scheme of the measuring apparatus is shown in Fig. 1.

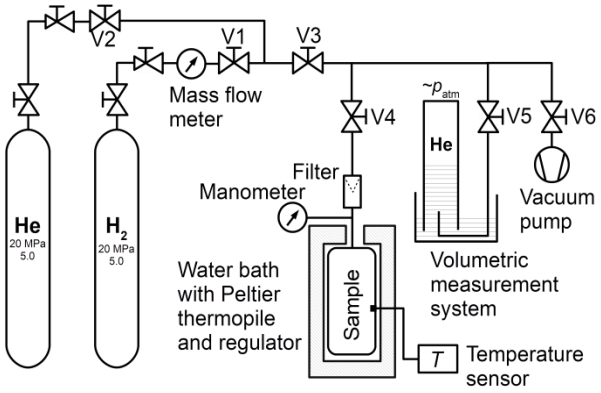


**Fig. 1** Scheme of the measurement apparatus

A substantial part of the system is a hermetically sealed chamber containing the alloy specimen; the chamber is located upstream the V4 valve. The specimen was immersed in the water bath where it was possible to measure and regulate the temperature within the range from 0 to 60 °C. The system facilitated independent supplies of helium and hydrogen at the maximum pressure of 7 MPa. Gases were removed from the system using the Edwards E2M1.5 two-stage oil vacuum pump. The pressure measurements were carried out using the BD SENSORS DX9-DMP 331i pressure sensor with the pressure range from 0 to 6 MPa. The temperature was measured using the ALMEMO FPA32P1 temperature sensor. The sensors were attached to the ALMEMO 2890-9 datalogger by the ALMEMO ZA 9020-FS connector. The assembled apparatus contained the BOSS-ML6-05 spherical valves. The measured data were indirectly used to calculate the weight capacity of the stored hydrogen; it was necessary to apply the mathematical procedure described below.

The amount of hydrogen absorbed in the alloy specimen was identified using the following formula:

$$V_{\mathrm{abs,n},i} = V_{\mathrm{tot},i} - V_{\mathrm{FV,n},i} - V_{\mathrm{VMS,n},i} \tag{1.}$$

where: $V_{\mathrm{abs,n},i}$ [m$^3$] – volume of hydrogen absorbed in the alloy at the $i^{th}$ measurement;
$V_{\mathrm{tot},i}$ [m$^3$] – total volume measured applying the volumetric method;
$V_{\mathrm{FV,n},i}$ [m$^3$] – volume of hydrogen in the free space between the alloy grains, including the supply pipeline;
$V_{\mathrm{VMS,n},i}$ [m$^3$] – volume of hydrogen measured in the volumetric measurement system.

All parameters in formula (1.) were calculated for normal conditions (101,325 Pa and 273.15 K). The volume of hydrogen in the free space of the apparatus, relative to normal conditions at the i$^{th}$ measurement, may be calculated using the following formula:

$$V_{\mathrm{FV,n},i} = \frac{T_{\mathrm{n}}}{\overline{T}} \cdot \frac{p_i}{p_{\mathrm{n}}} \cdot \frac{z_{\mathrm{n}}}{\overline{z}_i} \cdot V_{\mathrm{FV}} \tag{2.}$$

where: $T_{\mathrm{n}}$ [K] – normal temperature (273.15 K);
$\overline{T}$ [K] – average temperature in the storage volumetric system;
$p_{\mathrm{i}}$ [Pa] – absolute hydrogen pressure;
$p_{\mathrm{n}}$ [Pa] – normal pressure (101,325 Pa);
$z_{\mathrm{n}}$ [1] – compressibility factor of hydrogen in normal conditions ($z_{\mathrm{n}}$ = 1);
$\overline{z}_i$ [1] – compressibility factor at the average temperature and absolute hydrogen pressure;
$V_{\mathrm{FV}}$ [m$^3$] – free volume of the hermetically sealed system.

The free volume represents the space between the grains of the powder material, including the distribution pipeline between the pressure tank containing the specimen and the first closing valve V4. The volume of hydrogen released into the volumetric system $V_{\mathrm{VMS,n,i}}$, as calculated for normal conditions, is defined by the following formula:

$$V_{\mathrm{VMS,n},i} = V_{\mathrm{VMS},i} \cdot \frac{p_{\mathrm{VMS},i}}{p_{\mathrm{n}}} \cdot \frac{T_{\mathrm{n}}}{T_{\mathrm{VMS,i}}} \tag{3.}$$

where: $V_{\mathrm{VMS},i}$ [m$^3$] – volume of the released hydrogen in operating conditions;
$p_{\mathrm{VMS},i}$ [Pa] – absolute pressure in the volumetric system;
$T_{\mathrm{VMS},i}$ [K] – thermodynamic temperature in the volumetric system.

The total volume released into the measuring cylinder calculated for normal conditions was identical to the calculation made using formula (3.); however, it corresponded to the last (n$^{th}$) measurement.

$$V_{\mathrm{tot,n}} = V_{\mathrm{VMS,n},i}\big|_{i=n} \tag{4.}$$

The resulting mass concentration of the stored hydrogen for the i$^{th}$ measurement was identified as follows:

$$c_i = \frac{\rho_{\mathrm{H_2,n}} \cdot V_{\mathrm{abs,n},i}}{m_{\mathrm{alloy}}} \tag{5.}$$

where: $m_{\mathrm{alloy}}$ [kg] – mass of the alloy specimen;
$\rho_{\mathrm{H_2,n}}$ [kg/m$^3$] – hydrogen density in normal conditions.

During the measurements of different specimens, the free volume of the hermetically sealed system $V_{\mathrm{FV}}$ was changing due to changes in the porosity and the amount of the powder alloy. It was therefore necessary to identify this parameter prior to the measurement of the next specimen. For this purpose, the secondary gas, helium, was used prior to hydrogen absorption. The system was vacuumed, using a vacuum pump, to the absolute pressure of 5 Pa and then filled with helium with which absorption into the alloy structure does not occur; this facilitated measuring the amount of the gas released into the volumetric measurement system in order to identify the free volume between the grains and use such data to make a simple calculation of the missing parameter $V_{\mathrm{FV}}$. The calculation was based on the differential form of the equation of state; a pressure decrease in the hermetic chamber was adequate to the amount of the released hydrogen:

$$\mathrm{d}p_{\mathrm{He}} \cdot V_{\mathrm{FV}} = \mathrm{d}m_{\mathrm{He}} \cdot r_{\mathrm{He}} \cdot \overline{T} \cdot \overline{z}_{\mathrm{He}} \tag{6.}$$

where: $\mathrm{d}p_{\mathrm{He}}$ [Pa] – elementary change in the pressure in the closed chamber during the release of helium;
$\mathrm{d}m_{He}$ [kg] – elementary change in the mass of helium released from the system;
$r_{\mathrm{He}}$ [J/(kg·K)] – specific gas constant of helium;
$\overline{z}_{\mathrm{He}}$ [1] – average value of the compressibility factor.

By subsequent solving of the equation, it was possible to calculate the ratio of the free volume and the average temperature; the ratio was identical to that observed during the measurements with hydrogen and helium (while maintaining the same thermal field of the tank). Therefore, it was possible to substitute the ratio of the free volume to the average temperature directly to formula (2.) obtaining the following formula:

$$\frac{V_{\mathrm{FV}}}{\overline{T}} = \frac{\Delta m_{\mathrm{He}}}{\Delta p_{\mathrm{He}}} \cdot r_{\mathrm{He}} \cdot \overline{z}_{\mathrm{He}} \tag{7.}$$

A change in the mass of hydrogen was identified using the equation of state for hydrogen released from the volumetric measurement system:

$$\Delta m_{\mathrm{He}} = \frac{p_{\mathrm{VMS,He}} \cdot V_{\mathrm{VMS,He}}}{r_{\mathrm{He}} \cdot T_{\mathrm{VMS,He}}} \tag{8.}$$

where: $p_{\mathrm{VMS,He}}$ [Pa] – pressure in the measuring cylinder;
$V_{\mathrm{VMS,He}}$ [m$^3$] – hydrogen volume in the measuring cylinder;
$T_{\mathrm{VMS,He}}$ [K] – hydrogen temperature in the measuring cylinder.

**SPECIMEN ACTIVATION**

The specimen of the $Ti_{0.95}Zr_{0.05}Cr_{0.8}Mn_{0.8}V_{0.2}Ni_{0.2}$ alloy was activated in order to eliminate the oxidation layer which might generate during the production of and manipulation with the specimen. The specimen was exposed to three cycles of heating and cooling at the temperatures from 3 to 100 °C and at the pressures from 0 to 4.3 MPa. The specimen was first heated to 100 °C at the absolute pressure below 5 Pa and then left in these conditions for the period of 30 minutes. Subsequently, the pressure tank of the hermetically sealed system was cooled to the temperature of 3 °C and the system was filled with hydrogen to the pressure of 4.3 MPa and then left in these conditions for the period of 5 hours. During

hydrogen absorption, the pressure in the chamber slowly decreased (Fig. 2); this facilitated the calculation of the increase in the mass concentration of the stored hydrogen over time.

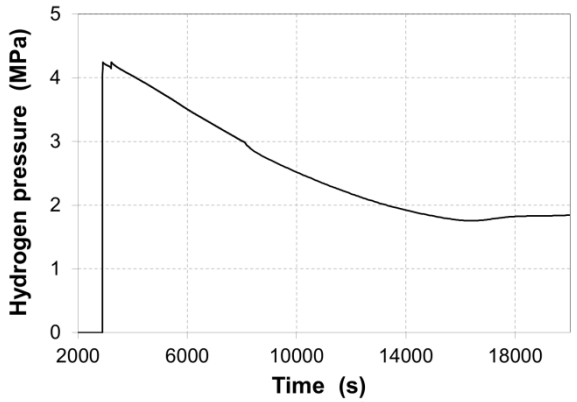


**Fig. 2** Pressure decrease in the tank during the first activation

An increase in the mass concentration may be defined as the ratio of the change in the mass concentration of the stored hydrogen per time unit in the initial linear area of the pressure decrease (between 4,000 and 8,000 s) using the following formula:

$$\psi_1 = \frac{\Delta c}{\Delta \tau} = \frac{\Delta m_{H2}}{\Delta \tau \cdot m_{alloy}} = -\frac{\Delta p_{H_2} \cdot V_{FV}}{\Delta \tau \cdot m_{alloy} \cdot r_{H_2} \cdot \bar{T}} \quad (s^{-1}) \qquad (9.)$$

where: $\Psi_1$ [$s^{-1}$] – increase in the mass concentration over time;
$\Delta c$ [1] – change in the mass concentration of the stored hydrogen;
$\Delta m_{H2}$ [kg] – change in the mass of the absorbed hydrogen;
$\Delta p_{H2}$ [Pa] – decrease in hydrogen pressure in the pressure tank;
$r_{H2}$ [J/(kg·K)] – specific gas constant of hydrogen.

During the first activation cycle, the absorption kinetics were very slow and reached the value $\Psi_1 = 4.93 \cdot 10^{-7}$ $s^{-1}$. This value represented an increase in the mass concentration in $4.93 \cdot 10^{-5}$ % per second.

The second activation cycle was carried out in identical conditions, but the kinetics of the process of the initial absorption was as much as 117 times faster ($\Psi_2 = 5.8 \cdot 10^{-5}$ $s^{-1}$). The curve of the pressure in the hermetic chamber during the second activation of the alloy is shown in Fig. 3.

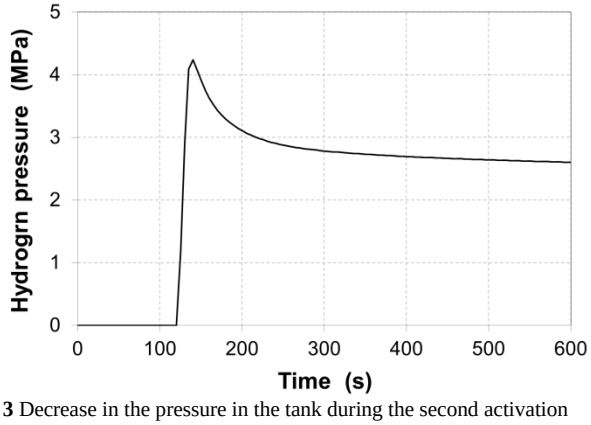


**Fig. 3** Decrease in the pressure in the tank during the second activation

During the third activation, the value of the increase in the mass concentration $\Psi_3$ was $1.66 \cdot 10^{-5}$ $s^{-1}$.

**DISCUSSION**

The measurements of the decrease in the pressure in the hermetically sealed measurement chamber during the activation indicate that the initiation of hydrogen absorption into the alloy structure requires at least three consecutive cycles of the activation process. This will initiate the process of hydrogen storage with acceptable process kinetics. Following the alloy activation and the measurement of the free volume of the hermetically sealed system, the system was vacuumed using a vacuum pump; this resulted in an increase in hydrogen pressure to 5 MPa. Through the gradual release of hydrogen into the volumetric measurement system and a subsequent calculation, as described in the mathematical apparatus, the PCI characteristics of the alloy were identified (Fig. 4).

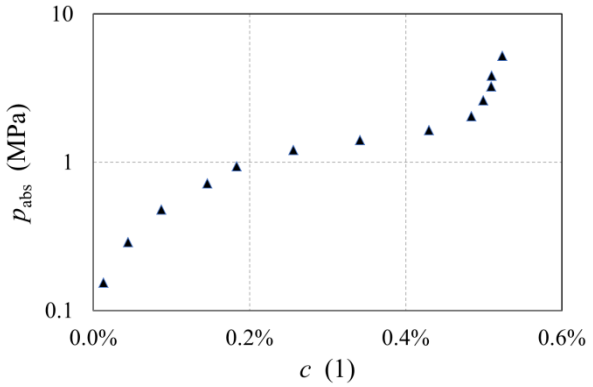


**Fig. 4** PCI characteristics of the $Ti_{0.95}Zr_{0.05}Cr_{0.8}Mn_{0.8}V_{0.2}Ni_{0.2}$ alloy during hydrogen desorption

Hydrogen absorption into the alloy begins already at the pressure of 0.2 MPa. The relevant curve indicates that the plateau pressure for the tested alloy was 1.4 MPa and after the peak mass concentration of 0.52 % was achieved, the pressure sharply increased. This was caused by the alloy saturation and further supplies of hydrogen into the storage system caused the gas accumulation in the free volume $V_{FV}$. In order to confirm the measurement accuracy and determine the cyclic stability, the measurements of the PCI characteristics were repeated 6 times while maintaining the same thermodynamic conditions. Fig. 5 shows the curve of the peak mass concentrations of the stored hydrogen at individual measurements.

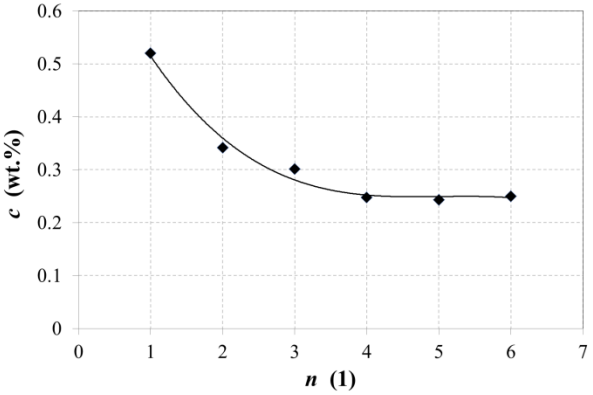


**Fig. 5** Curve of the peak weight capacity of the alloy under the periodic load

A stable value of the mass concentration, i.e., 0.25 wt. %, was reached after the third absorption-desorption cycle. From cycle 4 onwards, the alloy appeared to be stable for further hydrogen storage.

## CONCLUSION

Certain disadvantages of the pressure and cryogenic storage of hydrogen urge the necessity to search for alternative methods of storing this gas [21]. An option that seems to be appropriate is the use of metal hydride alloys which facilitate the storage of hydrogen in crystal lattices of metals. In the case of the tested alloy $Ti_{0.95}Zr_{0.05}Cr_{0.8}Mn_{0.8}V_{0.2}Ni_{0.2}$, hydrogen was stored in the cubic lattice. This alloy may be used for hydrogen storage, but the use thereof requires multiple activation of its surface. The measurements of the PCI characteristics were made applying the volumetric method which is, compared to the high-pressure thermogravimetric analysis, more cost-effective, provided that the obtained results are comparable. The problem associated with the practical application of the tested alloy in hydrogen storage is insufficient cyclic stability with a 50 % decrease in the maximum value of the mass concentration after three consequent storage processes. After the mass concentration stabilises, its value is only 0.25 wt. %, representing 27.8 litres of the stored hydrogen (in normal conditions: 101,325 Pa; 273.15 K) in 1 kg of the alloy. The measurements of the PCI characteristics clearly show that this alloy exhibits low absorption pressure of 1.4 MPa; it is therefore suitable for the direct absorption of hydrogen produced through the electrolysis of water in high-pressure electrolysers which achieve the pressures of up to 2 MPa. This eliminates the necessity of using a compressor.

**Acknowledgments:** This paper was written with the financial support of the granting agency VEGA within the project solution No. 1/0108/19 and No. 1/0626/20 and of the granting agency KEGA within the project solution No. 005TUKE-4/2019.

## REFERENCES

1. J. Andersson, S. Grönkvist: International Journal of Hydrogen Energy, 44, 2019, 11901-11919, https://doi.org/10.1016/j.ijhydene.2019.03.063
2. R. Moradi, K. M. Groth: International Journal of Hydrogen Energy, 44, 2019, 12254-12269, https://doi.org/10.1016/j.ijhydene.2019.03.041
3. E. Rivard, M. Trudeau, K. Zaghib: Materials, 12, 2019, 1-22, https://doi.org/10.3390/ma12121973
4. B. Sakintuna, F. Lamari-Darkrim, M. Hirscher: International Journal of Hydrogen Energy, 32, 2007, 1121-1140, https://doi.org/10.1016/j.ijhydene.2006.11.022
5. B. P. Tarasov, M. V. Lototskii, V. A. Yartys: Russian Journal of General Chemistry, 77, 2007, 694-711 https://doi.org/10.1134/S1070363207040329
6. M. W. Davids, M. Lototskyy, M. Malinowski, D. V. Schalkwyk, A. Parsons, S. Pasupthi, D. Swanepoel, T. V. Niekerk: International Journal of Hydrogen Energy, 44, 2019, 29263-29272, https://doi.org/10.1016/j.ijhydene.2019.01.227
7. M. Bhouri, M. Linder, I. Bürger:: International Journal of Hydrogen Energy, 43, 2018, 23357-23371, https://doi.org/10.1016/j.ijhydene.2018.10.194
8. T. Brestovič, N. Jasminská, R. Pyszko, M. Lázár, M. Puškár: Measurement, 72, 2015, 52-60, https://doi.org/10.1016/j.measurement.2015.04.027
9. T. Bibienne, R. Flacau, C.Y. Kim, J.L. Bobet, J. Huot: Materials Research, 19, 2016, 8-12, https://doi.org/10.1590/1980-5373-mr-2016-0075
10. F. Askri, M. B. Salah, A. Jemni, S. B. Nasrallah: International Journal of Hydrogen Energy, Vol 34, 2009, p. 897-905, https://doi.org/10.1016/j.ijhydene.2008.11.021
11. T. Brestovič, N. Jasminská, M. Lázár: Acta Mechanica Slovaca, 22, 2018, 24-29, https://doi.org/10.21496/ams.2018.013
12. H. Iba, E. Akiba: Intermetallics, 6, 1998, 461-470, https://doi.org/10.1016/S0966-9795(97)00088-5
13. S. Miraglia, P. de Rango, S. Rivoirard, D. Fruchart, J. Charbonnier, N. Skryabina: Journal of Alloys and Compounds, 536, 2012, 1-6, https://doi.org/10.1016/j.jallcom.2012.05.008
14. Q. Luo, J. Li, B. Li, B. Liu, H. Shao, Q. Li: Journal of Magnesium and Alloys, 7, 2019, 58-71, https://doi.org/10.1016/j.jma.2018.12.001
15. M. Ma, R. Duan, L. Ouyang, X. Zhu, Z. Chen, Ch. Peng, M. Zhu: Journal of Alloys and Compounds, 691, 2017, 929-935, https://doi.org/10.1016/j.jallcom.2016.08.307
16. A. Ovchinnikov, S. Skvortsova, A. Mamonov, E. Yermakov: Acta Metallurgica Slovaca, 23, 2017, 122-134, http://dx.doi.org/10.12776/ams.v23i2.916
17. X.B. Yu, Z. Wu, B.J. Xia, N. X. XU: Journal of Alloys and Compounds, 372, 2004, 272-277, https://doi.org/10.1016/j.jallcom.2003.09.153
18. N. Jasminská, T. Brestovič, M. Puškár, R. Grega, J. Rajzinger, J. Korba: Measurement, 56, 2014, 219-230, https://doi.org/10.1016/j.measurement.2014.07.002
19. T. Brestovič, Ľ. Bednárová, N. Jasminská, M. Lázár, R. Dobáková: Acta Tecnologia, 5, 2019, 37-41, https://doi:10.22306/atec.v5i2.52
20. S.F. Santos, J. Huot: Journal of Alloys and Compounds, 480, 2009, 5-8, https://doi.org/10.1016/j.jallcom.2008.09.191
21. A. Züttel: Materials Today, 6, 2003, 24-33, https://doi.org/10.1016/S1369-7021(03)00922-2

OPEN ACCESS

# ACTA METALLURGICA SLOVACA

2020, VOL. 26, NO. 2, 67-69

## BORON CARBIDE BASED CERAMIC COMPOSITES HOT PRESSED WITH ALUMINIUM ADDITIVE

*Pavol Švec[1]*, Zuzana Gábrišová[1], Alena Brusilová[1], Ľubomír Čaplovič[2]*

[1]Institute of Technologies and Materials, Faculty of Mechanical Engineering, Slovak University of Technology in Bratislava, Bratislava, Slovakia

[2]Institute of Materials Science, Faculty of Materials Science and Technology in Trnava, Slovak University of Technology in Bratislava, Trnava, Slovakia

*Corresponding author: pavol.svec@stuba.sk +421 2 57296 339, Institute of Technologies and Materials, Faculty of Mechanical Engineering, Slovak University of Technology in Bratislava, Námestie slobody 17, 812 31 Bratislava, Slovakia

Received: 23.03.2020
Accepted: 20.05.2020

**ABSTRACT**

Ceramic composite materials consisting of $B_4C$ matrix and $Al_8B_4C_7$ secondary phase were prepared by in situ reactive sintering of the initial powder mixture $B_4C$-Al with concentration from 5 to 25 wt.% Al sintering additives. The composite samples were hot pressed at the temperature of 1850 °C, pressure of 35 MPa, for 15 min in a vacuum atmosphere. The portion of $Al_8B_4C_7$ secondary phase increased from 3.3 to 22.1 wt.% when increasing the concentration of Al sintering additive from 5 to 25 wt.% Al. Significant improving of densification and mechanical properties was measured at increasing of Al sintering additive concentration from 5 to 10 wt.% Al. The highest average hardness of 28.74 GPa was achieved when adding 15 wt.% Al sintering additive. The fracture toughness increased with concentration of Al sintering additive in whole concentration range with the highest average value of 5.92 MPa.m$^{1/2}$ at 25 wt.% Al sintering additives.

**Keywords:** boron carbide, ceramic composite, secondary phase, hardness, fracture toughness

### INTRODUCTION

Boron carbide ($B_4C$) based ceramic materials have been intensively studied, because of their excellent properties [1-3]. Due to its prevailing covalent bonding the boron carbide based ceramic materials are extremely hard. The high hardness, above 30 GPa, places it on the third place between hardest materials after diamond and cubic boron nitride [4-6]. $B_4C$ is corrosion and wear resistant and ambient and elevated temperatures [7-8]. Boron carbide is characterized by high melting temperature of 2450 °C, it has low density of 2.52 g.cm$^{-3}$, high Young's modulus of 460 GPa and high cross-section for absorption of neutrons [4, 10-12]. Difficult sinterability of $B_4C$ is one of the main problems of reliable compacts preparations. Hinder sinterability causes closed rest porosity in the sintered compacts, which is irremovable [7, 9, 10 12]. This stems from small coefficients of self-diffusion in $B_4C$. Full density of $B_4C$ cannot be achieved at pressureless sintering without sintering additives. $B_4C$ compacts with near full density of 2.52 g.cm$^{-3}$ can be prepared by hot pressing at temperatures above 2300 °C. However, the sintering at temperatures above 2000 °C causes the particle coarsening in ceramic compacts [5, 13]. Using fine powder, adding of sintering additives and application of pressure at sintering allows decreasing of sintering temperature [12, 14-19].

One of the major disadvantages of $B_4C$ is its low fracture toughness, which have to be improved for successful applications of boron carbide based ceramics [17, 20]. An increase of fracture toughness of samples can be solved through sintering of ceramic composite systems, which enables decreasing of sintering temperature too. Choosing of suitable composite systems permits creation of new phases in situ during sintering. Sintering additives in form of some elements (such as Al, Hf, Ti, B, C), and compounds (such as $Al_2O_3$, $HfO_2$, $TiO_2$, $ZrO_2$, $Si_3N_4$, TiC, $W_2B_5$) are used at fabrication of in situ sintered $B_4C$ based ceramic composite materials [4, 14, 15]. They improve densification and influence the microstructure and mechanical properties of sintered compact because of creation of new secondary phases. Secondary phases are essential mainly for enhancing of fracture toughness, which is critical for boron carbide based ceramic materials, because it achieves values only from 2 to 3 MPa.m$^{1/2}$. The composite hardness can decrease, as phases with smaller hardness in comparison to $B_4C$ are created [15].

Sintering of $B_4C$ based ceramic composite with Al additive is interesting because of its low density [14, 20]. It is possible to densify the system at pressureless sintering, hot pressing and plasma spark sintering. Porous $B_4C$ skeleton can be infiltrated with molten aluminium. Al sintering additive is used at pressureless sintering of $B_4C$-Al system. Achieved structure is similar to boron carbide with some changes in elementary lattice cell. Compacts with the density from 95 to 99 % are possible to prepare at sintering temperatures from 2100 to 2200 °C. Hot pressing can be used for increasing of densification when the sintering temperature decreases to 1600 °C. Final composite is very dependent on the composition of powder mixture, densification value and sintering temperature. Sintering pressure has a positive effect on density and mechanical properties. Al additive enables sintering with in situ reactions and creating of composite consisting of $B_4C$ matrix reinforced with $Al_8B_4C_7$ secondary phase. $Al_8B_4C_7$ secondary phase can function as sintering additive to improve the sintering property of $B_4C$ based ceramic which could result in higher relative density, lower shrinkage rate and better mechanical properties compared to that without $Al_8B_4C_7$ secondary phase. $Al_8B_4C_7$ secondary phase can be used as high temperature construction material since it possesses density of 2.69 g.cm$^{-3}$, which is close to density of $B_4C$ (2.52 g.cm$^{-3}$) [19-21].

### USED MATERIALS AND EVALUATION METHODS

Densities, microstructures and mechanical properties of $B_4C$ based ceramic composite materials were studied on compacts prepared using hot pressing process of the initial powder mixture composed of $B_4C$ powder with different concentration of Al sintering additive. The initial $B_4C$-Al powder mixture contained 5, 10, 15, 20 and 25 wt.% Al sintering additive. Their homogenisation was accomplished using wet mixing in horizontal mill with Teflon container and $B_4C$ mill balls in isobutyl alcohol lubricant. The green samples were die pressed in simple tool with floating die of cylindrical shape with diameter of 8 mm at pressure of 140 MPa. All samples were consequently hot pressed in graphite die with floating matrix of cylindrical shape at the temperature of 1850 °C, pressing time of 15 min and pressure of 35 MPa in a vacuum atmosphere with final vacuum value about 10 Pa.

The densities of hot pressed samples were measured using Archimedes method. The microstructures were studied with Axiovert 40 MAT microscope and JEOL JSM-IT300 scanning electron microscope. The phase analysis was done using X ray diffraction method with Philips PW 1710 diffractometer. Volume portion of phases was estimates using image analysis with software of AxioVision, module Mutiphase. The hardness and fracture toughness of ceramic composite materials were measured using Vickers indenter Buehler IndentaMet 1100 with load of 49.03 N and indentation time of 10 s.

### RESULTS AND DISCUSSION

#### Densification of $B_4C$-Al initial powder mixture

The average densities of ceramic composites prepared by hot pressing of the initial powder mixture $B_4C$ with different concentration of Al are summarised in tab. 1. Their densities increased from 93.90 to 98.85 % when increasing the Al sintering additive concentration from 5 to 10 wt.% Al. Small differences in the

densities, in the interval from 98.85 to 98.89 %, were measured for samples with the initial concentration in the interval from 10 to 25 wt.% Al. These differences were lower than scatter of measured values, but the highest average density of 98.89 % was measured for sample with the initial concentration of 15 wt.% Al.

**Table 1** Effect of Al concentration on density and portion of phases in $B_4C$-$Al_8B_4C_7$ composite

| Al concentration (wt.%) | Density (%) | $B_4C$ portion (vol.%) | $Al_8B_4C_7$ portion (vol.%) |
|---|---|---|---|
| 5 | 93.90 | 96.7 | 3.3 |
| 10 | 98.85 | 94.8 | 5.2 |
| 15 | 98.89 | 92.8 | 7.2 |
| 20 | 98.74 | 86.3 | 13.7 |
| 25 | 98.84 | 77.9 | 22.1 |

**Microstructure of $B_4C$-$Al_8B_4C_7$ ceramic composite**

Microstructure of ceramic composite materials with the initial concentration of 5 and 10 wt.% Al sintering additives are depicted in Figs. 1 and 2. The microstructures contain three phases with different colours. The microstructures consist of grey matrix of boron carbide ($B_4C$) phase, light areas of aluminium boron carbide ($Al_8B_4C_7$) phase and small portion of dark areas which represent rest porosity of samples. All samples had similar microstructure but with different portion of observed phases. The portion ratio of $Al_8B_4C_7$ secondary phase increased and the portion of rest porosity decreased with increased concentration of Al sintering additive in the initial powder mixture.
The identification of phase composition was realised by X ray diffraction analysis. All composites had similar XRD records with major portion of $B_4C$ phase which corresponds with grey areas in Fig. 1 and 2 and minor portion of $Al_8B_4C_7$ phase and it corresponds with light areas in Fig. 1 and 2. The formation of $Al_8B_4C_7$ phase was in good agreement with theoretical background.

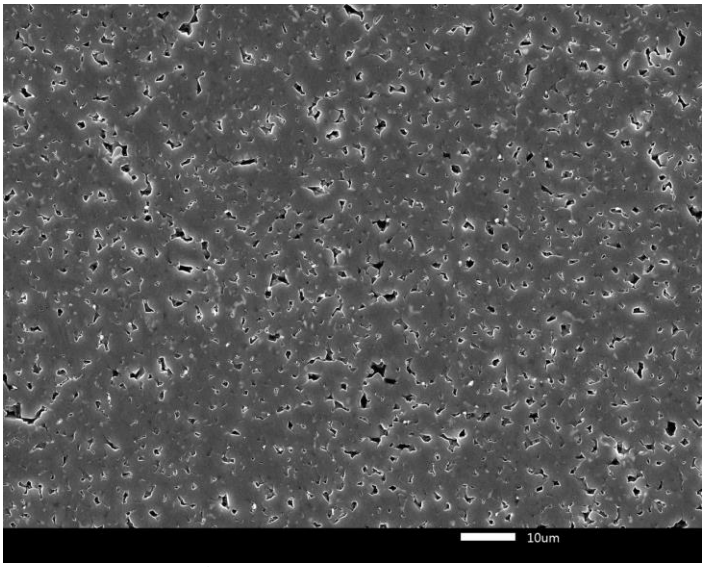


**Fig. 1** Microstructure of $B_4C$ based composite sintered with 5 wt. % Al

The effect of Al concentration on the portion of observed phases measured using the image analysis is given in Table 1. The portion of $Al_8B_4C_7$ phase was 3.3 vol.% for sample in fig. 1 which was hot pressed from the initial powder mixture $B_4C$ with 5 wt.% of Al sintering additive.
The image analysis showed a positive effect of Al sintering additive on portion of $Al_8B_4C_7$ secondary phase in $B_4C$-$Al_8B_4C_7$ composite. The image analysis of composite microstructures showed that the portion of the $Al_8B_4C_7$ secondary phase increased from 3.3 to 22.1 vol. % $Al_8B_4C_7$, but he portion of $B_4C$ matrix decreased from 96.7 to 77.9 vol.% $B_4C$ when increasing the concentration of Al sintering additives from 5 to 25 wt.% of Al sintering additive. The increase of $Al_8B_4C_7$ secondary phase portion with the increase of Al sintering additive concentration can be related to the larger extent of the in-situ reaction at higher concentration of Al.

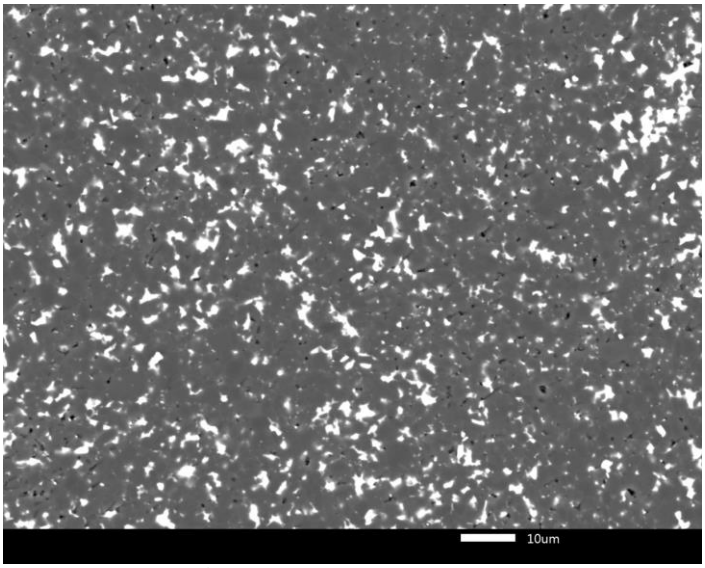


**Fig. 2** Microstructure of $B_4C$ based composite sintered with 10 wt. % Al

**Mechanical properties of $B_4C$-$Al_8B_4C_7$ composite**

The effects of Al sintering additive concentration in the $B_4C$-Al initial powder mixture on the hardness and fracture toughness of $B_4C$-$Al_8B_4C_7$ ceramic composite materials are plotted in Figs. 3 and 4.

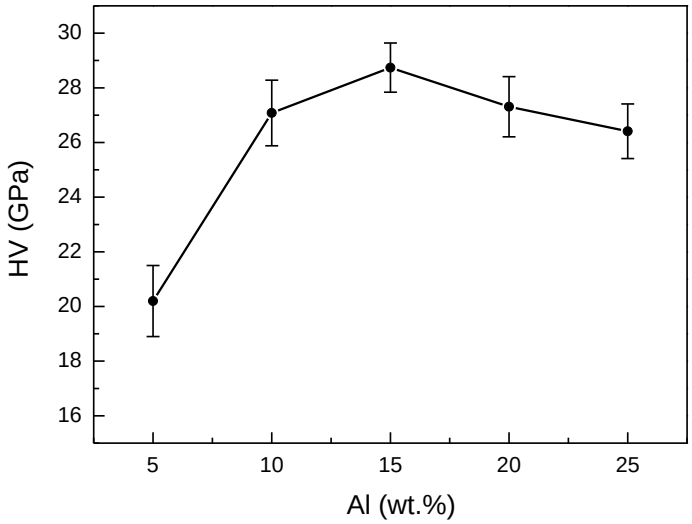


**Fig. 3** Effect of Al on hardness of $B_4C$ based ceramic composite

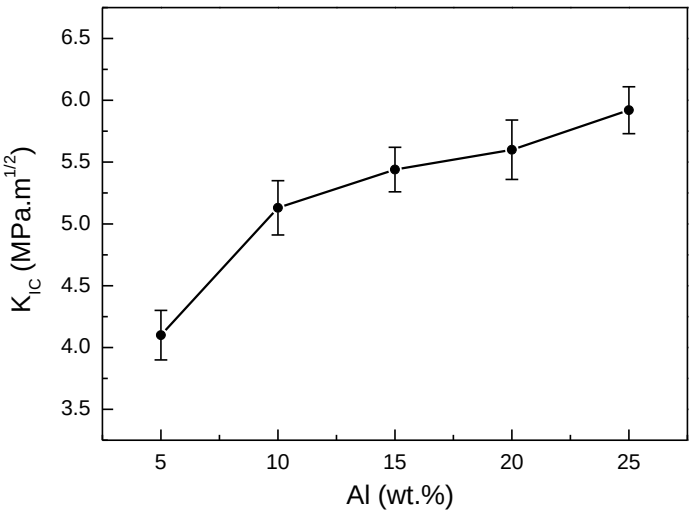


**Fig. 4** Effect of Al on fracture toughness of $B_4C$ based ceramic composite

The effect of Al sintering additive on the hardness of $B_4C$-$Al_8B_4C_7$ ceramic composite presented in fig. 3 can be divided to two sections. Average hardness of $B_4C$-$Al_8B_4C_7$ ceramic composite increased from 20.20 GPa to 28.74 GPa in the concentration interval from 5 to 15 wt. % Al sintering additive because of better densification of composite and larger extent of in situ reaction with increased concentration of Al. Average hardness of $B_4C$-$Al_8B_4C_7$ ceramic composite slightly decreased from 28.74 GPa to 26.41 GPa in the concentration interval from 15 to 25 wt. % Al because of creation of large portion of secondary phase $Al_8B_4C_7$ with lower hardness compared to $B_4C$ matrix. The highest hardness of 28.74 GPa was achieved when adding 15 wt.% Al sintering additive.

Addition of Al into $B_4C$ powder had the positive effect on the increase of fracture toughness in whole studied Al concentration range (see fig. 4). Average fracture toughness of $B_4C$-$Al_8B_4C_7$ composite increased from 4.10 to 5.92 MPa.m$^{1/2}$ with the increase of Al sintering additive concentration from 5 to 25 wt.% Al. The highest average fracture toughness of 5.92 MPa.m$^{1/2}$ was measured at composite with the highest concentration of 25 wt.% Al sintering additives. The fracture toughness increased by 44 % at the composite sintered with the highest concentration of sintering additive (25 wt.% Al) compared to the composite with the lowest concentration of sintering additive (5 wt.% Al). This effect can be explained by both toughening effect of $Al_8B_4C_7$ secondary phase and higher fracture toughness of $Al_8B_4C_7$ compared to $B_4C$ matrix.

## CONCLUSIONS

Ceramic composite material consisting of boron carbide $B_4C$ matrix and aluminium boron carbide $Al_8B_4C_7$ secondary phase was prepared by hot pressing of the initial powder mixture $B_4C$-Al with concentration from 5 to 25 wt.% Al. The composite samples were hot pressed at the temperature of 1850 °C, pressure of 35 MPa, during hot pressing time of 15 min in vacuum atmosphere about 10 Pa.

Significant improving of average density of $B_4C$ based ceramic composite material from 93.90 to 98.85 %. was reached at increasing of Al sintering additive concentration from 5 to 10 wt.% Al. The highest average density of 98.89 % was measured for composite with the initial concentration of 15 wt.% Al sintering additive.

The portion of the $Al_8B_4C_7$ secondary phase increased from 3.3 to 22.1 vol.% $Al_8B_4C_7$ when increasing the concentration of Al sintering additives in the initial $B_4C$-Al powder mixture from 5 to 25 wt.% of Al sintering additive.

The hardness of $B_4C$-$Al_8B_4C_7$ ceramic composite increased from 20.20 GPa to 28.74 GPa in the concentration interval from 5 to 15 wt. % Al sintering additive because of better densification of composite and larger extent of in situ reaction with increased concentration of Al sintering additive.

Addition of Al into $B_4C$ powder had the positive effect on the increase of fracture toughness in whole studied Al concentration range. Average fracture toughness increased from 4.10 to 5.92 MPa.m$^{1/2}$ in $B_4C$-$Al_8B_4C_7$ composite with increase of concentration of Al sintering additive from 5 to 25 wt.% Al.

**Acknowledgments:** This work was supported by the Scientific Grant Agency of the Ministry of Education, Science, Research and Sport of the Slovak Republic under the VEGA 1/0298/18 contract. The work was supported by UVP STU Bratislava the ITMS 26240220084 project.

## REFERENCES

1. Y. Gao et al.: Materials and Design, 92, 2016, 814-822. https://doi.org/10.1016/10.1016/j.matdes.2015.12.123
2. X. Zhang et al.: Ceramics International, 44(9), 2018, 10766-10772. https://doi.org/10.1016/j.ceramint.2018.03.114
3. L. Roumiguier, A. Jankowiak, N. Pradeilles, G. Antou, A. Maitre: Ceramics International, 45(8), 2019, 9912-9918. https://doi.org/10.1016/j.ceramint.2019.02.033
4. D. Wang, S. Ran, L. Shen, H. Sun, Q. Huang: Journal of the European Ceramic Society, 35(3), 2015, 1107-1112, https://doi.org/10.1016/j.jeurceramsoc.2014.10.018
5. H. Wie et al.: Ceramics International, 45(12), 2019, 14749-14755. https://doi.org/10.1016/j.ceramint.2019.04.201
6. P. Hvizdoš, A. Vencl: Ceramic Matrix Composites With Carbon Nanophases: Development, Structure, Mechanical and Tribological Properties and Electrical Conductivity, *In book: Reference Module in Materials Science and Materials Engineering*, first ed., Elsevier, Amsterdam, 2021, 1-18. https://doi.org/10.1016/B978-0-12-803581-8.11858-2
7. B.M. Moshtaghioun, F.L. Cumbrera, A.L. Ortiz, M. Castillo-Rodríguez, D. Gómez-García: Journal of the European Ceramic Society, 34(3), 2014, 841-848. https://doi.org/10.1016/j.jeurceramsoc.2013.10.006
8. R.M. White, E.C. Dickey: Journal of the European Ceramic Society, 34(9), 2014, 2043-2050. https://doi.org/10.1016/j.jeurceramsoc.2013.08.012
9. D. Wang, H. Sun, Q. Deng, Z. Ding, S. Ran, Q. Huang: Ceramics International, 40(9), 2014, 15341-15344. https://doi.org/10.1016/j.ceramint.2014.06.103
10. M.S. Heifari, H.R. Baharvandi: International Journal of Refractory Metals and Hard Materials, 51, 2015, 224-232. https://doi.org/10.1016/j.ijrmhm.2015.04.003
11. R. Lu, S. Chandrasekaran, W.L. Du Frane, R.L. Landingham, M.A. Worsley, J.D. Kuntz: Materials and Design, 148, 2018, 8-16. https://doi.org/10.1016/10.1016/j.matdes.2018.03.026
12. X. Li et al.: Ceramics International, 40(3), 2014, 4359-4366. https://doi.org/10.1016/j.ceramint.2013.08.106
13. B.M. Moshtaghioun, M.A. Laguna-Bercero, D. Gomez-García, J.I. Pena: Journal of Alloys and Compounds, 795, 2019, 408-415. https://doi.org/10.1016/j.jallcom.2019.05.037
14. H. Latifi, A. Moradkhani, H. Baharvandi, J. Martikainen: Materials and Design, 62, 2014, 392-400. https://doi.org/10.1016/10.1016/j.matdes.2014.05.039
15. S. Faila, C. Melandri, L. Zoli, G. Zucca, D. Sciti: Journal of the European Ceramic Society, 38(9), 2018, 3089-3095. https://doi.org/10.1016/j.jeurceramsoc.2018.02.041
16. X. Zhang et al.: Ceramics International, 43(8), 2017, 6345-6352, https://doi.org/10.1016/j.ceramint.2017.02.043
17. Q. Wen, Y. Tan, Z. Zhong, H. Zhang, X. Zhou: Materials Science and Engineering A, 701, 2017, 338-343. https://doi.org/10.1016/j.msea.2017.06.100
18. X. Zhang et al.: Ceramics International, 44(2), 2018, 2615-2619. https://doi.org/10.1016/j.ceramint.2017.10.230
19. J. Hu, F. Zhang, W. Wang, Z. Fu, J. Zhang: Journal of the European Ceramic Society, 39(9), 2019, 2874-2881. https://doi.org/10.1016/j.jeurceramsoc.2019.03.028
20. K. Sairam et al.: Journal of the American Ceramic Society, 101, 2018, 2516-2526. https://doi.org/10.1111/jace.15376
21. W. Ji, R.I. Todd, W. Wang, H. Wang, J. Zhang, Z. Fu: Journal of the European Ceramic Society, 36(10), 2016, 2419-2426. https://doi.org/10.1016/j.jeurceramsoc.2016.03.028

OPEN ACCESS

# ACTA METALLURGICA SLOVACA

2020, VOL. 26, NO. 2, 70-73

**RESEARCH PAPER**

## MECHANICAL PROPERTIES OF PRODUCT FROM 7075 ALUMINUM CHIPS AFTER CONSOLIDATION BY KOBO METHOD

*Beata Pawłowska*[1*]

[1]*Rzeszow University of Technology, al. Powstańców Warszawy 8, 35-959 Rzeszów, Poland*

*Corresponding author: bpaw@prz.edu.pl, Tel.: +48178651237, Department of Materials Forming and Processing, The Faculty of Mechanical Engineering and Aeronautics, Rzeszow University of Technology, al. Powstańców Warszawy 8, 35-959 Rzeszów, Poland

Received: 06.12.2019
Accepted: 03.06.2020

**ABSTRACT**

This paper presents the possibility of consolidating side products of turning of aluminum alloys into the form and properties of solids metals using low-temperature KoBo extrusion method has been assessed.The proposed method is based on cold compaction of chips into briquettes, and then extrusion by KoBo method at room temperature. The extruded rods were tested for mechanical properties (uniaxial tensile test and Vickers hardness test), and compared with specific mechanical properties of solid material. A very good effect of chips compaction has been proved by KoBo method, which has been confirmed by relatively slightly different mechanical properties of the material after consolidation compared with the solid one.

**Keywords:** metallic chips, KoBo method, extrusion, mechanical properties of extrudate

### INTRODUCTION

Manufacturing metal objects leads to a great amount of scrap material, such as: chips, cuttings or defective components. Most often, such scrap material goes back to steel plants, where it is recycled (by melting) and some part of it can be used again in manufacturing processes.
Aluminum machining chips are one of the most difficult types of scrap to recycle using traditional methods of remelting. It is characterized by elevated surface/volume ratio and it is usually oxidized and covered by different types of contaminants (i.e. lubricants used for the machining process). Due to these features, conventional consolidation by melting technologies may lead to different drawbacks and environmental issues (e.g. fumes and gas formation, energetic/economic issues). In the last years, the consolidation by melting of aluminum alloys has been deeply investigated by many researchers [e.g. 1-5]. From these studies it arises that the recovery rate of the entire process usually hardly reaches 50%. Moreover, the whole process requires several intermediate operations: cleaning, dying, compacting, etc. as well as high energy usage, causing these conventional technologies to be inadequate for the modern industrial needs.
However, there exists another method of metal waste management, which involves its direct conversion into solid material. One of the promising ways of consolidation of metallic scrap, alternative to re-melting, is the technology based on plastic working [e.g. 6-9].
There are great literature reports concerning the consolidation of metallic chips based on the traditional plastic deformation processes (e. g. high-temperature extrusion) [10-22]. However, conventional, high-temperature extrusion of chips does not result in their satisfactory consolidation due to the slight value of extrusion ratio λ and strong surface oxidation of chips. So far, using SPD (Severe Plastic Deformation) in particular ECAP methods to solve this problem, given their low efficiency, have not proved to be very applicable in the industry. That is why, new methods of chip consolidation by low-temperature processes are being investigated. Such a result can be obtained by the use of KoBo extrusion method [e. g. 23-26].
KoBo method is an interesting technical and technological solution allowing for controlling the process of plastic flow of metallic materials, but also an effective method of forming the structure and properties of materials. The application of additional reversible torsion of die by a given angle, at specific frequency (Fig. 1) results in some strain caused by die torsion leading to the existence of viscoplasticity effect of the material [27-31]. The essence of KoBo method is the change of strain path, which leads to the change of stress and results in lower extrusion force.

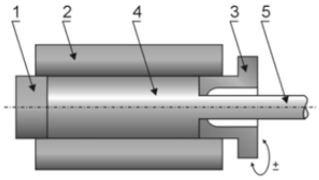


1 – punch, 2 – container, 3 – reversibly rotating die, 4 – extruded metal/billet, 5- product

**Fig. 1** Scheme of extrusion by KoBo method [36]

Superplastic type of metal flow makes it possible to obtain a high quality product, even with complex shapes. As a result, a product is obtained with high plastic properties, suitable for further, direct forming operations [23, 30, 32].
The great advantage of the process compared to classical SPD and extrusion methods is to obtain the product in a single step [30-34], at room temperature and with properly reduced cross sections, even for hardly deformable materials [e.g. 30, 32].
In case of extrusion of chips there are two issues: the necessity of their compaction up to solid state and recreation of joints between individual chips in order to form bulk material/product, which requires inducing a cyclic change of strain path in each of them. In particular, cyclic torsion leads to deformation in the sheared layers, and thus "exposure" of new, non-oxidized surface elements of adjacent chips. High compressive stresses provide them with good mutual adhesion and in effect their stable joint at atomic level [33-35].
The KoBo method is an efficient, low energetic method for consolidation of chips. Each of the five process parameters (temperature, extrusion ratio, extrusion rate, angle and frequency of oscillations) can exert influence on mechanical properties and microstructure. This influence should be considered in order to obtain desirable results.
The aim of the study is to present the possibility of consolidation machining chips from aluminum alloys into products with properties of solids leaving the liquid phase out has been assessed and the analysis of the effects of process parameters on the mechanical properties of the final product. For this purpose, the process of low-temperature extrusion using the KoBo method was used. The proposed method is based on cold compaction of chips into briquettes, and then extrusion by KoBo method without initial heating. The extruded rods were tested for mechanical properties (uniaxial tensile test and Vickers hardness test), and compared with specific mechanical properties of extrudate made of bulk material.

### MATERIAL AND METHODS

#### Experimental procedures

The investigation was conducted on 7075 alloy in the form of chips from manufacturing process and in the form of solid material, for the sake of comparison of the final effects of both methods.
The machining chips coming from the manufacturing processes, contained coolant and lubricant residue. They were not given any cleaning after being produced. In the first stage of the experiment, the chips were compacted. They were put into a special container (cylindrical container with a 60 mm diameter hole) and pressed on a vertical hydraulic press under pressure of 30T. The obtained metal briquettes were used as billets for KoBo method (Fig. 2). The process of consolidation by KoBo extrusion method at low temperature was conducted on the HYDROMET hydraulic KoBo press with the maximum load of 2,5 MN.

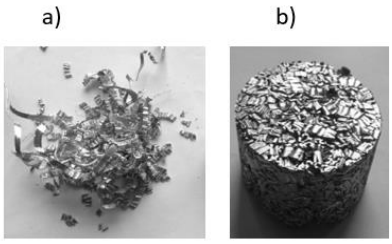


**Fig. 2** Chips of 7075 alloys (a) and briquettes (b) made of them as billet for KoBo process

Based on the experimental results obtained in the process of extrusion of solid metals and alloys, the presented experiments were conducted with the amplitude of the die rotation angle equal to ±8°. The frequency of die oscillation was selected in the range of 5÷8Hz. The extrusion process was conducted at room temperature with the use of non-heated briquettes as billets. The extrusion rate was in the range of 0,2-0,25 mm/s .The parameters of the extrusion process were the same for both extruded material (chips and bulk).
As a result of extrusion process ϕ10 mm rod was obtained with the extrusion ratio λ = 36. The obtained products (Fig. 3) were tested for their mechanical properties in a uniaxial tensile test and Vickers hardness test.

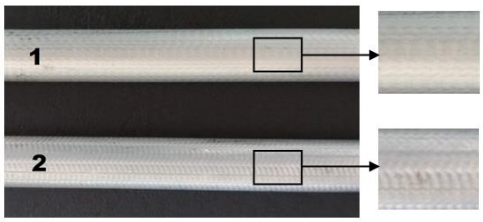


**Fig. 3** Rods obtained by KoBo method: 1 – rod made of bulk billet (smooth surface quality), 2 – rod obtained from chips (smooth surface with "pattern" resulting from die rotation)

## RESULTS AND DISCUSSION

### Investigation of mechanical properties of KoBo extruded rods

Quality evaluation of extrudates is based on the determination of their mechanical properties and surface quality. Test pieces for a static uniaxial tensile test were taken from extruded rods, and test was conducted by means of Zwick/Roell Z100 testing machine. The test pieces were taken from the beginning, middle and end part of the extrudate. They were subjected to tensile test at constant strain rate. Diagrams showing stress–strain (σ – ε) relationship were made, and tensile strength ($R_m$), yield point ($R_{0,2}$) and elongation (A) were determined.
Also, Vickers hardness tests were taken
according with PN-EN ISO 6507-2 by means of NEXUS 4303 hardness tester. Test pieces for hardness tests were made according with standards mentioned in PN-EN norms (e.g. PN-EN ISO 6507-1:20020. Fig. 4 shows the diagram of tensile tests on rods obtained by consolidation of chips of 7075 in the process of extrusion by Kobo method, whereas Table 1 presents determined mechanical properties.

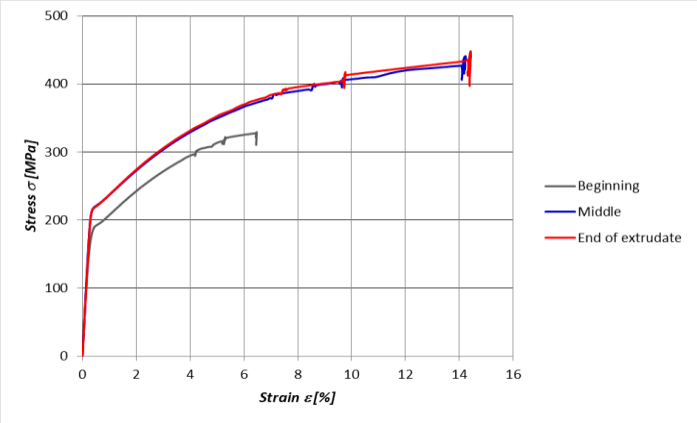


**Fig. 4** Tensile curves of ϕ10 mm rods after 7075 chips consolidation by KoBo method

**Table 1** Mechanical properties of extrudates made of chips extruded by KoBo method (average values from three test pieces)

| Test piece/Properties | $R_m$ [MPa] | $R_{0,2}$ [MPa] | A [%] |
|---|---|---|---|
| 7075 – beginning of extrudate | 309 | 190 | 6.6 |
| 7075 – middle of extrudate | 385 | 210 | 14.2 |
| 7075 – end of extrudate | 392 | 219 | 14.3 |

By comparing mechanical properties of the material from the extruded consolidated chips in a tensile test, it can be observed that the tensile strength increases as the distance from the beginning of the extrudate grows. The yield point is similar with a significant difference at the end part of the rod. Elongation at specific parts of the rod has shown a considerable growth at the end of the extrudate.
For comparison of the effect of KoBo extrusion of consolidated chips the results of extrusion of bulk material were given. Fig. 5 presents diagrams illustrating tension of rods from bulk material of 7075 alloys in the process of concurrent extrusion by KoBo method, whereas Table 2 shows determined mechanical properties.

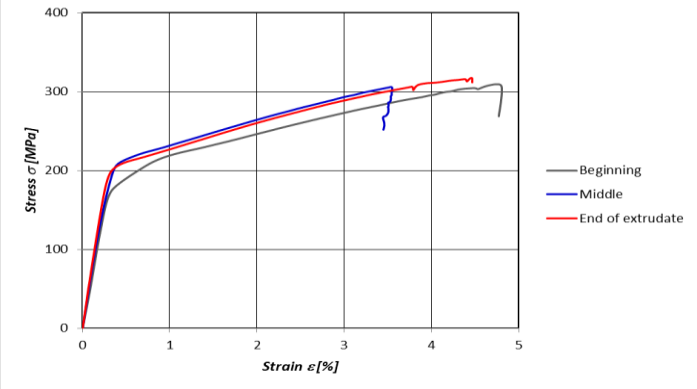


**Fig. 5** Tensile curves of ϕ10 mm rods obtained from bulk 7075 materials by KoBo method

**Table 2** Mechanical properties of extrudate made of bulk material extruded by KoBo method (average values from three test pieces)

| Test piece/Properties | $R_m$ [MPa] | $R_{0,2}$ [MPa] | A [%] |
|---|---|---|---|
| 7075 – beginning of extrudate | 295 | 189 | 4,7 |
| 7075 – middle of extrudate | 295 | 214 | 4,4 |
| 7075 – end of extrudate | 303 | 209 | 3,4 |

Analyzing the properties of rod made of bulk material of 7075 alloy it can be observed that the tensile strength increases as the distance from the beginning of the extrudate grows. The obtained product is characterized by varied yield point with the lowest point in the beginning part of the tested piece for 7075 alloy. The elongation in the beginning and middle the part of extrudate is considerably different from the yield point measured for the ending part, which proves that the ending part of the extruded rod is relatively brittle. The longer the process, the more flowing the extruded material becomes.
Figure 6 shows the results of Vickers hardness tests with the load of 1N of the sample taken from the middle part of extrudate for 7075 bulk materials and after chips consolidation.

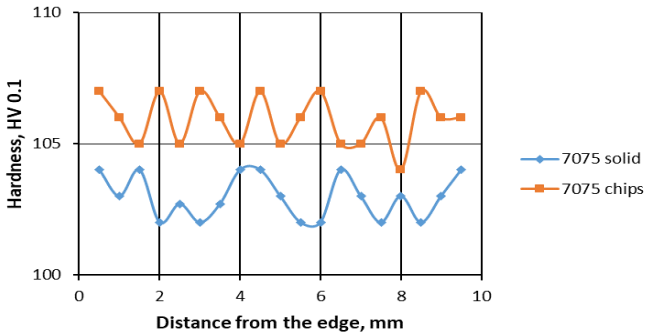


**Fig. 6** Hardness distribution in the extrudate made of chips and solid materials by KoBo method

The Vickers hardness tests prove that after chip consolidation by KoBo method the material has better hardness compared with hardness of bulk material made by KoBo method.
The oxide coating after refinement due to plastic strain in the process of extrusion constitutes the hardening phase, which has an advantageous effect on the extrudate's mechanical properties. It is proved by slightly better hardness of aluminum alloy obtained directly after chip consolidation.

**Macro- and microstructural observations**

The results of microstructural observations of profiles of the extrudate produced by bulk aluminum alloy 7075 during low-temperature KoBo extrusion is presented in fig. 7.

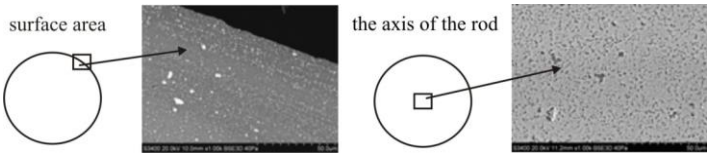


**Fig. 7** Microstructures on cross section of rod obtained from bulk 7075 alloy (cut form middle of extrudate)

Based on the observations, in the case of rods extruded from bulk material 7075 the microstructure is highly homogeneous.
In order to determine the type of phases occurring in the alloy, the chemical composition of the precipitates was analyzed in micro-areas and in points by the SEM / EDS method. The tests were carried out on polished surfaces of the digested samples. The microstructure of the 7075 alloy consists of a warp of solid alloys in aluminum and fine precipitates of irregular $MgZn_2$ phase particles and large precipitations of the $FeAl_3$ intermetallic phase, insoluble precipitates $(Fe,Mn)Al_6$ at the grain boundaries and the $Mg_2Si$ dispersion strengthening phase.
In the area of the outside diameter, plastic strain lines are visible, typical for the extrusion process, no cracks, impurities or other discontinuities were found. The plastic forming operations applied did not cause major changes in the morphology of the alloy microstructure components.
The results of microstructural observations of profiles of the compact produced by aluminum alloy 7075 chips consolidation during low-temperature KoBo extrusion are shown in Fig. 8.

Based on the observation of the microstructure of rods extruded from material from consolidated chips, it was found that in the surface areas there are heterogeneities in the form of strongly deformed, elongated bands, without a clear boundary of separation (Fig. 8).

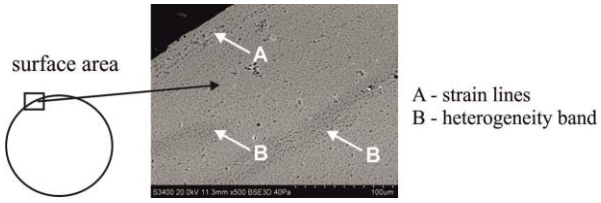


**Fig. 8** Microstructures on cross section of extruded rod obtained from 7075 alloy chips

Observations using a larger magnification allowed to state that the bands are areas constituting an integral part of the alloy, not separated by a distinct boundary and differing only in the morphology of the intermetallic phase precipitates.
In addition to the bands of heterogeneity of microstructure related to heterogeneity of alloys in the macroscopic scale, there are also areas in which discontinuities with the appearance of thin boundaries are visible. The analysis of the observation results suggests that they are oxide coating present on the surface of chips that have not degraded in the extrusion process and remained in the alloy representing the shape of the chips. These coatings are fragmentary and make the connection of chips into a fully consolidated material difficult.

**CONCLUSION**

The investigation of mechanical properties of billets extruded from consolidated chips, compared with the properties of a product extruded from bulk material by KoBo method leads to the following conclusions:

- Low temperaturing extrusion by KoBo method allows for full consolidation of dispersed chips of 7075 aluminum alloy and allows for obtaining long products by cold forming. The presence of impurities in chips, after machining, does not pose a significant difficulty for obtaining a solid product in the process of extrusion by KoBo method.
- The research has shown that the consolidation process of plastic materials based on Al alloys is able to provide very high quality and desired properties of the output product, in some cases even better than for bulk material. Obtaining material possessing good mechanical properties is conditioned by prevention of too thick oxide coatings on the chip particles' surface in the process of refinement and depletion of aluminum oxide coatings on the chip particles' surface as a result of using large plastic deformation.
- The oxide coating after refinement due to plastic strain in the process of extrusion constitutes the hardening phase, which has an advantageous effect on the extrudate's mechanical properties.
- Product made of consolidated chips is characterized by higher strength properties compared with the one obtained from bulk material, at almost twice as high elongation measured in tensile tests (Table 1, 2) and better hardness of aluminum alloy form the extruded consolidated chips (Fig. 6).

**REFERENCES**

1. Y. Chino et al.: Journal of Materials Research, 17, 2002, 2783–2786. https://doi.org/10.1557/JMR.2002.0404
2. Y. Chino, T. Hoshika, J. Lee, M. Mabuchi: Journal of Materials Research, **21** (3), 2006, 754-760. https://doi.org/10.1557/jmr.2006.0090
3. K. Kondoh, T. Luangvaranunt, T. Aizawa: Materials Transaction, 43, 2002, 322–325. https://doi.org/10.2320/matertrans.43.322
4. D. R. Cooper, J. Song, R. Gerard: Journal of Cleaner Production, 200, 2018, 282-292. https://doi.org/10.1016/j.jclepro.2018.07.246
5. Y. Wanga, H. Xua, M. Hua, S. Sugiyamab, Z. Jia: Results in Physics, 12, 2019, 718–724. https://doi.org/10.1016/j.rinp.2018.12.036
6. J. Gronostajski, A. Matuszak: Journal of Materials Processing Technology, 92-93, 1999, 35-41. https://doi.org/10.1016/S0924-0136(99)00166-1

7. S. Shamsudin, M.A. Lajis, Z.W. Zhong: Procedia CIRP, 40, 2016, 256-261. https://doi.org/10.1016/j.procir.2016.01.117
8. R. Kocisko, R. Bidulsky, L. Dragosek, M. Skrobian: Acta Metallurgica Slovaca, 20 (3) 2014, 302-308. https://doi.org/10.12776/ams.v20i3.366
9. J. Gronostajski , H. Marciniak, A. Matuszak: Journal of Materials Processing Technology, 106, 2000, 34-39. https://doi.org/10.1016/S0924-0136(00)00634-8
10. J.M. Lianga et. al.: Materials Science & Engineering, A 729, 2018, 29–36. https://doi.org/10.1016/j.msea.2018.05.047
11. J.M. Liang, M.T. Jia, X.Q. Guo, D.L. Zhang: Materials Science and Engineering, A 590, 2014, 307–313. https://doi.org/10.1016/j.msea.2013.10.050
12. R. Chiba, M. Yoshimura: Journal of Manufacturing Processes, 17, 2015, 1–8. https://doi.org/10.1016/j.jmapro.2014.10.002
13. A. Rahim SN, M. Lajis, S. Ariffin: Procedia CIRP, 26, 2015, 761. https://doi.org/10.1016/j.procir.2015.01.013
14. M. Haase, A. E. Tekkaya: Procedia Engineering, 81, 2014, 652. https://doi.org/10.1016/j.proeng.2014.10.055
15. M. Moungomo et. al.: International Journal of Advanced Manufacturing Technology, 87, 2016, 2551–2566. https://doi.org/10.1007/s00170-016-8564-x
16. S. Shamsudin, Z. Zhong, A. Rahim, M. Lajis: International Journal of Advanced Manufacturing Technology, 90, 2017, 2631–2643. https://doi.org/10.1007/s00170-016-9521-4
17. D. Baffari, G. Buffa, D. Campanella, L. Fratini: Procedia Manufacturing, 15, 2018, 280-286. https://doi.org/10.1016/j.promfg.2018.07.220
18. A.E. Tekkaya et. al.: Journal of Materials Processing Technology, 209, 2009, 3343-3350. https://doi.org/10.1016/j.jmatprotec.2008.07.047
19. M. Haase, A.E. Tekkaya: Journal of Materials Processing Technology, 217, 2015, 356-367. https://doi.org/10.1016/j.jmatprotec.2014.11.028
20. R. Chiba, T. Nakamura, M. Kuroda: Journal of Materials Processing Technology, 211, 2011, 1878-1887. https://doi.org/10.1016/j.jmatprotec.2011.06.010
21. W. Tang, A.P. Reynolds: Journal of Materials Processing Technology, 210, 2010, 2231-2237. https://doi.org/10.1016/j.jmatprotec.2010.08.010
22. V. Güley, N.B. Khalifa, A.E. Tekkaya: International Journal of Material Forming, 3, 2010, 853-856. https://doi.org/10.1007/s12289-010-0904-z
23. B. Pawłowska, R. E. Śliwa: Obróbka Plastyczna Metali, 28, 2017, 301–316.
24. A. Korbel, W. Bochniak: *Method of plastic forming of materials.* U.S. Patent No. 5,737,959, 1998, European Patent No.0711210, 2000
25. A. Korbel, W. Bochniak: Scripta Materialia, 51, 2004, 755-759. https://doi.org/10.1016/j.scriptamat.2004.06.020
26. A. Korbel et. al.: Obróbka Plastyczna Metali, 27, 2016, 133–152.
27. A. Korbel et. al.: Journal of Materials Processing Technology, 216, 2015, 160-168. https://doi.org/10.1016/j.jmatprotec.2014.09.008
28. M. Zwolak, R. E. Śliwa: Obróbka Plastyczna Metali, 28, 2017, 317–330.
29. W. Bochniak, A. Korbel: Journal of Materials Processing Technology, 134, 2003, 120-134. https://doi.org/10.1016/S0924-0136(02)01033-6
30. Paweł Koprowski et. al.: Journal of Materials Processing Technology, 253, 2018, 34–42. https://doi.org/10.1016/j.jmatprotec.2017.10.043
31. A. Korbel, W. Bochniak, P. Ostachowski, L. Błaż: Metallurgical and Materials Transactions, A 42, 2011, 2881–2897. https://doi.org/10.1007/s11661-011-0688-x
32. R. Bogucki, K. Sulikowska, M. Bieda, P. Ostachowski, K. Sztwiertnia: Archives of Metallurgy and Materials, 60, 2015, 3063–3068. https://doi.org/10.1515/amm-2015-0489
33. A. Korbel, W. Bochniak: Philosophical Magazine, 93, 2013, 1883-1913. https://doi.org/10.1080/14786435.2013.765977
34. W. Bochniak, A. Korbel, P. Ostachowski, S. Ziółkiewicz, J. Borowski: Obróbka Plastyczna Metali, 24, 2013, 83-97.
35. K. Pieła, L. Błaż, M. Jaskowski: Archives of Metallurgy and Materials, 58, 2013, 683–689. https://doi.org/10.2478/amm-2013-0055
36. W. Bochniak: *Teoretyczne i praktyczne aspekty plastycznego kształtowania metali – Metoda KoBo*, Wydawnictwo AGH, Kraków, 200

OPEN ACCESS

# ACTA METALLURGICA SLOVACA

2020, VOL. 26, NO. 2, 74-77

**TECHNICAL PAPER**

## SHAPING OF DUCTILE CAST IRON DEDICATED FOR SLAG LADLE

*Andrzej Szczęsny[1*], Dariusz Kopyciński[1], Edward Guzik[1], Grzegorz Sobół[1], Krzysztof Piotrowski[2], Paweł Bednarczyk[2], Władysław Paul[2]*

[1]*AGH-University of Science and Technology, Faculty of Foundry Engineering, Reymonta 23, 30-059 Kraków, Poland*

[2]*Krakodlew S.A., Ujastek 1, 30-969 Kraków, Poland*

**Corresponding author: ascn@agh.edu.pl; tel.: +48 12 617 27 80, AGH-University of Science and Technology, Faculty of Foundry Engineering, Reymonta 23, 30-059 Kraków, Poland*

Received: 14.08.2019
Accepted: 03.02.2020

**ABSTRACT**

In industrial conditions, ductile iron was prepared and two molds were made, in which a 600mm thick plate was formed. Filling system for one mold was placed vertically and for the second -horizontally. In order to obtain cooling curves, "S" type thermocouples have been placed in the mold. After cooling the casts, the samples from the fixing points of thermocouples were cut by the trepanning method. In the "vertical" cast sample shrinkage porosity was observed, while in the "horizontal" cast sample no porosity was detected. A significant difference in the recorded temperature in the center of the casts was discovered, indicating a defect in "vertical" cast.

**Keywords:** slag ladle, cast iron, porosity, casting; thermal analysis

### INTRODUCTION

Slag ladle or slag pot (Fig. 1) belong to the group of massive and thick-walled casts. Their shaping microstructure (during crystallization) is significantly different from the castings with smaller dimensions, which in turn consequently can lead to elements segregation and shrinkage porosity [1-7].

**Fig. 1** Examples of slag ladles produced in Krakodlew S.A.

Crystallization of heavy-section casting affects the final quality of cast iron castings, because off its wall thickness and longer cooling time. Due to the fact that these castings are exposed to thermal loads during usage and must be characterized by adequate strength, it is important to properly carry out the casting process. It can be made of various grades of cast iron, but to make extend service life, it should be made of GJS cast irons, which, unlike the GJL grade, contain nodular graphite (Fig. 2) instead flake graphite (Fig. 3). Changing the shape of graphite particles (from flake to nodule) give an increased chance of shrinkage porosity. The method of preventing this defect is the appropriate metallurgical quality of the metal [8], but also the appropriate mould technology. Increasing demand for this type of castings requires more extensive research in this area.

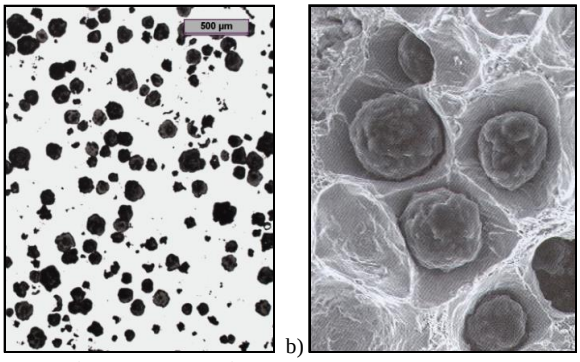


a) b)

**Fig. 2** Example of microstructure of ductile cast iron, light microscope – a), SEM – b)

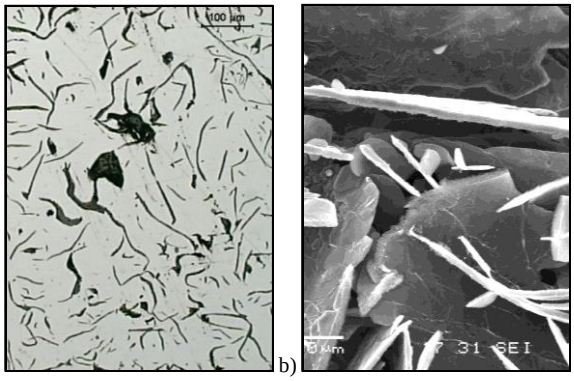


a) b)

**Fig. 3** Example of microstructure of lamellar cast iron, light microscope – a), SEM – b)

## MATERIAL AND METHODS

In order to check the metallurgical quality of metal in relation to mold technology, in industrial conditions of Krakodlew S.A. foundry, it was made two casting molds made of furan resin sand. In each form a plate (600x600x75mm) was formed. The first – vertically and the second – horizontally. The plates were used as a model tests for optimizing the production process of slag ladles. In the mold cavity, "S" type thermocouples have been placed for the measurement of cooling and crystallization curves. The article presents the results to measurements of two thermocouple. One was placed in center of the the plate and second – 75 mm from its edges (Figs. 4, 5). The thermocouples were covered by quartz casings. Additionally, a metallurgical quality test was performed using a standard „K" type cup. Then the ductile iron (from the same melt and the same ladle), which nodularization and inoculation process was carried out using cored wire method, was poured into the molds. After cooling the casting, from the thermocouples fixing points, the samples for metallographic examinations were cut out by the trepanning method.

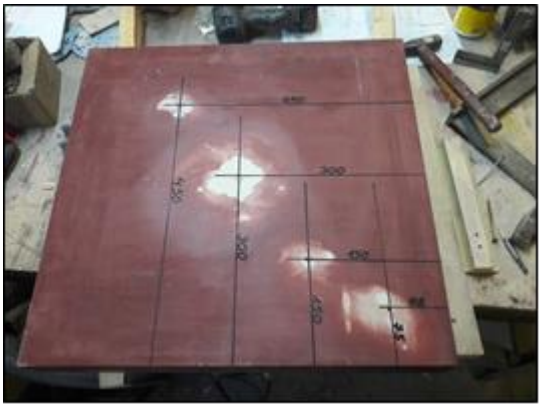

**Fig. 4** Scheme of the thermocouple arrangement in the plate

**Fig. 5** View of the mold cavity after installing the thermocouples

## RESULTS AND DISCUSSION

The symbols of the obtained samples are shown in Tab. 1. The number of graphite eutectic grains in the tested samples is presented in Fig 6. The results of the thermal analysis of the casting are presented in Fig 7. The photos of the trepanation samples are shown in Fig. 8 and 9. Obtained microstructures are shown in Fig. 10.

**Table 1 S**ymbols of the obtained samples

| Samples | Location of the thermocouple / sample | Forming a casting |
|---|---|---|
| VE | 75 mm from its edges | vertically |
| VC | in center | |
| HE | 75 mm from its edges | horizontally |
| HC | in center | |

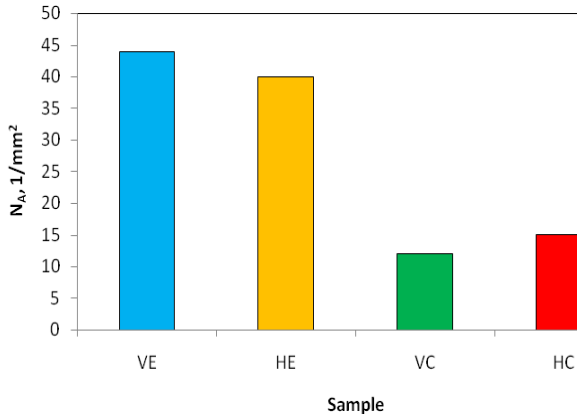


**Fig. 6** The number of graphite eutectic grains in the tested samples of nodular iron casting

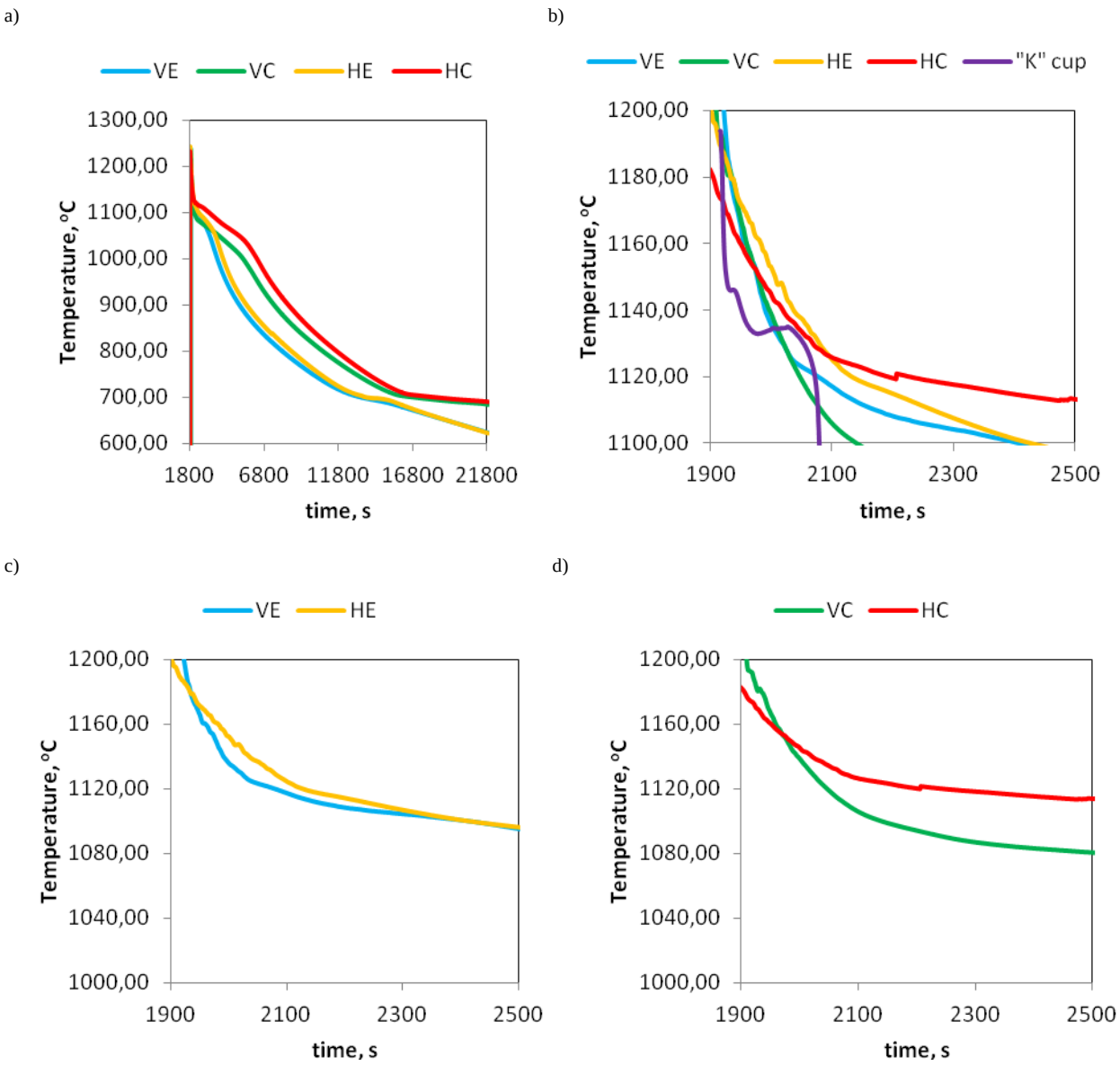


**Fig. 7** Received cooling curves: collective – a), collective with "K" cup – b),, HE and VE – c), HC and HV – d)

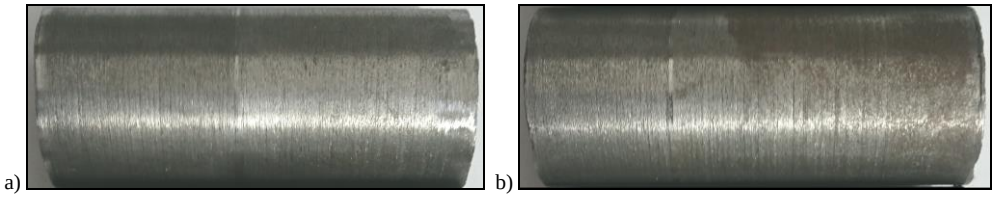


**Fig. 8** Trepanning samples cut from the plate: HC – a), HE – b)

c)


d)
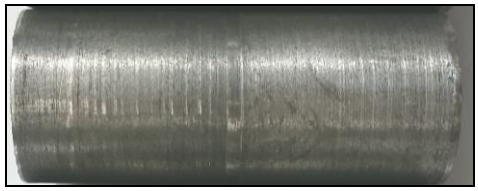

**Fig. 9** Trepanning samples cut from the plate: VC (visible porosity) – c), VE – d)

a)
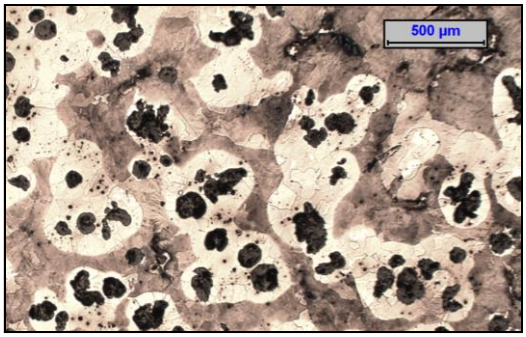


b)
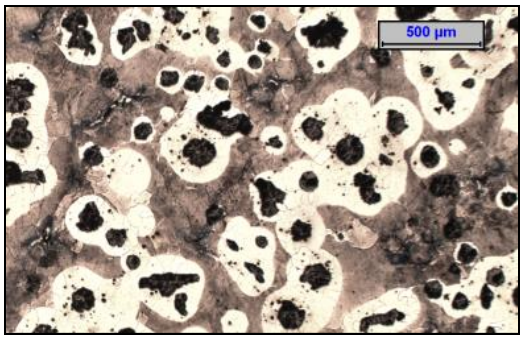


**Fig.10** Microstructure of sample HC –a), VC – b)

**Discussion**

Tests have shown that castings of the same shape but differing in the way of forming and the location of the running system can show differences in the obtained quality. The experiment showed that the vertical plate has shrinkage porosity in the center of the casting, while horizontal plate was devoid of these defects. The analysis of cooling curves showed that the temperatures near of edge of the casting was similar in both cases. In the case of thermocouples installed centrally, it can be observed that the vertically plate has a solidus temperature significantly lower than horizontally plate. Clearly, this indicates a smaller amount of crystallizing metal within a thermocouple research area.

**CONCLUSION**

1. In the vertical sample (VC) shrinkage porosity was observed, while in the horizontal sample (HC) no porosity was detected.
2. A significant difference in the recorded temperature in the center of the casts was discovered, indicating a defect in vertical plate.
3. The solidus temperature recorded in the VC was 50° C lower than in HC.

**Acknowledgments:** Authors are grateful for the support of experimental works by Smart Growth Operational Programme - " Development of an innovative technology for the production of massive slag ladles with increased exploitation parameters (tasks 9 and 10, cast steel and cast iron) POIR 01.01.01-00-0633/16.

**REFERENCES**

1. H. Rojacz H., A. I. Neacşu, L. Widder, M. Varga, J. Heiss: Wear, 350-351, 2016, 35-45. https://doi.org/10.1016/j.wear.2015.12.009
2. A. I. Neacsu., B. Scheichl, H. Rojacz, G. Vorlaufer, M. Varga., H. Schmid, J. Heiss: Steel Research International, 87, 2016, 720-732. https://doi.org/10.1002/srin.201500203
3. T. Borsato, P. Ferro, F. Berto, C. Carollo: Advanced Engineering Materials, 18, 2016, 2070-2075. https://doi.org/10.1002/adem.201600256
4. C. Weiping, Z. Liwei, L. Wenhui, L. Zhe: Advanced Materials Research, 750-752, 2013, 454-461. https://doi.org/10.4028/www.scientific.net/AMR.750-752.454
5. D. Xiaogang, N. Zhiliang, C. Fuyang, R. Shanzhi, S. Jianfei: Advanced Materials Research, 189-193, 2011, 3993-3998. https://doi.org/10.4028/www.scientific.net/AMR.189-193.3993
6. T. Borsato, P. Ferro, F. Berto, C. Carollo: Engineering Failure Analysis, 79, 2017, 902-912. https://doi.org/10.1016/j.engfailanal.2017.06.007
7. Y. Miyamoto. H. Itofuji:, Materials Transaction, 59, 2018, 1578-1584. https://doi.org/10.2320/matertrans.F-M2018833
8. D. Kopyciński, E. Guzik, A. Szczęsny, J. Dorula: Materials Science Forum, 790–791, 2013, 59–64. https://doi.org/10.4028/www.scientific.net/MSF.790-791.59